

DISS. ETH No. 29069

COHERENCE CONTROL  
WITH COMPLEX MEDIA  
FOR OPTICAL COMMUNICATIONS

A thesis submitted to attain the degree of

DOCTOR OF SCIENCES

(Dr. sc. ETH Zurich)

presented by

ALFONSO NARDI

Master in Electronics Engineering, Politecnico di Milano

born on 04.12.1993

accepted on the recommendation of

Prof. Dr. Lukas Novotny, examiner

Prof. Dr. Rachel Grange, co-examiner

Prof. Dr. David Phillips, co-examiner

2023

This work was carried out at the  
*Photonics Laboratory,*  
*Department of Information Technology and Electrical Engineering,*  
*ETH Zurich*

*che stai? breve è la vita, e lunga è l'arte;  
a chi altamente oprar non è concesso  
fama tentino almen libere carte.*  
– Ugo Foscolo, *A se stesso*

---

## Abstract

Contemporary society is in constant demand for faster and more reliable communications. This leads to an exponential increase in the load upon the communications infrastructure, which starts to suffer from physical limitations imposed by the supporting medium. Optical fibers, which have so far been able to sustain the growing demand, are in fact reaching their theoretical maximum capacity. These new challenges require innovative solutions and different approaches.

In this dissertation, we propose the use of coherence as information carrier. The standard encoding scheme achieved by modulating amplitude and phase of the single electric field is replaced by the encoding of information in the mutual coherence of each pair of a set of fields, thus generating a number of signals that scales quadratically with the number of transmitted beams. We provide a description of the resulting communication system, followed by the analysis of the dependence of the figures of merit (signal-to-noise ratio, maximum bit-rate, and spectral efficiency) on the number of transmitted fields. In addition to a potential advantage in terms of transmission capacity, we discuss how a coherence-based communication system can find application in cryptography.

The system relies on the ability to independently control the coherence between each pair of fields. To this end, we demonstrate experimentally that this control can be achieved by implementing a linear port combining several mutually incoherent fields. The experimental setup is based on a system consisting of a spatial light modulator and an optical complex medium.

In conclusion, the present work offers for the first time a method, and its experimental realization, to simultaneously control the coherence between several pairs of fields. It also demonstrates how such control can be effectively exploited to provide a new solution to the challenges present in optical communication.



---

## Abstract

Nella società contemporanea la richiesta continua di comunicazioni più rapide e ricche di informazioni comporta un aumento esponenziale del carico sulle infrastrutture di comunicazione, le quali cominciano ad intravedere limiti fisici legati ai supporti utilizzati; le fibre ottiche, che finora hanno sostenuto questa crescente domanda, stanno raggiungendo la capacità massima loro teoricamente consentita. Queste nuove sfide necessitano di soluzioni innovative e punti di vista differenti.

Nella seguente dissertazione si prospetta l'utilizzo della coerenza come veicolo di informazione: l'uso dell'ampiezza e della fase del singolo campo elettrico viene sostituito dalla codificazione dell'informazione nella coerenza della coppia di campi, generando così un numero di segnali che scala con il quadrato del numero di campi trasmessi. Per prima cosa si offre una descrizione del sistema di comunicazione e un'analisi della dipendenza dal numero di campi trasmessi delle figure di merito (rapporto segnale/rumore, bit rate massimo e efficienza spettrale). Da questa nasce una discussione circa la possibilità da parte di un sistema di comunicazione, basato sulla coerenza, di offrire un potenziale vantaggio in termini di capacità di trasmissione, e di trovare applicazione nella crittografia dei dati.

Il sistema di comunicazione proposto si fonda sulla capacità di controllare in maniera indipendente la coerenza tra ogni coppia di campi. Si dimostra che il suddetto controllo può essere ottenuto mediante l'implementazione di una porta lineare che combini diversi campi tra loro incoerenti. L'apparato sperimentale realizzato è centrato su di un sistema costituito da un modulatore spaziale di luce e un mezzo ottico complesso.

In conclusione, il presente lavoro propone un metodo innovativo e la prova empirica del controllo simultaneo della coerenza tra diverse coppie di campi, e dimostra come il controllo presentato possa essere efficacemente sfruttato per fornire una nuova soluzione alle sfide presenti nella comunicazione ottica.



---

## Foreword

The work in this dissertation would not have been possible without the contributions of several people. Shawn Divitt and Lukas Novotny designed the method for controlling the coherence matrix through a linear transformation, and proposed to use the mutual coherence as information carrier for optical communications. Moreover, Lukas Novotny first proposed to implement the coherence control employing a spatial light modulator and a multi-scattering medium. Miguel Alonso and Rodrigo Gutiérrez-Cuevas provided the theory for the generation of a three-dimensional quartic intensity (App. A). Moritz Cavigelli helped in the fabrication and characterization of the sample with gold nanoparticles used for the reconstruction of the focal intensity in App. A. Felix Tebbenjohanns, Massimiliano Rossi, Martin Frimmer and Lukas Novotny supervised the work and provided fruitful discussions throughout the whole research process. Massimiliano Rossi played an essential role in the organization of my work and in providing overall support in the various aspects of academic life. Martin Frimmer and Massimiliano Rossi taught me everything I know about scientific writing. Andreas Norrman guided me into the field of optical coherence. Andrei Militaru, together with Felix Tebbenjohanns, revised the theory presented in Ch. 3, and provided valuable feedback over all the theoretical work. Sylvain Gigan introduced me to the field of complex media and contributed to the article on which Ch. 4 is based. I acknowledge the entire Photonics Laboratory for providing the positive and engaging environment that led to this thesis. Finally, Andrei Militaru, Nicola Carlon Zambon, Eleonora Di Giuseppe, Louisiane Devaud, Fons van der Laan, Martin Frimmer and Massimiliano Rossi proofread parts of the thesis and their comments helped improving the text.

This research was funded by ETH under Grant ETH-41 19-1: *Spatial Correlation Coding*.





---

# Contents

<b>Abstract</b>	<b>i</b>
<b>Foreword</b>	<b>v</b>
<b>1 Introduction</b>	<b>1</b>
<b>2 Coherence control: theoretical background</b>	<b>7</b>
2.1 Basic definitions	7
2.2 Coherence matrix control with linear transformation	16
<b>3 Encoding information in the mutual coherence</b>	<b>19</b>
3.1 Optical communications	20
3.2 Figures of merit	27
3.3 Mutual coherence coding	30
<b>4 Coherence control with an optical complex medium</b>	<b>39</b>
4.1 Wavefront shaping in multi-scattering media	41
4.2 Coherence control: experimental realization	51
4.3 Conclusion	63
<b>5 Conclusions &amp; Outlook</b>	<b>65</b>
<b>A Related project: towards a three-dimensional quartic intensity</b>	<b>75</b>
<b>B Supplementary information</b>	<b>91</b>
<b>References</b>	<b>103</b>
<b>List of Publication</b>	<b>113</b>

Contents

---

**Curriculum vitae**

**115**

# 1

---

## Introduction

Our contemporary society is undoubtedly centered around fast and reliable exchange of information. The support of advanced communication systems is nowadays necessary in any social and economic environment, from the operation of industry and finance, to the global flow of news and knowledge, to personal entertainment. Looking into the near future, numerous emerging technologies, such as autonomous vehicles or the so-called “internet of things”, will place even greater overhead demands on current communication infrastructure (see predicted data trend in Fig. 1.1). As a prime technological example, virtual reality promises the establishment of an alternative platform that will allow people to meet and network, without the need of energy consuming transportation, thereby contributing to a more sustainable environment. This, however, entails the need for very high quality, real-time, three-dimensional virtual environments available simultaneously to countless users, thus calling for unprecedented network capacity. The ever-growing demand has been so far sustained by optical fibers, which provide the backbone of our communications infrastructure. The age of fiber optics started in 1966 with the work conducted by Charles Kao and George Hockham on ultra-low loss silica glass [2] and with the first demonstration of  $< 20$  dB/km optical fiber loss in 1970 [3]. Since then, the capacity of a single fiber has been boosted by several orders of magnitude, from a few Gb/s [4] to hundreds of Tb/s today [5]. This result has been achieved making full use of four degrees of freedom (time, polarization, frequency, and coding scheme), deploying complex quadrature

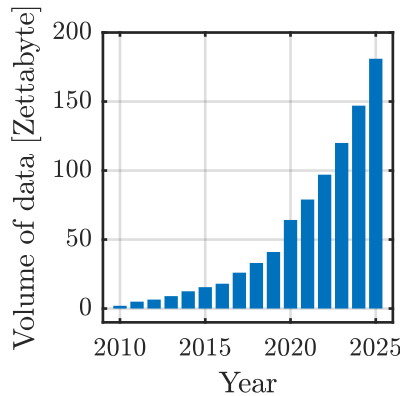


**Figure 1.1:** Volume of data/information created, captured, copied, and consumed worldwide from 2010 to 2020, with forecasts from 2021 to 2025 (in Zettabytes). The data is taken from Ref. [1].

modulation formats, polarization multiplexing, coherent detection, optical superchannels and multi-band optical transport [6–8]. However, even when efficiently exploiting the full low-loss spectral window available, a single optical fiber could not have a capacity higher than approximately 100 Tbit/s, due to the so-called “non-linear Shannon limit” [9]. Even if remarkable, this bit-rate would not be enough to satisfy the extrapolated need for 1 Pbit/s system capacity expected for the present decade [10]. The forthcoming inability to meet the growing bit-rate demand is known as “capacity crunch” [11]. The only viable solution seems to be to resort to new types of fibers that can support multiple transmission paths, thus taking advantage of the spatial degree of freedom. This approach is known as space-division multiplexing (SDM) [5]. We sketch some of the possible implementation of SDM in Fig. 1.2. The most straightforward option is to use a single-core thin fiber array, i.e., a *fiber bundle* (see Fig. 1.2a), with the disadvantage of not being cost-effective. Another solution involves embedding multiple uncoupled cores in the same glass filament (*multi-core fiber*, Fig. 1.2b). Employing this technology, it is currently possible to achieve up to 32 independent single-mode beams in a single fiber [12]. Finally, a third approach is to multiplex the information into different propagating transverse modes in the same core. For this purpose, one uses a *few-mode fiber* [13], i.e., a fiber that supports an appropriately small number of modes (see Fig. 1.2c). All of these solutions, alone or in combination, are now intensively researched for use in practical scenarios [12]. Efficiently employing another degree of freedom (space) promises a further increase of the system capacity, posing SDM as a

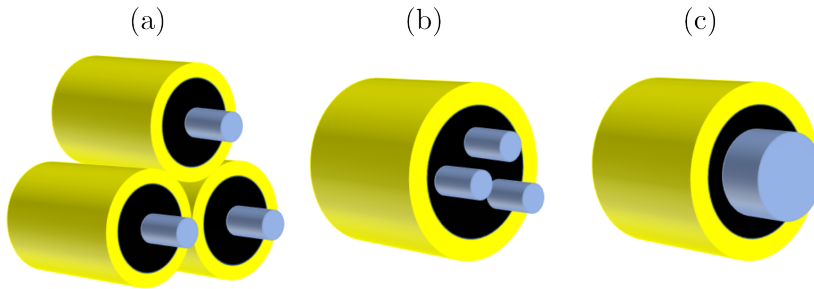


**Figure 1.2:** Different types of fiber for space-division multiplexing. (a) An array of single-core thin fibers (fiber bundle). (b) A multi-core fiber. (c) A few-mode fiber, i.e., a fiber that supports a designed number of modes.

practical solution to address the capacity crunch in the short term (see Fig. 1.3).

Capacity is not the only challenge that the next-generation communication network has to overcome. For instance, Internet access around the world is not uniform. The internet penetration, i.e., the percentage of total population that has access to the network, spans from an average of 89.7% in Europe [14], down to an average of 39.3% in Africa [15]. Even in the most developed countries, similar issues affect less densely populated areas that are generally close to the fiber backbone but do not have access to it. This problem is known as

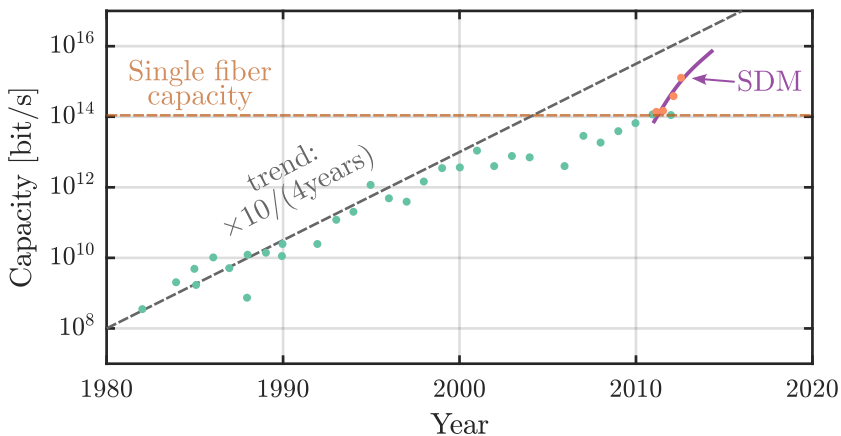


**Figure 1.3:** Capacity trend of communication systems over the years. SDM provides a solution to increase the capacity of communication systems beyond the limits imposed by the single fiber. Data is taken from Ref. [5].

“last mile access” [16]. Ideally, everyone should gain access to the optical fiber-based network, which grants maximum data rates. However, due to the high installation costs, this is not feasible, especially in less populated or hard-to-reach areas [17]. Radio frequency (RF) and microwave connectivity are the most common solutions to this problem. However, the main disadvantage is that they are severely limited in bandwidth and cannot support high throughput for multiple users [18]. An alternative solution is represented by free-space optical communications (FSO). FSO involves sending information through an unguided propagation medium using optical frequencies ranging from infrared to ultraviolet light. FSO offers various attractive features [19]:

- very large bandwidth;
- no license fee, since the optical spectrum is not covered by the telecommunications regulations;
- lower cost of installation and maintenance;
- lower power consumption;
- inherent security, thanks to the high directionality of the laser beams carrying the signals;
- immunity to RF electromagnetic interference;
- compatibility with the fiber optics network;
- straightforward implementation of SDM to increase the system capacity (array of laser beams).

The main challenge in FSO lies in atmospheric effects, such as absorption, scattering, and atmospheric turbulence [20]. In particular, atmospheric turbulence introduces intensity scintillation, phase distortion, and modal coupling. To reduce the impact of atmospheric effects, the use of partially coherent light has been proposed. Relying on partial coherence significantly reduces the bit-error rate, compared to its coherent counterpart [21].

It is clear from this overview that the science of communication will face major challenges in the coming years. To meet these challenges, simply improving existing technologies will most likely not be sufficient. We need to assume a new perspective that goes beyond traditional communication systems, and dare to explore innovative platforms. In this light, we took inspiration from existing solutions (SDM and partial coherence for FSO) to envision a potential

---

new route. Let us consider the four fibers in Fig. 1.4, that can be collected in a fiber bundle or a multi-core fiber, taking advantage of the platforms developed for SDM. Standard communication techniques would maximize the capacity of each single fiber, treating each transmitted field as an independent signal. However, we can also imagine a different scenario. Instead of employing each transmitted beam as an independent carrier, we assume that we can encode the information in the correlation between each pair of fields (*mutual coherence*). In this case, the number of signals would not be given by the number of fields ( $N_f = 4$ ), but by the number of field *pairs*  $N_p = 6$ , thus effectively increasing the number of transmitted signals without modifying the physical transmission line. This promising improvement becomes more relevant when we generalize this principle to an arbitrary number of fibers  $N_f$ , obtaining a quadratic scaling of the number of signals  $N_p$  with the number of transmitted fields:

$$N_p = \binom{N_f}{2} = \frac{N_f(N_f - 1)}{2}. \quad (1.1)$$

This observation leads to the central question of this thesis: can we effectively use mutual coherence to increase the capacity of a communication system? We develop our answer in three main points, which we can summarize as follows:

- we theoretically present a technique to independently control the mutual coherence of a set of fields through a linear transformation (Ch. 2);
- we analyze the performance of a communication system which encodes the data in the mutual coherences of a set of transmitted fields (Ch. 3);

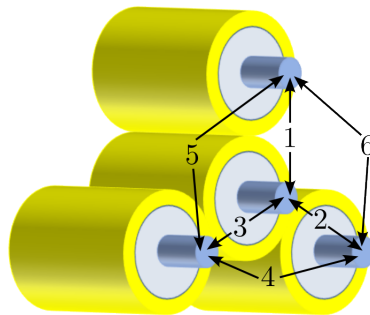


**Figure 1.4:** Encoding information in the mutual coherence of spatially separated fields. The number of signals scales quadratically with the number of transmitted fields.



- we experimentally realize the control of the mutual coherences of several fields, employing a spatial light modulator and a complex medium to implement a linear port (Ch. 4).

# 2

---

## Coherence control: theoretical background

Coherence is a fundamental notion in the science of light and offers a central degree of freedom to manipulate electromagnetic radiation of diverse physical character [22]. It accounts for the statistical properties of the electromagnetic radiation [23]. Not only has the study of optical coherence been crucial to the foundations and development of modern optics [24], but it has also found countless applications in optical technology, e.g., in imaging [25, 26], tomography [27–29], beam propagation [30], nanophotonics [31, 32], trapping [33–36], and free-space optical communications [21, 37].

In this chapter, we will provide the background concepts needed to understand the theory of optical coherence. Moreover, we present a method to generate a set of  $n$  fields with precisely controlled mutual coherences through an  $n \times n$  linear transformation.

### 2.1 Basic definitions

Here, we introduce two ways of treating the polychromatic fields analytically: the real field, which is the actual electric field as given by Maxwell's equations in time domain, and the complex representation, which is a convenient and powerful tool that simplifies many calculations. We then show that the two representations are equivalent, allowing us to work with complex fields for the rest of the document. We continue defining important quantities, such as

the autocorrelation of the fields, the power spectral density, the power and the first-order coherence. We then introduce the concept of mutual coherence and present two methods to experimentally measure it. Finally, we define the coherence matrix, highlighting its most relevant properties.

### 2.1.1 Non-monochromatic fields

In the field of optics, we commonly deal with monochromatic fields, which, at a given point  $P$ , are characterized by a constant amplitude and a phase that varies linearly with time [23]. This important approximation often well applies to the analysis of phenomena involving laser light, due to its narrow linewidth. However, even the sharpest spectral line has a finite width. Thus, for a general treatment of light field, we need to consider polychromatic fields [23]. In this section, we will derive a set of mathematical tools and properties that will be useful in the investigation of non-monochromatic light.

Let us restrict ourselves to a Cartesian component of the electric field, represented by the real signal  $F^{(r)}(t)$ . This non-monochromatic field can be decomposed in a sum of monochromatic components, each with relative amplitude  $a(\nu)$  and phase  $\phi(\nu)$ , and expressed through a Fourier integral,

$$F^{(r)}(t) = \int_0^{\infty} a(\nu) \cos[\phi(\nu) - 2\pi\nu t] d\nu. \quad (2.1)$$

We now introduce the complex representation of the field, associating to  $F^{(r)}(t)$  a complex function of the form [23]

$$F(t) = \int_0^{\infty} a(\nu) e^{i\phi(\nu) - i2\pi\nu t} d\nu. \quad (2.2)$$

We will refer to this function as the *complex field*. Because  $F^{(r)}(t)$  is the real part of  $F(t)$ , it is convenient (due to the mathematical properties of complex exponentials) to calculate the effect of linear systems considering  $F(t)$ , and only at the end of the calculations take its real part to derive the expression of the real field.

We can derive another relation between the real and complex fields by expressing  $F^{(r)}(t)$  through its Fourier transform

$$F^{(r)}(t) = \int_{-\infty}^{\infty} \nu(\nu) e^{-i2\pi\nu t} d\nu. \quad (2.3)$$

For a real signal we have  $\nu(-\nu) = \nu^*(\nu)$ , so we retain the total spectral information if we consider only the positive frequencies. If we then recast the complex

variable  $\nu(\nu)$  with explicit amplitude and phase

$$\nu(\nu) = \frac{1}{2} a(\nu) e^{i\phi(\nu)} \quad \text{with } \nu \geq 0, \quad (2.4)$$

we realize that it is possible to express  $F(t)$  in terms of the Fourier coefficients of  $F^{(r)}(t)$ :

$$F(t) = 2 \int_0^\infty \nu(\nu) e^{-i2\pi\nu t} d\nu. \quad (2.5)$$

This result tells us that the complex field can be derived from the real one, setting to zero the amplitudes belonging to the negative frequencies, and multiplying by two the amplitudes associated to the positive frequencies. As we have already point out, thanks to the symmetry of the spectrum of real signals,  $F(t)$  and  $F^{(r)}(t)$  carry the same information, confirming that the complex representation of the field is to be considered equivalent to the real one.

Next, we define some properties of polychromatic fields, namely the autocorrelation, the power spectral density, the power and the first-order coherence. We highlight that we always consider *stationary* and *ergodic* fields. Stationarity implies that the ensemble average is independent of the origin of time, while ergodicity entails the equivalence between ensemble average and time average involving a single realization of the random process. The field autocorrelation  $\mathcal{R}_F(t_1, t_2)$  is defined as

$$\mathcal{R}_F(t_1, t_2) = \overline{F(t_1)F^*(t_2)}, \quad (2.6)$$

where the overline stands for ensemble average. Under the stationarity condition, the autocorrelation only depends on the difference  $\tau = t_1 - t_2$ , and not on the particular values of  $t_1$  and  $t_2$ . Thus, we can write

$$\mathcal{R}_F(\tau) = \overline{F(t+\tau)F^*(t)}, \quad (2.7)$$

The power spectral density can be derived from the expression of the autocorrelation, through the Wiener-Khinchin theorem [23], which states that the power spectral density  $S(\nu)$  and the autocorrelation  $\mathcal{R}_F(\tau)$  form a Fourier transform pair:

$$S(\nu) = \int_{-\infty}^\infty \mathcal{R}_F(\tau) e^{-2\pi i\nu\tau} d\tau. \quad (2.8)$$

We then define a fundamental quantity in optics, which is the power  $P_F$  of the field\*:

$$P_F = \langle F(t)F^*(t) \rangle, \quad (2.9)$$

---

\*We will equivalently use the term *intensity*  $I_F$  to refer to this quantity.

where the angle brackets stand for an infinite-time average, i.e.,

$$\langle X(t) \rangle = \lim_{T \rightarrow \infty} \frac{1}{T} \int_{-T/2}^{T/2} X(t) dt. \quad (2.10)$$

Since we are dealing with ergodic and stationary fields, we can write the power in terms of the autocorrelation and the power spectral density:

$$P_F = \langle F(t)F^*(t) \rangle = \overline{F(t)F^*(t)} = \mathcal{R}_F(0) = \int_{-\infty}^{\infty} S(\nu) d\nu. \quad (2.11)$$

The normalized version of the autocorrelation is known as *first-order coherence*  $g^{(1)}(\tau) = \mathcal{R}_F(\tau)/P_F$  [38]. In this thesis we will assume light fields with a Lorentzian power spectral density, characterized by linewidth  $\Delta\nu$  and central frequency  $\nu_0$  [38], i.e.,

$$S(\nu) = \frac{1}{\pi} \frac{\Delta\nu}{(\nu - \nu_0)^2 + (\Delta\nu)^2}, \quad (2.12)$$

which results in a  $g^{(1)}(\tau)$  of the form <sup>†</sup>:

$$g^{(1)}(\tau) = e^{-i2\pi\nu_0\tau - 2\pi\Delta\nu|\tau|}. \quad (2.13)$$

Finally, we introduce the concept of *narrow-band* field. Until now we considered a general polychromatic field, while in most practical cases (and for the entirety of this thesis) we are interested in narrow-band fields, i.e., fields that are characterized by a power spectral density whose amplitudes are non-negligible only in a spectral window much smaller than the central frequency  $\nu_0$ . We can express a narrow-band field  $F(t)$  with an explicit dependence on the oscillation frequency  $\nu_0$ , and characterized by real and time-dependent amplitude  $A(t)$  and phase  $\Phi(t)$ :

$$F(t) = A(t)e^{i\Phi(t) - i2\pi\nu_0 t}. \quad (2.14)$$

The field  $F(t)$  – similarly to a monochromatic field – is characterized by fast oscillations at the central frequency  $\nu_0$ , with  $A(t)$  and  $\Phi(t)$  that can be considered constant over many oscillation cycles. On top of the monochromatic behavior, however, amplitude and phase undergo random fluctuations, with a rate that is given by the inverse of the spectral linewidth ( $1/\Delta\nu$ ). For this reason, narrow-band fields are also known as *quasi-monochromatic* fields.

---

<sup>†</sup>Note that in Ref. [39], we used  $g^{(1)}(\tau) = \exp(-i2\pi\nu_0\tau - \Delta\nu|\tau|)$ . In this thesis, we added the factor  $2\pi$  to the linewidth to be more consistent with the literature.

### 2.1.2 Mutual coherence

The term *mutual coherence*<sup>‡</sup> quantifies the correlation between a pair of stochastic fields. The mutual coherence can be defined with respect to any degree of freedom, e.g., space (spatial coherence), time (temporal coherence), polarization (degree of polarization [40]), and transverse modes [41]. Most of this work deals with the special case of spatially separated optical beams. We represent two random, statistically stationary and ergodic, narrow-band scalar optical fields at two different points in space, but evaluated at the same time, by the complex signals  $F_i$  and  $F_j$ . The mutual coherence (also known as *equal-time degree of coherence* [23])  $\gamma_{ij}$  between  $F_i$  and  $F_j$  is defined as

$$\gamma_{ij} = \frac{\langle F_i F_j^* \rangle}{\sqrt{\langle |F_i|^2 \rangle \langle |F_j|^2 \rangle}}. \quad (2.15)$$

The mutual coherence is a normalized quantity, spanning from full incoherence ( $|\gamma_{ij}| = 0$ ) to partial ( $0 < |\gamma_{ij}| < 1$ ) to full coherence ( $|\gamma_{ij}| = 1$ ).

There are many ways to experimentally measure the mutual coherence, two of which are relevant to our treatment and will therefore be described below. In both cases we consider two quasi-monochromatic fields  $X_1$  and  $X_2$ , which propagate as collimated fundamental Gaussian modes, and are characterized by mutual coherence  $\gamma_{12}$ , and input powers  $P_1 = \langle |X_1|^2 \rangle$  and  $P_2 = \langle |X_2|^2 \rangle$ . In the first method, we direct the two beams towards a beam splitter, as depicted in Fig. 2.1. We then measure the intensities of the two output ports with a pair of photodetectors. The two fields  $Y_+$  and  $Y_-$  at the output ports are

$$Y_{\pm} = \frac{X_i \pm X_j}{\sqrt{2}}, \quad (2.16)$$

while the power measured by each photodetector is

$$P_{\pm} = \langle |Y_{\pm}|^2 \rangle = \frac{1}{2} \left[ \langle |X_1|^2 \rangle + \langle |X_2|^2 \rangle \pm 2\sqrt{\langle |X_1|^2 \rangle \langle |X_2|^2 \rangle} \operatorname{Re}(\gamma_{12}) \right]. \quad (2.17)$$

Measuring the input powers  $P_i = \langle |X_i|^2 \rangle$ , with  $i = \{1, 2\}$ , and the difference between  $P_+$  and  $P_-$ , we can calculate the real part of the mutual coherence  $\gamma_{12}$  as

$$\operatorname{Re}(\gamma_{12}) = \frac{P_+ - P_-}{4\sqrt{P_1 P_2}}. \quad (2.18)$$

---

<sup>‡</sup>Note that throughout the thesis, we will indifferently use the terms *mutual coherence*, *mutual degree of coherence* or simply *degree of coherence*.

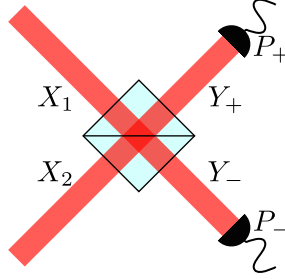


**Figure 2.1:** First method for the measurement of the mutual coherence. Two beams  $X_1$  and  $X_2$  are mixed with a beam splitter, resulting in the output fields  $Y_+$  and  $Y_-$ . Two photodetectors measure the output power, which is used to reconstruct the value of the mutual coherence between  $X_1$  and  $X_2$ .

In the second method, we measure the mutual coherence by interfering  $X_1$  and  $X_2$  at the focal plane of a low-NA lens. We sketch in Fig. 2.2a the optical setup considered, and the reference systems at the back and front focal planes of the lens. The total input field at the back focal plane  $F_{\text{in}}$  is given by the sum of  $X_1$  and  $X_2$ , which are collimated fundamental Gaussian modes centered at  $x = \pm x_0$ , respectively, and  $y = 0$ , with a beam waist  $w_0 \ll x_0$ :

$$F_{\text{in}} = \frac{X_1(t)}{\sqrt{2\pi}w_0} e^{-\frac{(x-x_0)^2+y^2}{2w_0^2}} + \frac{X_2(t)}{\sqrt{2\pi}w_0} e^{-\frac{(x+x_0)^2+y^2}{2w_0^2} + i\phi}, \quad (2.19)$$

where  $\phi$  is the relative phase difference between  $X_1$  and  $X_2$ , that we assume controllable. We calculate the focal field  $F_f$  through a 2D-Fourier transform with respect to the spatial variables  $x$  and  $y$  [42], obtaining a focal intensity

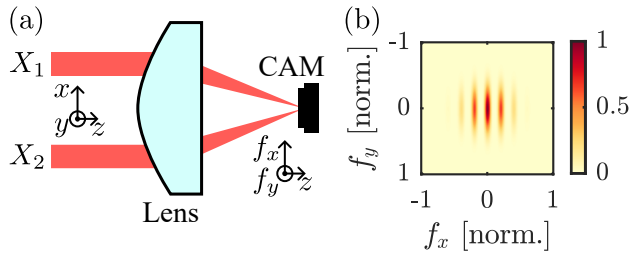


**Figure 2.2:** Second method for the measurement of the mutual coherence. (a) Two Gaussian beams are focused by a low-NA lens. We then measure the focal plane intensity with a camera. (b) Normalized intensity  $I_f$  measured in the focal plane. Here we have assumed  $\langle |X_1|^2 \rangle = \langle |X_2|^2 \rangle$ ,  $\phi = 0$  and  $\gamma_{12} = 1$ .

$I_f = \langle |F_f|^2 \rangle$  equal to

$$I_f = w_0^2 e^{-(f_x^2 + f_y^2)} w_0^2 \left[ \langle |X_1|^2 \rangle + \langle |X_2|^2 \rangle + 2\text{Re} \left( \langle X_1 X_2^* \rangle e^{2f_x x_0 - \phi} \right) \right], \quad (2.20)$$

where  $f_x$  and  $f_y$  are the spatial frequencies at the focal plane. In Eq. (2.20), we recognize the Gaussian envelope, modulated by the interference fringes arising from the cosine term. The intensity  $I_f$  is depicted in Fig. 2.2b, in the case of mutually coherent beams with same intensity, and relative phase  $\phi = 0$ .

We can recast Eq. (2.20) highlighting the role of the mutual coherence  $\gamma_{12}$ :

$$I_f \propto \langle |X_1|^2 \rangle + \langle |X_2|^2 \rangle + 2\sqrt{\langle |X_1|^2 \rangle \langle |X_2|^2 \rangle} |\gamma_{12}| \cos \left( \angle(\gamma_{12}) + 2f_x x_0 - \phi \right), \quad (2.21)$$

where  $\angle(\gamma_{12})$  is the phase of  $\gamma_{12}$ . It is then evident that the mutual coherence alters the interference fringes. In Figs. 2.3a and 2.3b, we show the intensity profile along  $f_x$  for different values of mutual coherence (we consider  $f_y = 0$ ,  $\langle |X_1|^2 \rangle = \langle |X_2|^2 \rangle = I_{\text{in}}$ , and we set the value of the relative phase to  $\phi = 0$ ). In Fig. 2.3a we modulate the magnitude of the mutual coherence, keeping constant its phase. Reducing the absolute value, the contrast of the interference fringes reduces, until we remain only with the Gaussian envelope for  $|\gamma_{12}| = 0$ . In Fig. 2.3b we instead keep constant the absolute value of the mutual coherence ( $|\gamma_{12}| = 1$ ), while we change its phase. This results in a shift of the interference fringes with respect to the Gaussian envelope. We obtain the same result modulating the relative phase  $\phi$  between  $X_1$  and  $X_2$ , as we can see from Eq. (2.21). We can use the dependence of the intensity  $I_f$  on the control parameter  $\phi$  to measure the degree of coherence. We choose a point in the camera plane, e.g.,  $f_x = f_y = 0$ , and we modulate  $\phi$  from 0 to  $2\pi$ , measuring the resulting intensity (see Fig. 2.3c). We then select the maximum  $I_{f,\text{max}}$  and minimum  $I_{f,\text{min}}$  intensities

$$\begin{aligned} I_{f,\text{max}} &= \langle |X_1|^2 \rangle + \langle |X_2|^2 \rangle + 2\sqrt{\langle |X_1|^2 \rangle \langle |X_2|^2 \rangle} |\gamma_{12}| \\ I_{f,\text{min}} &= \langle |X_1|^2 \rangle + \langle |X_2|^2 \rangle - 2\sqrt{\langle |X_1|^2 \rangle \langle |X_2|^2 \rangle} |\gamma_{12}| \end{aligned} \quad (2.22)$$

and we derive the *visibility*  $\mathcal{V}$ , defined as

$$\mathcal{V} = \frac{I_{f,\text{max}} - I_{f,\text{min}}}{I_{f,\text{max}} + I_{f,\text{min}}} = \frac{2\sqrt{\langle |X_1|^2 \rangle \langle |X_2|^2 \rangle}}{\langle |X_1|^2 \rangle + \langle |X_2|^2 \rangle} |\gamma_{12}|. \quad (2.23)$$

From the measurement of the visibility, and the single intensities of  $X_1$  and  $X_2$ ,



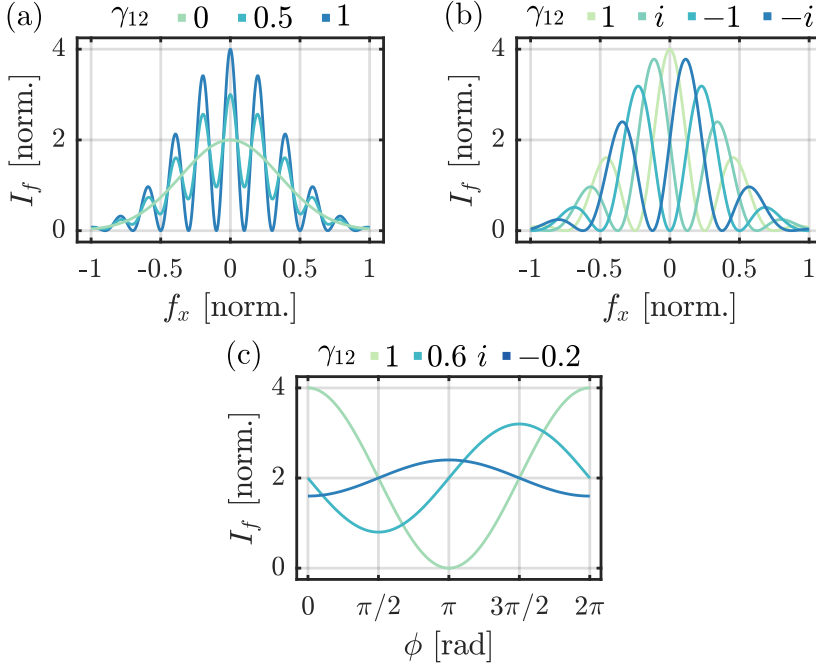


**Figure 2.3:** Interference fringes for different values of mutual coherence. (a,b) Intensity dependence on the spatial frequency  $f_x$  in the focal plane. (a) Changing the magnitude of  $\gamma_{12}$ , the contrast of the interference fringes reduces accordingly. (b) If we change the phase of the mutual coherence keeping the absolute value constant ( $|\gamma_{12}| = 1$ ), we measure a shift of the maxima and minima with respect to the Gaussian envelope. (c) Dependence of the intensity in a single point of the focal plane ( $f_x = f_y = 0$ ) on the relative phase difference  $\phi$  between the two interfering fields  $X_1$  and  $X_2$ .

we can calculate the magnitude of  $\gamma_{12}$ :

$$|\gamma_{12}| = \mathcal{V} \frac{\langle |X_1^2| \rangle + \langle |X_2^2| \rangle}{2\sqrt{\langle |X_1^2| \rangle \langle |X_2^2| \rangle}}. \quad (2.24)$$

The phase of the mutual coherence  $\angle(\gamma_{12})$ , instead, can be directly measured from the initial phase of the cosine modulation of  $I_f$ .

### 2.1.3 Coherence matrix

Let us generalize the concept of mutual coherence to a set of  $n$  fields  $F_i$ , with  $i = 1, 2, \dots, n$ , located at  $n$  different points in space. We start collecting the  $n$

fields in a normalized column vector  $\mathbf{F} = [F_1/\sqrt{I_1}, F_2/\sqrt{I_2}, \dots, F_n/\sqrt{I_n}]^\top$ , where  $I_i = \langle |F_i|^2 \rangle$  and the symbol  $\top$  denotes the transpose of the vector. In analogy with the definition of mutual coherence given in Eq. (2.15), we define a new quantity  $\mathbb{K}$  as

$$\mathbb{K} = \langle \mathbf{F} \mathbf{F}^\dagger \rangle, \quad (2.25)$$

where the dagger denotes conjugate transpose, and the angle brackets a time average. The matrix  $\mathbb{K}$  is known as *coherence matrix* (or, more specifically, *spatial coherence matrix*, since we are here dealing with spatially separated light fields). The diagonal elements of the matrix are the self degrees of coherence  $\gamma_{ii}$ , which are always equal to 1, and the off-diagonal terms are the values of mutual coherence  $[\mathbb{K}_{ij}] = \gamma_{ij}$ . The coherence matrix is also known as a statistical correlation matrix, which is a normalized covariance matrix, and must be Hermitian and positive semi-definite [43]. These conditions make the values of the degrees of coherence mutually dependent. We will now analytically derive this dependence, and set a more strict condition that allows us to independently choose the elements of the coherence matrix. Since  $\mathbb{K}$  is Hermitian, we have

$$\gamma_{ji} = \gamma_{ij}^*, \quad (2.26)$$

while the condition for positive definite matrices is [44]

$$\frac{\text{tr}(\mathbb{K})^2}{\text{tr}(\mathbb{K}^2)} > n - 1, \quad (2.27)$$

where  $\text{tr}$  stands for the matrix trace, and  $n$  is the dimension of  $\mathbb{K}$ , i.e., the number of spatially separated fields in the system. Since we also want to include the positive semi-definite matrices, we generalize the condition above to have<sup>§</sup>

$$\frac{\text{tr}(\mathbb{K})^2}{\text{tr}(\mathbb{K}^2)} \geq n - 1. \quad (2.28)$$

The diagonal elements of  $\mathbb{K}$  are all equal to 1, hence

$$\text{tr}(\mathbb{K})^2 = n^2. \quad (2.29)$$

The diagonal elements of  $\mathbb{K}^2$  are

$$\text{diag}(\mathbb{K}^2) = \sum_{j=1}^n \gamma_{ij} \gamma_{ji} = \sum_{j=1}^n \gamma_{ij} \gamma_{ij}^*, \quad (2.30)$$

---

<sup>§</sup>Note, however, that there exists positive semi-definite matrices which do not satisfy Eq. (2.28), which is a sufficient but not necessary condition. An example is given by the fully coherent system, which is represented by a coherence matrix where all the elements are 1.

where in the last passage we used the Hermitian property of  $\mathbb{K}$  [Eq. (2.26)]. Therefore we get that the trace is

$$\text{tr}(\mathbb{K}^2) = \sum_{i=1}^n \sum_{j=1}^n |\gamma_{ij}|^2. \quad (2.31)$$

Combining Eqs. (2.28), (2.29) and (2.31), we obtain a condition on the absolute values of the degrees of coherence

$$\sum_{i=1}^n \sum_{j=1}^n |\gamma_{ij}|^2 \leq \frac{n^2}{n-1}. \quad (2.32)$$

This condition ensures that the coherence matrix is physically meaningful. We find a stricter condition choosing all mutual coherences with the same absolute value, i.e.,  $|\gamma_{ij}| = |\gamma| \forall i, j$ , leading to

$$|\gamma| \leq \frac{1}{n-1}. \quad (2.33)$$

Equations (2.32) and (2.33) ensure that the coherence matrix is positive semi-definite if we choose

$$|\gamma_{ij}| < \frac{1}{n-1} \quad \forall i, j. \quad (2.34)$$

The interest in this sufficient condition resides in the fact that, if satisfied, we can choose the value of each mutual coherence independently of the others.

From the coherence matrix, we can also characterize the *overall coherence*  $\mathcal{S}$  of the system, employing the measure [45]

$$\mathcal{S} = \frac{n}{n-1} \left[ \frac{\text{tr}(\mathbb{K}^2)}{\text{tr}(\mathbb{K})^2} - \frac{1}{n} \right], \quad (2.35)$$

where  $\text{tr}$  stands for matrix trace. The overall coherence is normalized such that  $0 \leq \mathcal{S} \leq 1$ . The upper bound  $\mathcal{S} = 1$  is saturated exclusively when all fields are mutually fully coherent ( $|\gamma_{ij}| = 1$ ), hence corresponding to a completely coherent system. The lower bound  $\mathcal{S} = 0$ , on the other hand, is met only when all fields are mutually fully incoherent ( $|\gamma_{ij}| = 0$ , for  $i \neq j$ ), in which case the whole system is fully incoherent and the coherence matrix is equal to the identity matrix ( $\mathbb{K} = \mathbb{I}$ ).

## 2.2 Coherence matrix control with linear transformation

In this section, we will describe the important technique which allows us to control the coefficients of the coherence matrix employing a linear transformation.

### 2.2.1 Coherence control with mutually incoherent fields

We consider here  $n$  *mutually incoherent* input fields, which we can represent with the column vector  $\mathbf{F}_{\text{in}}$ . Since in this case all mutual degrees of coherence are zero, whereupon the overall coherence of the whole system is also zero, the input coherence matrix obeys

$$\mathbb{K}_{\text{in}} = \langle \mathbf{F}_{\text{in}} \mathbf{F}_{\text{in}}^\dagger \rangle = \mathbb{I}. \quad (2.36)$$

We combine the input fields via a linear transformation  $\hat{T}$ , according to

$$\mathbf{F}_{\text{out}} = \hat{T} \mathbf{F}_{\text{in}}, \quad (2.37)$$

where  $\mathbf{F}_{\text{out}}$  is the vector describing the output fields. The output coherence matrix is then given by

$$\mathbb{K}_{\text{out}} = \langle \mathbf{F}_{\text{out}} \mathbf{F}_{\text{out}}^\dagger \rangle = \langle \hat{T} \mathbf{F}_{\text{in}} \mathbf{F}_{\text{in}}^\dagger \hat{T}^\dagger \rangle. \quad (2.38)$$

Using the fact that  $\hat{T}$  is deterministic and time-independent and the inputs are mutually incoherent, we obtain

$$\mathbb{K}_{\text{out}} = \hat{T} \langle \mathbf{F}_{\text{in}} \mathbf{F}_{\text{in}}^\dagger \rangle \hat{T}^\dagger = \hat{T} \mathbb{K}_{\text{in}} \hat{T}^\dagger = \hat{T} \hat{T}^\dagger. \quad (2.39)$$

Therefore, it is possible to generate an arbitrary output coherence matrix upon choosing a linear transformation which fulfills

$$\hat{T} = \sqrt{\mathbb{K}_{\text{out}}}, \quad (2.40)$$

where the square root is the principal square root of the matrix. The positive semi-definiteness of the coherence matrix ensures the existence of such a linear transformation [43]. We note that the assumption of mutually incoherent input fields is not necessary to control the output coherence, yet it simplifies the treatment, as indicated by Eqs. (2.39) and (2.40). In the next section, we will derive the case of mutually partially coherent input fields.

Finally, we observe from Eq. (2.39) that, under unitary transformations, i.e.,  $\hat{T} \hat{T}^\dagger = \hat{T}^\dagger \hat{T} = \mathbb{I}$ , the output coherence matrix always obeys  $\mathbb{K}_{\text{out}} = \mathbb{K}_{\text{in}} = \mathbb{I}$  for an incoherent input system. The control of the output coherence thus relies on the nonunitary character of the chosen transformation. We can prove that unitary transformations cannot affect the overall coherence of a given system, regardless the form of  $\mathbb{K}_{\text{in}}$ . Demonstrating this general statement is the topic of App. B.1.

### 2.2.2 Coherence control with mutually partially coherent fields

Let us now consider input fields with a general coherence matrix  $\mathbb{K}_{\text{in}}$ . Because the input coherence matrix is positive semi-definite, we can diagonalize it, i.e.,

$$\mathbb{K}_{\text{in}} = \mathbb{V} \sqrt{\mathbb{D}} \sqrt{\mathbb{D}}^\dagger \mathbb{V}^\dagger, \quad (2.41)$$

where  $\mathbb{V}$  is a unitary matrix and  $\mathbb{D}$  is a diagonal matrix. Moreover, the positive semi-definiteness implies that the eigenvalues are real and non-negative, allowing us to take the square root of the diagonal matrix  $\mathbb{D}$ . Applying the linear transformation  $\hat{T}$ , we obtain the output coherence matrix

$$\mathbb{K}_{\text{out}} = \hat{T} \mathbb{K}_{\text{in}} \hat{T}^\dagger = \hat{T} \mathbb{V} \sqrt{\mathbb{D}} \sqrt{\mathbb{D}}^\dagger \mathbb{V}^\dagger \hat{T}^\dagger = \mathbb{M} \mathbb{M}^\dagger. \quad (2.42)$$

A relation analogous to Eq. (2.40) now applies to the matrix  $\mathbb{M} = \hat{T} \mathbb{V} \sqrt{\mathbb{D}}$ . Thus, given a desired output coherence matrix, the linear transformation  $\hat{T}$  must take the form

$$\hat{T} = \sqrt{\mathbb{K}_{\text{out}}} \left( \sqrt{\mathbb{D}} \right)^{-1} \mathbb{V}^{-1}. \quad (2.43)$$

This form is more difficult to implement experimentally. In fact, it requires to carefully characterize the input coherence matrix. On the other hand, obtaining mutually incoherent inputs is straightforward, since it simply requires the use of different lasers as input fields, or to split a single laser in multiple beams and introduce a propagation delay between one another much longer than the coherence time.

# 3

---

## Encoding information in the mutual coherence

Coherence has been used as a resource for optical communications since its earliest days. In particular, a coherence-based multiplexing technique (known as *coherence multiplexing*) has been proposed as the first coherent optical code-division multiple access (CDMA) technique [46, 47]. Its appeal (in common with other CDMA techniques [47]) lies in the fact that multiple users share the same optical bandwidth, thus relaxing the requirements for wavelength control, and transmit asynchronously to each other, allowing multiple access without requiring any scheduling [48]. Coherence multiplexing, in all the proposed configurations [46, 49, 50], makes use of optical coherence to discriminate one pair of transmitted signal-reference beams from all the other pairs. Although this CDMA technique uses coherence as a resource for multiplexing, its data encoding scheme still relies on the relative optical path difference between two fields, requiring each signal to have a dedicated reference. The presence of the reference fields is detrimental for many reasons:

- it doubles the number of signals to be multiplexed, affecting the system complexity and the noise performance [51–54];

---

This chapter is based on the article: Alfonso Nardi, Shawn Divitt, Massimiliano Rossi, Felix Tebbenjohanns, Andrei Militaru, Martin Frimmer, and Lukas Novotny, *Encoding information in the mutual coherence of spatially separated light beams*, "Opt. Lett. 47, 4588-4591 (2022)

- the losses associated to the beam splitting and recombination needed for the reference are a limiting factor to the large-scale practical implementation of coherence multiplexing [55].
- the length of the delay lines employed to distinguish between different reference fields scales exponentially with the number of multiplexed signals [56].

The need of the reference field can be eliminated by encoding information directly into the mutual coherence between pairs of transmitted light beams. In Sec. 2.2, we showed that, implementing a suitable optical linear port, we can independently control the mutual coherence between pairs of spatially separated light beams. Using this technique, the transmitted fields would be mutually referenced, without requiring the long delay lines and the lossy beam splitting needed to generate the dedicated references. This reference-less, coherence-based coding scheme is termed *mutual coherence coding*. Interestingly, by encoding information in the mutual coherence between field pairs, we gain a quadratic scaling of the number of transmitted signals with the number of transmitted light beams. In fact, considering  $N_f$  transmitted fields, the number of signals equals the number of field pairs, that is  $N_p = N_f(N_f - 1)/2$ .

We open the chapter by introducing the basic theory to analyze a general communication system. We then proceed describing the specific implementation of mutual coherence coding, and providing the dependence of relevant figures of merit (signal-to-noise ratio, maximum bit-rate and spectral efficiency) on the number of transmitted beams. We conclude with a discussion on the benefit and limitations of the proposed communication scheme.

## 3.1 Optical communications

In this section, we provide an essential theoretical description of a communication system. We first present the general scheme which allows information to flow from a sender to a receiver, describing each of the building blocks composing the system. We then continue illustrating the concept of multiplexing. We conclude using the presented formalism to describe the coherence multiplexing communication scheme.

### 3.1.1 General communication scheme

A general communication system is shown schematically in Fig. 3.1. It is composed of five essential building blocks [57, 58]:

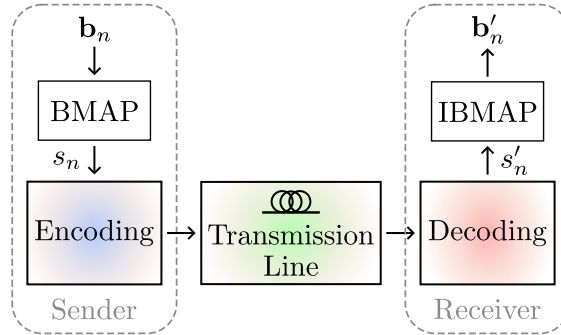


**Figure 3.1:** General scheme of a communication system. A binary word ( $\mathbf{b}_n$ ) is converted into a symbol  $s_n$  through a bit-map (BMAP). The symbol is then encoded into a physical signal, which is sent to the receiver through a transmission line. The received signal is translated into the symbol  $s'_n$  by a decoder and finally translated to a binary word  $\mathbf{b}'_n$  with an inverse bit-map (IBMAP). If the received binary word  $\mathbf{b}'_n$  is equal to the sent one  $\mathbf{b}_n$ , the communication was successful.

1. **Bit map (BMAP)** – The goal of a communication system is to send a *message* from the sender to the receiver. The message can be of various types, from a sequence of letters or numbers, to a continuous function of time [57]. Regardless the type, it is convenient to express the message as a series of bits [57]

$$\{\dots, b_{-1}, b_0, b_1, b_2, \dots, b_l, \dots\}. \quad (3.1)$$

We call the coefficients  $b_n$  *symbols*, while the set of values that they can assume is named *alphabet* [58]. In case of bits, the symbols  $b_n$  belong to a binary alphabet (e.g.,  $b_n \in \{0, 1\}$  or  $b_n \in \{-1, 1\}$ ). While the abstract representation of the message can always be expressed as a series of bits without any drop in performance, it is convenient that the physical signal to be transmitted assumes an arbitrary value inside a larger alphabet. In fact, the larger the alphabet, the higher the amount of information that is contained in each transmitted symbol. Let us consider a physical signal that can assume  $M$  possible values, and that we use to encode a symbol  $s_n$ . Then, the symbol  $s_n$  belongs to an  $M$ -ary alphabet ( $s_n \in \{v_1, v_2, \dots, v_M\}$ ), and carries a number of bits  $n_b$  given by [57]

$$n_b = \log_2(M). \quad (3.2)$$

A sequence of bits  $n_b$  forms a *binary word*  $\mathbf{b}_n$ . We can define a BMAP,



which maps one-to-one the binary word  $\mathbf{b}_n$  to a symbol  $s_n$ :

$$\mathbf{b}_n = [b_0, b_1, \dots, b_{n_b}] \xrightarrow{\text{BMAP}} s_n = \text{BMAP}(\mathbf{b}_n). \quad (3.3)$$

In this way, we translate the message, expressed in the binary word, in the symbol to be encoded in the physical signal. We highlight that throughout this work we will not assume any particular BMAP, in order to keep the treatment as general as possible. We will instead work directly with a symbol  $s_n$  belonging to the largest alphabet allowed by the signal-to-noise ratio (for more details, see Sec. 3.2.2).

2. **Encoding** – Once the binary word is mapped into the symbol, a physical carrier is needed to transmit the information to the receiver. In optical communications, the symbol is encoded in a specific degree of freedom of the light field, e.g., amplitude, phase, frequency, or, in the case covered in this thesis, mutual coherence. The modulator implementing the encoding operation depends on the particular communication scheme chosen, thus it must be independently analyzed for each case.
3. **Transmission line** – We refer to the physical channel connecting the sender to the receiver as the transmission line. When the carrier is the light field, the channel often involves the use of optical fibers, even though free-space optical communications is emerging as an alternative [19]. Along the transmission line, the signal is perturbed by an additive white Gaussian noise (AWGN) [57, 58]. More specifically, denoting as  $N(t)$  the noise realization at time  $t$ , one has that  $N(t)$  is:

- *additive*: it is simply added to the transmitted signal, i.e., if  $Y(t)$  is the transmitted signal at the sender side, the received signal  $\tilde{Y}(t)$  is

$$\tilde{Y}(t) = Y(t) + N(t). \quad (3.4)$$

Moreover, the variance of the noise  $N(t)$  does not depend on the signal  $Y(t)$ .

- *white*: the power spectral density of the noise is constant over the bandwidth of interest of the communication system. Considering that the channel introduces a cut-off frequency  $\Delta\nu_N$  (much larger than the bandwidth of detectors and modulators [10]) the noise autocorrelation  $\mathcal{R}_{\mathcal{N}}(\tau)$  is

$$\mathcal{R}_{\mathcal{N}}(\tau) = \overline{N(t+\tau)N^*(t)} = P_N e^{-2\pi\Delta\nu_N|\tau|}, \quad (3.5)$$

where  $P_N$  is the noise power. Moreover, white noise has zero mean;

- *Gaussian*: the noise has a Gaussian probability density function. This implies that it is fully specified by its mean (zero in case of white noise) and its variance.

4. **Decoding** – The receiver gets the transmitted signal  $\tilde{Y}(t)$ , from which we want to extract the encoded symbol. The decoder has various implementations, depending on the encoding technique used. Nevertheless, it always includes a photodetector, which is used to convert the optical signal into an electronic one, that can be read digitally. We model the operation of the detector  $\mathcal{D}$  on the field  $F(t)$  as:

$$\mathcal{D}[F(t)] = \frac{1}{T} \int_{-T/2}^{T/2} |F(t)|^2 dt = \langle |F(t)|^2 \rangle_T, \quad (3.6)$$

where  $T$  is the integration time of the detector. From the photodetector measurement we can extract the perturbed symbol  $s'_n$ . The relationship between the symbol and the measurement depends on the particular communication scheme. In absence of noise, we have that the decoded value is equal to the encoded one ( $s'_n = s_n$ ).

5. **Inverse bit-map** – the inverse bit-map (IBMAP) finally translates the reconstructed symbol  $s'_n$  into the binary word  $\mathbf{b}'_n$ :

$$\mathbf{b}'_n = [b'_0, b'_1, \dots, b'_{n_b}] = \text{IBMAP}(s'_n). \quad (3.7)$$

If  $\mathbf{b}'_n = \mathbf{b}_n$ , the message is successfully sent.

### 3.1.2 Multiplexing

In the previous paragraph, we restricted ourselves to the case of a single carrier, hence a single symbol per detection period  $T$ . Multiplexing serves to maximize the information throughput by combining different signals into the same transmission line. This can be done by encoding symbols into orthogonal vectors of a given basis, allowing us to mix different fields and separate them at the receiver side. The available bases cover all degrees of freedom of light, the most commonly used of which are time [59], polarization [60], space [5], orbital angular momentum [61, 62], and wavelength [63]. The selected basis determines the particular multiplexing method.

For our treatment, two multiplexing methods are relevant. The first one is space division multiplexing (which we have already illustrated in Ch. 1). In the analysis of mutual coherence coding, in fact, we consider a transmission

line composed of multiple, non-interacting transmission paths, that can be implemented using fiber bundles or multi-core fibers [5]. The second method relevant to our discussion is coherence multiplexing, which we will illustrate in the following example.

### 3.1.3 Example: coherence multiplexing

Hereafter we outline the theory of coherence multiplexing and show how it differs from mutual coherence coding. This also offers the opportunity to summarize the concepts presented so far in a practical example.

Let us first focus on a single carrier, in order to understand the modulation principle at the core of coherence multiplexing. The scheme is depicted in Fig. 3.2. The binary message is translated through the BMAP into the symbol  $a_n$ . A light source characterized by a short coherence time  $\tau_c = 1/(2\pi\Delta\nu)$  (e.g, an LED), where  $\Delta\nu$  is the linewidth, feeds a Mach-Zender interferometer (MZI). The symbol  $a_n$  is encoded by setting the phase of one of the two branches of the MZI, while the other branch introduces a delay time  $\tau_d$  much longer than the coherence time  $\tau_c$ . We translate the symbol  $a_n$  into a phase level  $\phi_n$ , following

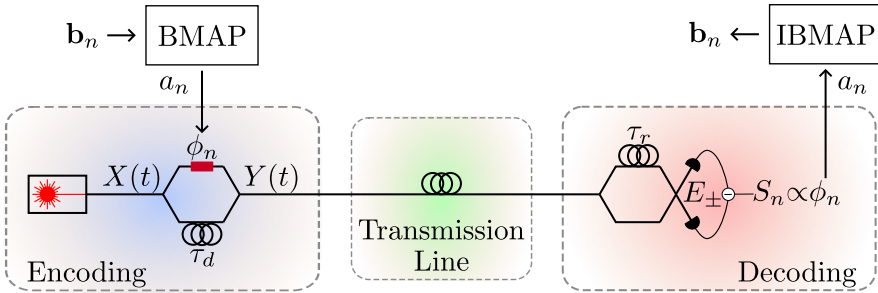


**Figure 3.2:** Coherence multiplexing with a single signal carrier. A BMAP translates the binary word  $\mathbf{b}_n$  into the symbol  $a_n$ . A field  $X(t)$  enters a MZI, which produces a reference field that undergoes a delay  $\tau_d$  and a signal field passing through a phase modulator. The symbol  $a_n$  is encoded into the phase  $\phi_n$  of the signal field via the phase modulator. The output field of the MZI  $Y(t)$  comprising the signal and reference fields is then transmitted. At the receiver side, another MZI and a balanced photodetector are used to measure the encoded phase  $\phi_n$ , from which we can extract the transmitted symbol  $a_n$  and convert it back to the binary word  $\mathbf{b}_n$ . For the communication scheme to work, the delay of the receiving MZI ( $\tau_r$ ) and of the transmitting MZI ( $\tau_d$ ) must be the same, i.e.,  $\tau_r = \tau_d$ .

the rule

$$\phi_n = \frac{a_n}{M-1} 2\pi, \quad a_n \in \{0, 1, \dots, M-1\}. \quad (3.8)$$

Therefore, if  $X(t)$  is the field at the input of the MZI, the output beam  $Y(t)$  is

$$Y(t) = \frac{X(t + \tau_d) + X(t)e^{i\phi_n}}{2}. \quad (3.9)$$

The field  $Y(t)$  is then sent to the receiver, traveling through the transmission line, where it adds up with a noise realization  $N(t)$ , leading to the received signal  $\tilde{Y}(t) = Y(t) + N(t)$ . The decoder is again a MZI, with one of the two arms introducing a delay  $\tau_r$ . The output fields of the receiver MZI are

$$E_{\pm} = \frac{\tilde{Y}(t + \tau_r) \pm \tilde{Y}(t)}{2}, \quad (3.10)$$

and they are measured by a balanced photodetector [64]. The signals  $\mathcal{D}[E_{\pm}]$  of the two detectors are

$$\mathcal{D}[E_{\pm}] = \langle |E_{\pm}|^2 \rangle_T = \frac{1}{4} \left[ \langle |\tilde{Y}(t + \tau_r)|^2 \rangle_T + \langle |\tilde{Y}(t)|^2 \rangle_T \pm 2\text{Re} \left( \langle \tilde{Y}(t + \tau_r) \tilde{Y}^*(t) \rangle_T \right) \right], \quad (3.11)$$

leading to the measured value

$$S_n = \mathcal{D}[E_+] - \mathcal{D}[E_-] = \text{Re} \left( \langle \tilde{Y}(t + \tau_r) \tilde{Y}^*(t) \rangle_T \right). \quad (3.12)$$

Let us analyze the signal  $S_n$ . We consider here only the expectation value of  $S_n$  (a thorough noise analysis of this scheme can be found in Refs. [51–54]), i.e.,

$$\overline{S_n} = \text{Re} \left( \frac{1}{T} \int_{-T/2}^{T/2} \overline{[Y(t + \tau_r) + N(t + \tau_r)] [Y^*(t) + N^*(t)]} dt \right). \quad (3.13)$$

Since the noise  $N(t)$  and the signal  $Y(t)$  are uncorrelated, and the correlation time of the noise  $\tau_N = 1/(2\pi\Delta\nu_N)$  is much smaller than the introduced delay  $\tau_r$ , we have that  $\overline{Y(t + \tau_r)N^*(t)} = \overline{N(t + \tau_r)Y^*(t)} = \overline{N(t + \tau_r)N^*(t)} = 0$ , hence

$$\overline{S_n} = \text{Re} \left( \frac{1}{T} \int_{-T/2}^{T/2} \overline{Y(t + \tau_r)Y^*(t)} dt \right) = \text{Re} \left( \overline{Y(t + \tau_r)Y^*(t)} \right), \quad (3.14)$$

where in the last equality we used the fact that the autocorrelation  $\mathcal{R}(\tau_r) = \overline{Y(t + \tau_r)Y^*(t)}$  does not depend on the absolute time  $t$ , but only on the time difference  $\tau_r$ . Writing Eq. (3.14) in terms of the input field  $X$ , we get

$$\overline{S_n} = \frac{1}{4} \text{Re} \left\{ \overline{[X(t + \tau_d + \tau_r) + X(t + \tau_r)e^{i\phi_n}] [X^*(t + \tau_d) + X^*(t)e^{-i\phi_n}]} \right\}, \quad (3.15)$$

which contains many terms of the form

$$\overline{X(t_1)X^*(t_2)} = P_X g_X^{(1)}(t_2 - t_1) = P_X e^{-i2\pi\nu_0(t_2-t_1) - |t_2-t_1|/\tau_c}, \quad (3.16)$$

where  $P_X$  is the input power. If the output delay matches the input one, i.e.,  $\tau_d = \tau_r$ , and neglecting all the terms for which  $|t_2 - t_1| \gg \tau_c$ , we get

$$\overline{S_n} = \frac{1}{4} \operatorname{Re} \left[ \overline{X(t + \tau_r)X^*(t + \tau_d)} e^{i\phi_n} \right] = \frac{P_X \cos \phi_n}{4}. \quad (3.17)$$

Therefore, from the signal measured by the balanced photodetector we can extract the encoded phase  $\phi_n$ . From the extracted phase level we can then infer the transmitted symbol  $a_n$ , which is translated back into the binary word  $\mathbf{b}_n$  with an IBCMAP\*.

So far we have outlined a communication system that is seemingly based on phase modulation only, and where coherence plays a secondary role. However, there is an important point to be noted. We considered a single-mode fiber in the transmission line, but two beams traveling: the one carrying the signal and its dedicated reference. Without the use of coherence, we would have to transmit two separate fields: the reference  $X(t)$  and the modulated version  $X(t)e^{i\phi_n}$  (see Fig. 3.3). Instead, due to the long delay lines in the MZIs, the two beams  $X(t + \tau_d)$  and  $X(t)e^{i\phi_n}$  are mutually incoherent, allowing us to incoherently sum them in the same single-mode fiber. At the receiver side, an equally long delay  $\tau_r = \tau_d$  is used to make the two beams  $X(t + \tau_d)$  and  $X(t + \tau_r)e^{i\phi_n}$  again perfectly mutually coherent, such that we are able to extract the phase  $\phi_n$  from an interference experiment. Therefore, coherence is used for multiplexing the

\*In the rest of the document, the stages of BMAP and IBCMAP will always be implicit.

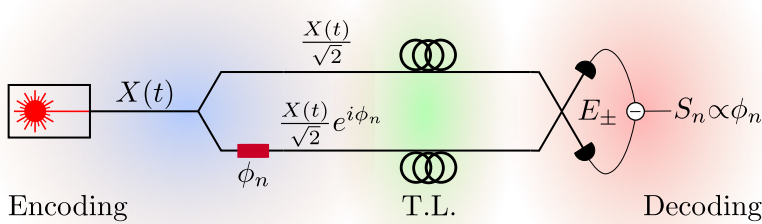


**Figure 3.3:** Communication scheme based on phase modulation. The reference field and the signal field (carrying the signal encoded in the phase  $\phi_n$ ) are transmitted in two separate channels. The two transmitted fields are then combined and measured by a balanced photodetector to extract the phase  $\phi_n$ .

signal-reference pair, while the information is stored in the phase of the field. This is important to keep in mind when we will analyze mutual coherence coding (Sec. 3.3). In fact, in mutual coherence coding, coherence is used to directly encode the information to be transmitted, while the multiplexing is performed by other means (e.g., space division multiplexing).

Coherence multiplexing can also be extended to a set of  $N_f$  fields, which we modulate independently. The communication system is depicted in Fig. 3.4. We consider a set of  $N_f$  input beams, each one modulated by a dedicated MZI. It is important to note that the delays of the MZIs are different and increasing in length [56], such that

$$\tau_c \ll \tau_1 \ll \tau_2 \ll \dots \ll \tau_{N_f}. \quad (3.18)$$

We thus obtain a set of mutually incoherent fields  $Y_1, Y_2, \dots, Y_{N_f}$ , that we can combine in the same single-mode fiber. The multiplexed signal will then be

$$Z(t) = \sum_{i=1}^{N_f} Y_i = \frac{1}{2} \sum_{i=1}^{N_f} [X_i(t + \tau_i) + X_i(t) e^{i\phi_{n,i}}], \quad (3.19)$$

where  $\phi_{n,i}$  is the phase encoded by the  $i$ -th modulator. After the transmission line, at the decoder, we split the received field and we feed another set of MZIs with delays matching the input ones. Considering the  $i$ -th modulator ( $\tau_i$  delay), the output signal is the results of the sum of many terms of the form of Eq. (3.16). Due to the condition in Eq. (3.18), all terms with non-matching delays are averaged to zero. Therefore, the measured signal is equal to

$$\overline{S_{n,i}} = \text{Re} \left[ \frac{\langle Z(t + \tau_i) Z^*(t) \rangle_T}{N_f} \right] = \text{Re} \left[ \frac{\langle |X_i(t + \tau_i)|^2 \rangle_T e^{i\phi_{n,i}}}{4N_f} \right] = \frac{P_{\text{in}}}{4N_f} \cos(\phi_{n,i}). \quad (3.20)$$

Therefore, by using a dual set of MZIs with matched delays, we are able to encode and decode information in the phase  $N_f$  input fields, transmitted through a single-mode fiber. The cost of multiplexing is twofold: the power reaching the detector is lower ( $1/N_f$ ) and, more importantly, all the incoherent fields will contribute to the detector noise [51–54]. This noise contribution is known as *optical beat noise*. We will extensively discuss this noise in the treatment of mutual coherence coding.

## 3.2 Figures of merit

To compare different communication systems, we need metrics that assess the performance of a specific scheme. We have selected three figures of merit that

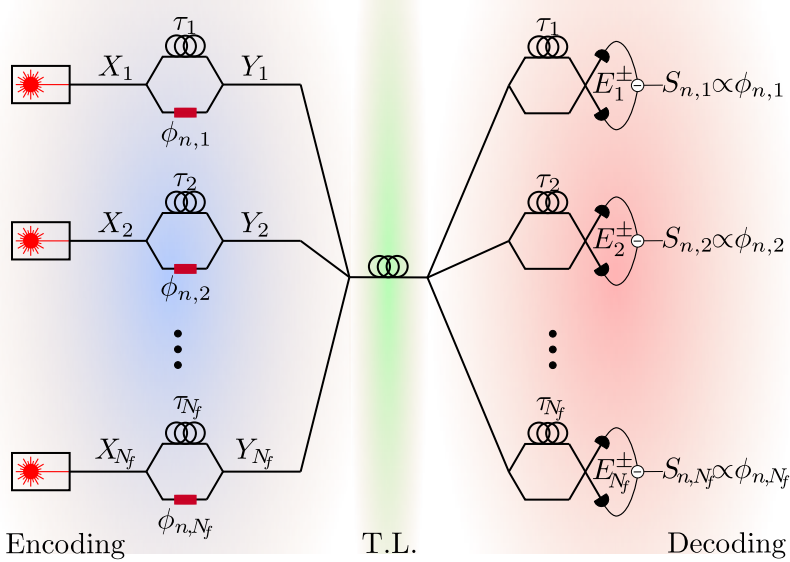


**Figure 3.4:** Coherence multiplexing in the case of  $N_f$  multiplexed fields. A set of MZIs splits each input field into a signal-reference pair of fields. The  $i$ -th reference field undergoes a delay  $\tau_i$ , while a phase modulator adds a phase  $\phi_{n,i}$  to the signal field. Then, all the modulated fields get mixed in the transmission line. At the receiver side, the transmitted field is again split to reach a set of MZIs, each with different delays matching the input ones, and the outputs are measured by balanced photodetectors. The signal measured by the  $i$ -th detector is given only by the signal-reference pair that matches the  $i$ -th delay.

we believe are the most relevant for a general comparison that does not consider a particular practical implementation: signal-to-noise ratio, maximum bit-rate, and spectral efficiency.

### 3.2.1 Signal-to-noise ratio

The signal-to-noise ratio (SNR) is a key parameter for evaluating communication systems. A higher SNR reduces the probability of bit error [58] and increases the channel capacity (see next subsection). As the name suggests, the SNR is defined as the ratio of the signal power and the noise power. Let us consider a received field  $\tilde{S}$  affected by noise. In the definition of the SNR, we denote by the term *signal* the expectation value of  $\tilde{S}$ . Regarding the noise, as discussed in Sec. 3.1.1, we consider it a zero-mean Gaussian process, meaning

that it is fully defined by the variance of  $\tilde{S}$ . Therefore, we derive the SNR as

$$\text{SNR} = \frac{(\overline{\tilde{S}})^2}{\text{Var}(\tilde{S})}. \quad (3.21)$$

### 3.2.2 Channel capacity and maximum bit-rate

The *channel capacity* was first defined by Shannon in his seminal paper “Communication in the presence of noise” [57]. In his article, beside the rigorous demonstration, he gives an estimation of the channel capacity that has a clear intuitive meaning. Here, we will revisit his reasoning to arrive at the formal definition.

As we have seen in Sec. 3.1.1, we receive a symbol per carrier per integration time of the detector  $T$ . Considering a symbol belonging to a  $M$ -ary alphabet, the number of bits per symbol are  $n_b = \log_2(M)$ . Thus, we can define the bit-rate as

$$\text{BR} = N_S \frac{\log_2(M)}{T}, \quad (3.22)$$

where  $N_S$  is the number of multiplexed carriers, i.e., symbols received per sampling period  $T$ . One might ask what is the maximum number  $M$  that we can have in the presence of noise. This is limited by the number of levels we can distinguish, in turn limited by the stochastic fluctuations of the perturbed signal. Let us consider a signal affected by noise  $\tilde{S}(t) = S(t) + N(t)$ , measured by a photodetector:

$$\mathcal{D}[\tilde{S}] = \langle |\tilde{S}(t)|^2 \rangle_T = \langle |S(t)|^2 \rangle_T + \langle |N(t)|^2 \rangle_T \pm 2\text{Re} \left( \langle S(t)N^*(t) \rangle_T \right). \quad (3.23)$$

Because the signal and the noise are uncorrelated, the expectation value of the detected signal is

$$\overline{\mathcal{D}[\tilde{S}]} = P_S + P_N, \quad (3.24)$$

where  $P_S = \overline{|S(t)|^2}$  and  $P_N = \overline{|N(t)|^2}$ . The variance is the sum of the variances of the different noise contributions. For a perfectly deterministic signal, the variance is

$$\text{Var}\{\mathcal{D}(\tilde{S})\} = P_N. \quad (3.25)$$

Considering the ideal scenario of perfect error correction, an estimate of the number of levels we can distinguish is given by the ratio between the



expectation value of the detected amplitude and the standard deviation of the measurement [57]:

$$M_{\max} = \sqrt{\frac{P_S + P_N}{P_N}} = \sqrt{1 + \text{SNR}}. \quad (3.26)$$

Finally, combining Eq. (3.22) and Eq. (3.26), the maximum bit-rate ideally achievable without errors is

$$\text{BR}_{\max} = N_S \frac{\log_2(M_{\max})}{T} = N_S \frac{\log_2(1 + \text{SNR})}{2T} = N_S C_{Sh}. \quad (3.27)$$

The parameter  $C_{Sh}$  is known as channel capacity (or Shannon capacity), and it is the result of the Shannon-Hartley theorem [57]. We decided to use  $\text{BR}_{\max}$  as a figure of merit to provide a theoretical limit on the bit-rate of mutual coherence coding, without being constrained by the number of levels that a specific implementation can practically encode, or by the probability of bit error that a particular application can accept [58].

*The maximum channel capacity achievable in current communication systems is 100 Tbit/s, due to nonlinearities of the fiber response [5].*

#### 3.2.3 Spectral efficiency

The third figure of merit we selected is the spectral efficiency (SE). It quantifies how effectively a given communication system exploits the signal bandwidth. We define it as maximum bit-rate per symbol per unit bandwidth (bit/s/Hz)<sup>†</sup>, i.e.,

$$\text{SE} = \frac{\text{BR}_{\max}}{N_S \text{BW}_{\text{in}}}, \quad (3.28)$$

where  $\text{BW}_{\text{in}}$  is the bandwidth of the transmitted signal.

*The spectral efficiency of current communication systems can reach 5 bit/s/Hz and above, employing advanced multilevel modulation techniques [10].*

### 3.3 Mutual coherence coding

In this final section, we apply the theory presented above to the analysis of mutual coherence coding. We start by describing the encoding and decoding

---

<sup>†</sup>Note that other works [61, 65] define the spectral efficiency considering the totality of the multiplexed signals, i.e.,  $\text{SE} = \text{BR}_{\max}/\text{BW}_{\text{in}}$ , reaching values of SE on the order of 100 bit/s/Hz. We find our normalized definition more appropriate for fair comparisons.

schemes, followed by the dependence of the figures of merit on the number of transmitted beams. We conclude by evaluating the advantages of using the proposed technique in combination with coherence multiplexing and proposing the generalization of coherence control to other degrees of freedom.

### 3.3.1 Implementation

A general implementation of mutual coherence coding is sketched in Fig. 3.5, for the case of  $N_f = 4$ . We omit the bit map and inverse bit map, which are not peculiar in mutual coherence coding and can be freely chosen depending on the particular application. We start from a set of incoherent input fields  $X_1, X_2, \dots, X_{N_f}$ , with the same central frequency  $\nu_0$ , linewidth  $\Delta\nu$  and power  $P_{\text{in}}$ . The light sources employed can be LEDs or laser diodes, characterized by a large linewidth, but that can still be considered narrow-band, i.e.,  $\Delta\nu \ll \nu_0$ . Through a linear port, each input  $X_j$  is connected to an output field  $Y_i$ , with  $i \in \{1, 2, \dots, N_f\}$ , through a complex coefficient  $t_{ij}$ , i.e.,  $Y_i = \sum_{j=1}^{N_f} t_{ij} X_j$ . The mutual coherence  $\gamma_{ij}$  between two output fields  $Y_i$  and  $Y_j$  takes the form

$$\gamma_{ij} = \frac{\overline{Y_i Y_j^*}}{P_{\text{out}}} = \sum_{n=1}^{N_f} t_{in} \sum_{m=1}^{N_f} t_{jm}^* \frac{\overline{X_n X_m^*}}{P_{\text{out}}} = \frac{P_{\text{in}}}{P_{\text{out}}} \sum_{n=1}^{N_f} t_{in} t_{jn}^*, \quad (3.29)$$

where we used the condition of input mutual incoherence  $\overline{X_i X_j^*} = P_{\text{in}} \delta_{ij}$ , and we assumed the output fields having the same power  $\overline{|Y_i|^2} = P_{\text{out}} = \eta P_{\text{in}}$ ,

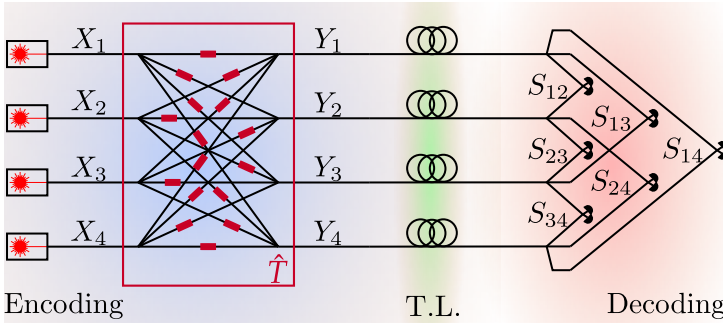


**Figure 3.5:** Implementation of mutual coherence coding. A set of broadband light sources (here: 4) are fed into a linear port  $\hat{T}$  to control their mutual coherences. Afterward, the fields reach the receiver through a transmission line. The received fields are then split to recover the encoded signals. The mutual coherence is reconstructed through pair-wise interference experiments, which can be implemented using a beam splitter and a balanced detector.

where  $\eta = P_{\text{out}}/P_{\text{in}}$  is the transmission efficiency. By tuning the values of the modulation coefficients  $t_{ij}$ , we can then control the values of  $\gamma_{ij}$  (see Sec. 2.2). We note that the coherence matrix  $\mathbb{K}$ , which collects the degrees of coherence of all the pairs, must be positive semi-definite, which is always fulfilled if  $|\gamma_{ij}| \leq 1/(N_f - 1)$ , for all  $i \neq j$  (see Sec. 2.1.3). This choice, while allowing us to independently choose the values of all the mutual coherences, restricts the analysis to a subspace of possible coherence matrices. One could envision a more general scenario where the value of  $\gamma_{ij}$  can exceed the mentioned bound [e.g., using the less stringent condition given by Eq. (2.32)]. In this way, it would be possible to find other values of mutual coherence which, for instance, maximize the SNR. The output fields  $Y_i$  are transmitted to the receiver through a transmission line. The transmission line in the case of signals carried by spatially separated light beams can be a bundle of single-mode fibers, or a multi-core fiber, making use of the platform developed for space division multiplexing (see Ch. 1 and Ref. [66]). At the receiver side, we reconstruct the values of mutual coherences to decode the transmitted data. We divide each received light beam into  $N_f - 1$  copies, and subsequently perform  $N_f(N_f - 1)/2$  pair-wise interference experiments. The interference experiment is carried out by mixing two fields via a beam splitter, and measuring the intensities of the two output ports with a differential detector (see Sec. 2.1.2). The two fields  $E_{ij}^+$  and  $E_{ij}^-$  at the output ports are

$$E_{ij}^{\pm} = \frac{Y_i \pm Y_j}{\sqrt{2(N_f - 1)}}, \quad (3.30)$$

while the signal measured by the balanced detector is

$$S_{ij} = \langle |E_{ij}^+|^2 \rangle - \langle |E_{ij}^-|^2 \rangle = \frac{2 \operatorname{Re}(\langle Y_i Y_j^* \rangle_T)}{N_f - 1}. \quad (3.31)$$

The detected signal is a random process, which we can characterize by an mean value and a variance. From the expectation value, we confirm that the designed measurement corresponds indeed to an unbiased estimate of the real value of the mutual coherence

$$\overline{S_{ij}} = \frac{2}{T(N_f - 1)} \int_{-T/2}^{T/2} \operatorname{Re}(\overline{Y_i Y_j^*}) dt = \frac{2P_{\text{out}}}{N_f - 1} \operatorname{Re}(\gamma_{ij}), \quad (3.32)$$

where we used Eq. (3.29) for the definition of  $\gamma_{ij}$ . However, the stochastic nature of the underlying fields leads to a non-zero variance even in the case

where no noise is considered (for the derivation, see App. B.2)

$$\text{Var}(S_{ij}) = \overline{S_{ij}^2} - (\overline{S_{ij}})^2 = \frac{2P_{\text{out}}^2 \left[ 1 + \text{Re}(\gamma_{ij}^2) \right]}{(N_f - 1)^2 2\pi\Delta\nu T}. \quad (3.33)$$

This variance is inversely proportional to the number of statistically independent realizations that we sample during the measurement time  $T$ . Fields separated by a time longer than the inverse of the linewidth are uncorrelated, hence the number of independent realizations of the random process is given by  $2\pi\Delta\nu T$  [38]. Moreover, in the limit of small mutual coherence  $|\gamma_{ij}| \ll 1$ , the variance saturates to a non-zero value determined by the number of collected samples. The variance in Eq. (3.33) gives a contribution to the total noise, which is known in the literature as optical beat noise, and it is regarded as the main limitation for the performance of traditional coherence multiplexing (see Sec. 3.1.3 and Refs. [51–54, 67]).

### 3.3.2 Performance

We will now derive, for the case of mutual coherence coding, the figures of merit discussed in Sec. 3.2. We focus on the maximum bit-rate allowed by the channel capacity in the presence of additive white Gaussian noise [57] (note that also the optical beat noise falls into this category [67]). Each of the  $N_p$  mutual coherences between the field pairs is an independent signal, leading to a maximum bit-rate

$$\text{BR}_{\text{max}} = N_p \frac{\log_2(1 + \text{SNR})}{2T} = \frac{N_f(N_f - 1)}{2} \frac{\log_2(1 + \text{SNR})}{2T}. \quad (3.34)$$

According to Eq. (3.21), the SNR is defined as

$$\text{SNR} = \frac{(\overline{\tilde{S}_{ij}})^2}{\text{Var}(\tilde{S}_{ij})}, \quad (3.35)$$

where  $\tilde{S}_{ij}$  is the detected signal resulting from the mutual coherence of the pair of fields  $Y_i$  and  $Y_j$  in the presence of noise. For multiple, independent noise sources the variance is the sum of the variances of the different noise contributions (see App. B.3). Restricting ourselves to optical beat noise and shot noise, the SNR can be expressed as

$$\text{SNR} = \left[ \frac{1 + \text{Re}(\gamma_{ij}^2)}{2\text{Re}(\gamma_{ij})^2 2\pi\Delta\nu T} + \frac{h\nu_0}{\eta P_{\text{in}} \text{Re}(\gamma_{ij})^2 2\pi T} \right]^{-1}. \quad (3.36)$$

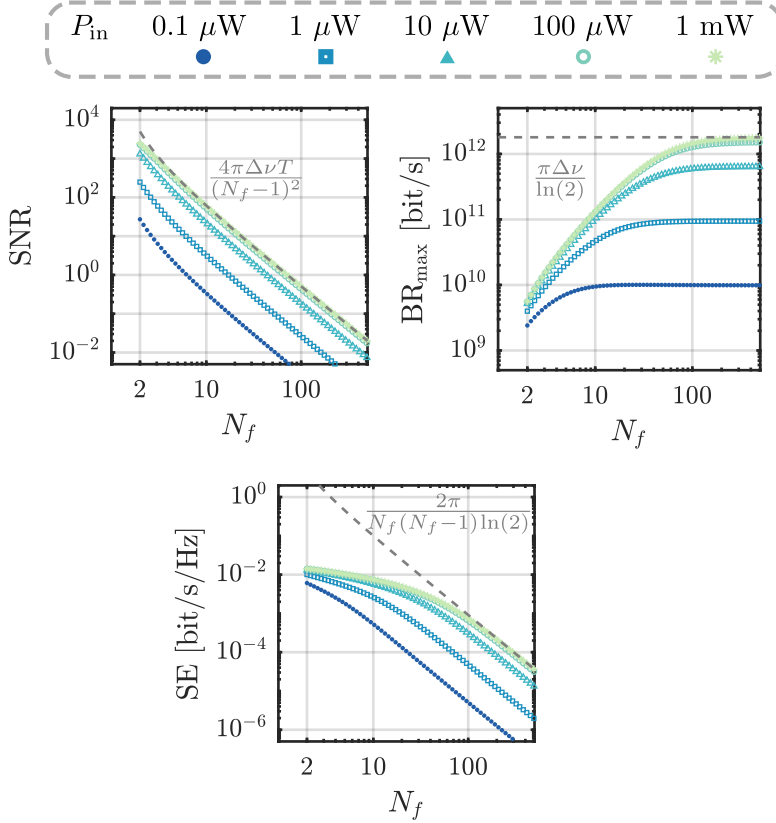


**Figure 3.6:** System performance. (a) SNR, (b) maximum bit-rate ( $\text{BR}_{\text{max}}$ ) and (c) spectral efficiency (SE) as a function of the number of transmitted fields ( $N_f$ ) and input power ( $P_{\text{in}}$ ). The dashed lines correspond to (a) Eq. 3.37, (b) Eq. 3.38 and (c) Eq. 3.39. The system parameters are:  $T = 1$  ns,  $\gamma_{\text{max}} = 1/(N_f - 1)$ ,  $\lambda_0 = 870$  nm,  $\Delta\lambda = 1$  nm and  $\eta = 1\%$ , where  $\lambda_0 = c/v_0$  and  $\Delta\lambda = c\Delta\nu/v_0^2$  are the central wavelength and the linewidth expressed in nanometer, respectively, while  $c$  is the speed of light.

The first term is the optical beat noise highlighted in (3.33) and the second term corresponds to shot noise. The derivation of Eq. (3.34) assumes a value of  $\text{Re}(\gamma_{ij}) = \gamma_{\max}$  that is at the extreme of the allowed range of values. In fact, with this choice the SNR provides the maximum number of discretization steps of the signal. We choose  $\gamma_{\max} = 1/(N_f - 1)$  to ensure the positive semi-definiteness of the output coherence matrix. We then insert  $\gamma_{\max}$  into Eq. (3.36) for the SNR and then into Eq. (3.34) to obtain the maximum bit-rate. In Figs. 3.6a and 3.6b, we show the SNR and the  $\text{BR}_{\max}$ , respectively, as a function of the number of transmitted fields  $N_f$  for different input powers. The SNR decays monotonically with increasing  $N_f$ , whereas the maximum bit-rate first increases quadratically and then saturates at large  $N_f$  values. The quadratic increase derives from the number of field pairs, while the saturation is due to the low SNR. In the limit of large  $N_f$  and sufficient input power (to be limited by optical beat noise) the SNR takes the expression

$$\text{SNR} \approx \frac{4\pi\Delta\nu T}{(N_f - 1)^2}, \quad (3.37)$$

where the factor  $2\pi\Delta\nu T$  can be understood as the number of independent realizations of the light field within the time  $T$ . This expression is in line with what has been previously reported for traditional coherence multiplexing limited by optical beat noise [67]. When the SNR becomes smaller than 1, we can Taylor expand Eq. (3.34) and the maximum bit-rate saturates at the value

$$\text{BR}_{\max} \approx \frac{N_f(N_f - 1)}{4T} \left[ \frac{4\pi\Delta\nu T}{(N_f - 1)^2 \ln(2)} \right] \approx \frac{\pi\Delta\nu}{\ln(2)}. \quad (3.38)$$

Therefore, the ultimate limit of the bit-rate is given by the input linewidth. The saturation can be well understood considering the statistical nature of mutual coherence, since the rate of field realizations needed to reconstruct the mutual coherence is given by the linewidth.

Finally, we derive the expression of the spectral efficiency, which reads as

$$\text{SE} = \frac{\text{BR}_{\max}}{N_p \Delta\nu} < \frac{\pi}{N_p \ln(2)} = \frac{2\pi}{N_f(N_f - 1) \ln(2)}. \quad (3.39)$$

The dependence of the SE on the number of transmitted fields  $N_f$  is represented in Fig. 3.6c. With a value much smaller than one, mutual coherence coding performs worse in terms of spectral efficiency than standard coding techniques [68]. On the other hand, the bandwidth  $\Delta\nu$  of mutual coherence coding is considerably larger than the bandwidth of other coding techniques,

which are restricted by the bandwidth of optoelectronic components, such as detectors and modulators ( $\sim 50$  GHz). The large bandwidth associated with mutual coherence coding is provided by the input sources, and it is used to build the statistical ensemble required to achieve a quadratic scaling of the number of transmitted signals on  $N_f$ . Thanks to this quadratic scaling, mutual coherence coding can achieve bit-rates on the order of  $\Delta\nu$ , hence very high for input with large linewidth. Therefore, even if the spectral efficiency of mutual coherence coding is much lower than in other coding schemes, we can gain technical advantage in terms of bit-rate.

#### 3.3.3 Discussion

Mutual coherence coding comes with a quadratic scaling of the bit-rate with the number of transmitted fields, up to the point where it saturates. The saturation value is given by the linewidth of the light sources employed. Selecting broadband light sources, such as LEDs or laser diodes, can therefore lead to remarkable data transmission rates. These light sources have the added advantage of being inexpensive, thus facilitating the scalability. Furthermore, the use of broadband light makes our proposal suitable for free-space communications, where partially coherent sources have been reported to be more robust to atmospheric turbulence [21]. Another advantage of the proposed method is the absence of local oscillators at the receiver side, since in mutual coherence coding the transmitted beams are mutually referenced, allowing for a simpler implementation. However, the discussed implementation requires an accurate control on the length difference between the transmitted fibers. In fact, through the linear port we can control the *equal-time* mutual coherence, which is conserved only as long as the optical path difference of the interfering beams does not exceed the coherence length of the input source. This issue becomes more severe for large input linewidths, as the coherence length is reduced accordingly. A possible solution to this limitation is to combine mutual coherence coding and coherence multiplexing, obtaining a fully coherence-based communication system. A schematics of this solution is depicted in Fig. 3.7. To do so, one would introduce, at the sender side, a different delay for each output beam of the linear port. If the individual delays and their differences are much longer than the coherence time of the light sources, the fields do not interfere, even when combined in the same single-mode fiber. The receiver then splits the transmitted field and compensates for the input delays to reconstruct the multiplexed signals, before proceeding with the pair-wise interference experiments. Besides allowing to perform the transmission with

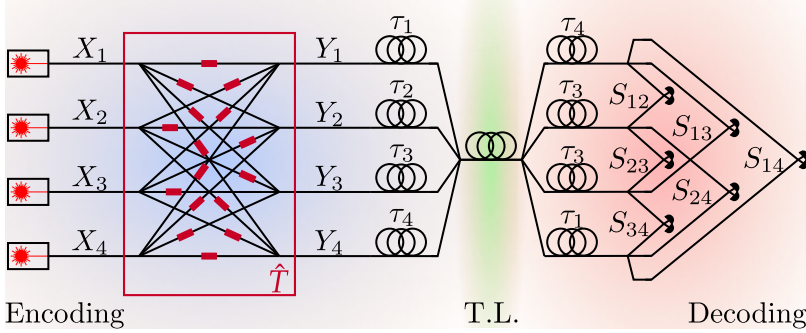


**Figure 3.7:** Combination of mutual coherence coding and coherence multiplexing. We control the coherence matrix of a set of mutually incoherent fields through a linear port  $\hat{T}$ . Each of the generated fields  $Y_i$  undergoes a delay  $\tau_i$ , where  $\tau_1 \ll \tau_2 \ll \tau_3 \ll \tau_4$ . The signals are then mixed in the same fiber which transmits the fields to the receiver. At the receiver side, a set of delays matches the input one. Analogously to coherence multiplexing, the encoded coherence matrix is retrieved only for the field components that undergo the same total delay.

a single fiber, this approach relaxes the requirement on the length difference between the fibers. In fact, since the transmission line is common, any optical path difference between the interfering beams can only originate from the introduced delays. Interestingly, in this approach the delay lines are very short (on the order of the coherence length) and embedded in a well controlled environment. The needed calibration of the delay length can then make use of the techniques developed for standard coherent detection schemes [69].

Moreover, having a coherence based communication system comes with security benefits. Suppose the sender and the receiver have a pre-shared set of delays (which can be frequently updated). An eavesdropper cannot record the message encoded in the mutual coherence, because they are not able to record the fluctuations of the light field in real time. An eavesdropper could measure the mutual coherences only through interference experiments and only if they knew the pre-shared delays. This security benefit is similar to that of traditional coherence multiplexing [70].

As a concluding remark, we highlight that mutual coherence coding is not limited to spatial coherence. Coherence based on any other degree of freedom of light (temporal coherence, degree of polarization, correlations between transverse modes, etc.) can be used to encode information, allowing for various implementations. Moreover, resorting to mutual coherence between different degrees of freedom [71] can lead to a great enhancement of the scaling with



### 3 Encoding information in the mutual coherence

---

the number of transmitted fields. Considering for example  $n$  different beams (spatial degree of freedom), each of them characterized by  $m$  transverse modes, the number of mutual coherences that we can control is  $N_p \approx (n \times m)^2/2$ . This can be further generalized (e.g., including time and polarization) to greatly improve the capacity of current communication systems.

# 4

---

## Coherence control with an optical complex medium

The use of mutual coherence to encode information has the potential to increase the capacity of optical communication systems. If, with a standard scheme, we are able to multiplex  $N_f$  fields, the pair-wise nature of mutual coherence allows to simultaneously send  $\approx N_f^2/2$  independent signals. Obviously, being able to control the mutual coherence of several, spatially separated beams is crucial for the implementation of the communication scheme.

Efforts have been made in developing several methods to control mutual coherence, either via active devices such as spinning phase diffusers [72], spatial light modulators (SLMs) [73] and digital micromirror devices (DMDs) [74], or via passive methods such as fine tuning of the optical path [75–77]. Yet, all these techniques have limitations on the attainable speed or are limited to a single pair of fields.

In Sec. 2.2, we have presented a method to control the coherence matrix of a set of fields, based on a linear transformation. In optical communications, a linear transformation must be implemented through a *multi-port linear optical device* (or *linear port*). There are several ways to implement an optical

---

This chapter is based on the article: Alfonso Nardi, Felix Tebbenjohanns, Massimiliano Rossi, Shawn Divitt, Andreas Norrman, Sylvain Gigan, Martin Frimmer, and Lukas Novotny, *Controlling spatial coherence with an optical complex medium*, Opt. Express 29, 40831-40840 (2021)

linear port. The earliest proposed method considered a free-space optical setup, employing phase shifters and beam splitters with variable transmittance [78]. However, as the number of ports increases, the use of discrete optical components in free space rapidly becomes impractical. Thus, a straightforward solution is to employ integrated optics [79–81]. Nonetheless, the number of components still scales quadratically with the dimensionality of the linear transformation. This is a major challenge when working with photonic integrated circuits, as any manufacturing variability results in an error in the linear transformation produced. Furthermore, non-unitary transformations are needed to control the coherence matrix (see App. B.1). While there exist configurations that allow the implementation of non-unitary linear ports [82], they involve the use of a complex network of interferometers, where a large part of the components is used to introduce controlled losses [83]. An interesting alternative emerged recently, that exploits the properties of optical complex media when combined with wavefront shaping devices. A complex medium is an optical system that mixes many degrees of freedom of an impinging field (space, time, polarization, mode), resulting in a scrambled intensity distribution at its output [84]. The extremely large number of internal degrees of freedom of a complex medium makes the output intensity pattern disordered, yet it remains deterministic. Therefore, it is possible to fully characterize the effect of the propagation through the medium on an incident field with a linear transmission matrix (TM) [85]. Knowledge of the TM allows complex media to be used to perform a variety of tasks, once combined with programmable modulators. Applications include the control of different properties of light, e.g., intensity [86–88], polarization [89, 90] and spectrum [91–94]. In particular, complex media have been proposed as a compact, highly-dimensional multi-port device [95], e.g., to perform quantum operations [96, 97]. Interestingly, even though both random diffusers and wavefront shaping devices, such as SLMs and DMDs, have been used for the control of the spatial coherence [72–74], they have not been employed in combination to overcome the previous limitations.

In this chapter, we show the control of the coherence matrix of a set of fields in a single-shot fashion, based on a linear transformation applied to  $n$  mutually incoherent input beams. The linear transformation is experimentally implemented with a complex medium in combination with SLM-based wavefront shaping. As a proof of principle, we report the realization of a  $3 \times 3$ -port device and show that it generates any combination of mutual coherences, within the technical limitations.

## 4.1 Wavefront shaping in multi-scattering media

Consider a room well lit by a lamp, enclosed between white walls, with a rose in its center. A door, opened, leads to an adjoining room, also surrounded by white walls. We sit comfortably in the center of the room, and we would like to observe the rose. Since the walls of the entire structure are perfectly white, there is no light absorption. So we would expect the light reflected by the flower (hence containing the information of its shape) to propagate to the second room, allowing us to see an image of the rose (see Fig. 4.1). Why does this not happen? The physical phenomenon that prevents us from seeing around corners (as well as through thick fog or clouds) is called multiple scattering. To understand this phenomenon, we need to investigate what happens at the microscopic level when the light is reflected from the wall (Fig. 4.2).

Let us consider a wall composed of numerous non-absorbing particles, each of them scattering light in a random direction. The cumulative effect of all the scattering events happening in the material (multiple scattering) is the scrambling of the outgoing light. This hides the spatial information contained in the light reflected by the rose, making it impossible for the naked eye to

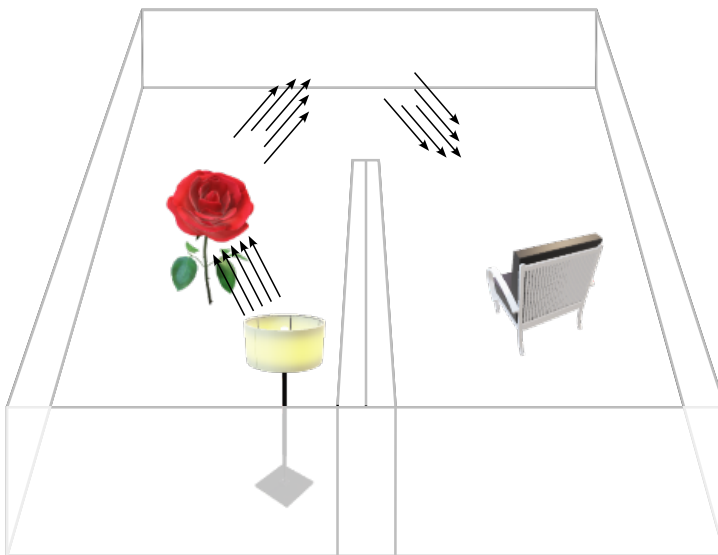


**Figure 4.1:** Light propagation inside a completely white room. One would expect that the light reflected by the rose (which then contains the information of its shape) is in turn reflected by the non-absorbing walls until they reach the observer sit in the adjacent room.

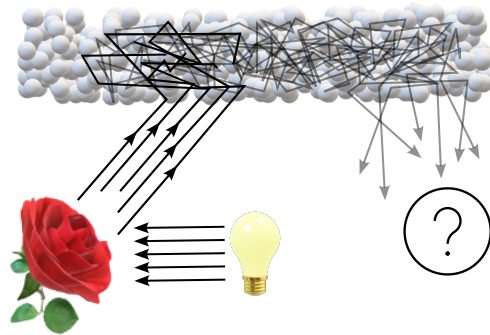


**Figure 4.2:** Multi-scattering in the white paint. The white paint covering the wall consists of many scattering particles. The light reflected by the rose is scattered many times inside the material before reaching the observer in the other room. This multiple-scattering scrambles the wavefront, hiding the shape information.

reconstruct its shape. We refer to this class of multi-scattering, non-absorbing materials as *random* or *complex* media (or, simply, as multi-scattering media).

Let us now assume that we have perfect knowledge of the effect of the material on each incoming ray of light, and that we are equipped with a device that can modify the incident beam at will. Then we would be able to pre-compensate the beam impinging the wall, so to cancel its effect and retrieve the spatial information that leads to the rose image (Fig. 4.3).

This simplified picture is intended to provide the reader with an intuitive view of the basic principle of light propagation control in complex media. Starting from this principle, this scientific field has progressed to develop numerous methods for turning a random medium into a useful instrument, such as a high-NA lens [87], a variable phase plate [98, 99], a spectral filter [100, 101], a high resolution spectrometer [102, 103], an optical simulator [104], or a broadband second harmonic generator [105]. In particular, wavefront shaping can be used in combination with a multi-scattering medium to construct an arbitrary, programmable optical linear port. The rest of the chapter will be devoted to the detailed description of how to realize such a device.

### 4.1.1 Transmission matrix

We have seen that a multi-scattering medium has the property of mixing the input modes, to the extent that it generates a disordered intensity pattern at the output, resulting from the complex interference of the propagating modes [84].

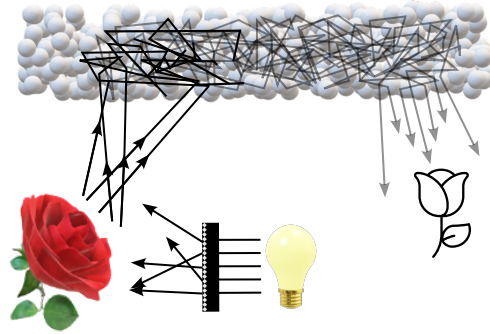


**Figure 4.3:** Retrieving the image of the rose after the propagation inside the white paint. The effect of the paint is seemingly random, yet it is deterministic. Thus, knowing the effect of the wall to the input light, we can think of using a device to pre-compensate for the multi-scattering phenomenon, such that we are able to reconstruct the image of the rose after the propagation inside the white medium.

An example of this random intensity distribution, known as *speckle pattern*, is reported in Fig. 4.4. Different input modes produce different, seemingly random, speckle patterns. However, as long as the input light and the position of the scatterers in the material do not change in time, a given input mode always leads to the same result. To use the complex medium as an optical tool, we ideally want to fully characterize and control this input-output relation. Since we are dealing with a linear medium, this relation can be expressed in terms of the scattering matrix [106]. Let us refer to the scheme depicted in Fig. 4.5. We consider a set of input modes, which we collect in a vector  $\mathbf{E}_{\text{in}}$ ,

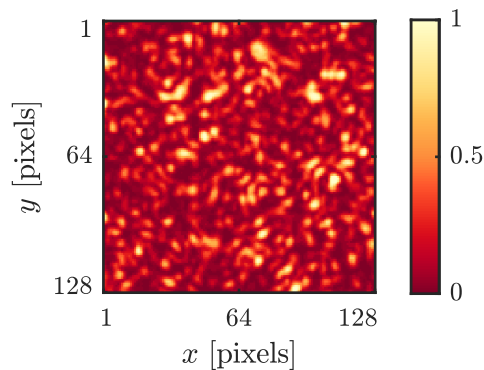


**Figure 4.4:** Camera image of a typical speckle pattern.

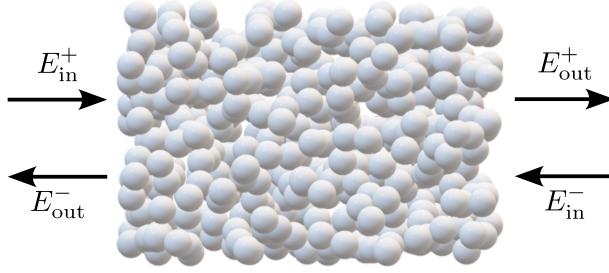


**Figure 4.5:** Scattering matrix formalism. The scattering matrix relates the input fields and the output fields scattered by the material.  $E_{\text{in}}^+$  and  $E_{\text{out}}^+$  are the input and output right-propagating beams, respectively, while  $E_{\text{in}}^-$  and  $E_{\text{out}}^-$  are the input and output left-propagating beams.

such as

$$\mathbf{E}_{\text{in}} = \begin{bmatrix} E_{\text{in}}^+ \\ E_{\text{in}}^- \end{bmatrix}, \quad (4.1)$$

where  $\mathbf{E}_{\text{in}}^+$  and  $\mathbf{E}_{\text{in}}^-$  are the column vectors collecting the right-propagating and the left-propagating modes, respectively. The scattering matrix  $\mathbb{S}$  relates the input vector to a set of output modes  $\mathbf{E}_{\text{out}} = [E_{\text{out}}^+, E_{\text{out}}^-]^\top$ , according to the relation

$$\mathbf{E}_{\text{out}} = \mathbb{S}\mathbf{E}_{\text{in}} \quad \longrightarrow \quad \begin{bmatrix} E_{\text{out}}^+ \\ E_{\text{out}}^- \end{bmatrix} = \begin{bmatrix} \mathbb{T} & \mathbb{R}' \\ \mathbb{R} & \mathbb{T}' \end{bmatrix} \begin{bmatrix} E_{\text{in}}^+ \\ E_{\text{in}}^- \end{bmatrix}, \quad (4.2)$$

where again  $\mathbf{E}_{\text{out}}^+$  and  $\mathbf{E}_{\text{out}}^-$  are the right-propagating and the left-propagating output modes, respectively. Matrices  $\mathbb{R}$  and  $\mathbb{R}'$  are known as *reflection* matrices, while  $\mathbb{T}$  and  $\mathbb{T}'$  are the *transmission* matrices. The scattering matrix  $\mathbb{S}$  is unitary in absence of loss ( $\mathbb{S}\mathbb{S}^\dagger = \mathbb{I}$ , where  $\mathbb{I}$  is the identity matrix). Experimentally, measuring the entire scattering matrix of a 3D multiple scattering medium is a goal that remains unattained to date, despite considerable efforts [107]. Still, even with only partial knowledge of the scattering matrix, we can access enough information to have some control over the output speckle pattern. In particular, we focus on a sub-matrix of  $\mathbb{S}$  that connects the right-propagating input and output modes. This is commonly known as the *transmission matrix* (TM) of the medium, a concept that was first presented and measured by Popoff *et al.* [85]. Due to the loss of information, the TM is a random matrix, and contains only a subset of the total modes [108]. All the uncontrolled modes count as lossy channels, thus allowing the TM to be non-unitary. Nonetheless, for our purposes, the dimensionality of the TM is very large, being limited only by the number of pixels of the devices we use to characterize it [106]. In this

work, we use a phase-only, liquid crystal-based SLM and a camera, both with a number of pixels typically on the order of one million. From the knowledge of this large fixed random matrix, we can employ the SLM in combination with the complex medium to implement a smaller but reconfigurable linear transformation [95], as we will see in the following sections.

### 4.1.2 Characterization of the transmission matrix

Let us proceed describing how to characterize the TM of a random medium. The principle is the following. We consider a set of  $N$  input  $E_n^{\text{in}}$  (with  $n \in \{1, 2, \dots, N\}$ ) and  $M$  output  $E_m^{\text{out}}$  (with  $m \in \{1, 2, \dots, M\}$ ) orthogonal modes. The transmission matrix relates each input and output field, i.e.,  $E_m^{\text{out}} = t_{mn} E_n^{\text{in}}$ , where  $t_{mn}$  is a complex element of the TM. To characterize the TM, we measure for each input mode the resulting complex amplitudes of the output modes. The measured amplitudes are the elements of the corresponding column of the TM (injecting the  $n$ -th input mode results in the measurement of the  $n$ -th column). Implementing sequentially all the modes of the input basis, one reconstructs the entire TM.

Let us now discuss how this method can be implemented with the SLM, the complex medium and the camera (see Fig. 4.6). An input field, characterized by constant amplitude and phase, is modulated by  $N$  segments (i.e., group of pixels of suitable size, see an example in Fig. 4.6) of the SLM, that we can consider orthogonal spatial modes. At the output of the multi-scattering medium, we record with a camera the speckle field resulting from the propagation. Through appropriate magnification and binning, we ensure that the pixel size of the camera corresponds to the speckle grain [85], thus we can consider the field at each camera pixel as an independent output mode. Let us assume for now that we are able to measure the complex field  $E_m^{\text{out}}$  at the  $m$ -th camera pixel (we will describe how to extract the phase information later in the section). Each complex element  $t_{mn}$  of the TM relates the field at the  $n$ -th segment of the SLM ( $E_n^{\text{in}}$ ) with the field at the  $m$ -th camera pixel, i.e.,  $E_m^{\text{out}} = t_{mn} E_n^{\text{in}}$  (see Fig. 4.6). Therefore, the most straightforward way to measure the TM would be to switch off all the SLM segments except a single one, while recording the  $M$  output speckles. This would give access to the elements of the  $n$ -th column of the TM. Proceeding sequentially with all the other SLM segments, we will be able to reconstruct the entire TM. However, this basis, which is commonly regarded as *canonical* basis [85], has two main disadvantages:

- this basis is very sensitive to noise, since each vector of the basis consists of a single SLM segment;



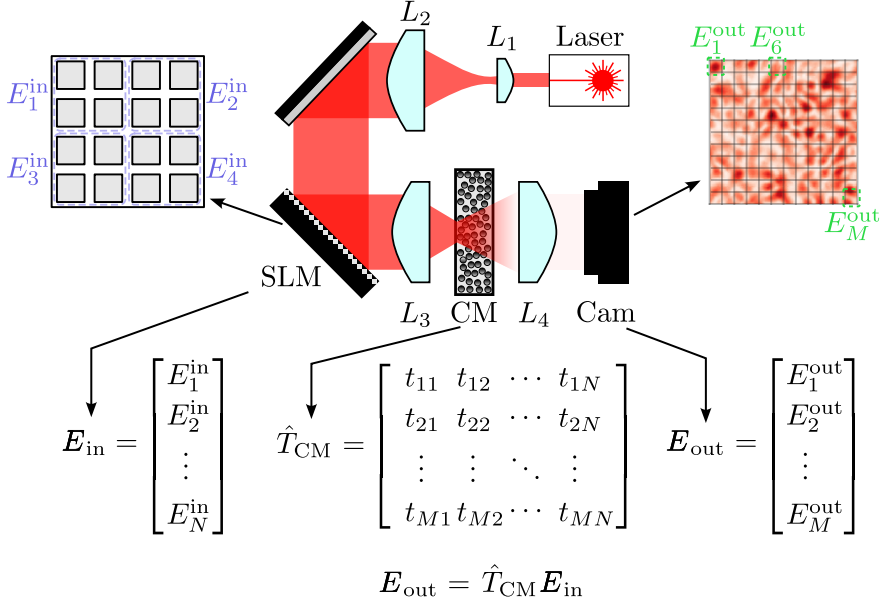


**Figure 4.6:** Experimental setup for characterizing the TM. A laser beam is expanded via a telescope ( $L_1$  and  $L_2$  lenses) to match the SLM aperture. We collect the SLM pixels into segments (in the examples each segments contains  $2 \times 2$  pixels), and we consider each segment as an independent input beam  $E_i^{\text{in}}$ , with  $i = 1, 2, \dots, N$ , where  $N$  is the total number of segments. The modulated field is focused by a lens ( $L_3$ ) onto a multi-scattering medium (CM), and the output light is then collimated by another lens ( $L_4$ ). Finally, a camera measures the resulting speckle intensity. Through appropriate magnification and binning, we make sure that the pixel size of the camera corresponds to the speckle grain. Each pixel is then considered as an independent output field  $E_i^{\text{out}}$ , with  $i = 1, 2, \dots, M$ , where  $M$  is the total number of camera pixels. The relationship between the input fields (collected in a column vector  $\mathbf{E}_{\text{in}}$ ) and the output fields (column vector  $\mathbf{E}_{\text{out}}$ ) is determined by the transmission matrix  $\hat{T}_{\text{CM}}$ .

- we would need to impose zero-intensity on all but one segment, which is not easily achieved with phase-only SLMs.

Therefore, we can consider another approach, which is offered by the Hadamard basis [85]. It consists of  $N$  orthogonal patterns (where  $N$  is also the number of individually controlled SLM segments), wherein half of the pixels have a  $\pi$  phase difference relative to the other half, while the amplitude is constant everywhere. It offers the advantage of being composed by phase-only patterns (easy to implement with the SLM), and it maximizes the intensity at the

output camera (all the SLM pixels contributes to the signal), decreasing the experimental sensibility to noise [109]. Let us give an example considering an SLM with  $N_{SLM} = 2 \times 2$  segments. We choose a vector of the canonical basis, e.g.,  $\mathbf{c} = [0, 1, 0, 0]^T$ . We can convert the vector  $\mathbf{c}$  in a vector  $\mathbf{h}$  of the Hadamard basis via the product with a  $4 \times 4$  *Hadamard matrix*  $\mathbb{H}_4$  [110]:

$$\underbrace{\begin{bmatrix} 1 \\ 1 \\ -1 \\ -1 \end{bmatrix}}_{\mathbf{h}} = \underbrace{\begin{bmatrix} 1 & 1 & 1 & 1 \\ 1 & 1 & -1 & -1 \\ 1 & -1 & 1 & -1 \\ 1 & -1 & -1 & 1 \end{bmatrix}}_{\mathbb{H}_4} \underbrace{\begin{bmatrix} 0 \\ 1 \\ 0 \\ 0 \end{bmatrix}}_{\mathbf{c}}. \quad (4.3)$$

We then reshape the vector  $\mathbf{h}$  into a  $2 \times 2$  matrix and program the SLM with the corresponding phase mask, that we use to measure the TM. In Fig. 4.7, we show some exemplary patterns for the case of  $N_{SLM} = 16 \times 16 = 256$  segments. Note that we use the Hadamard basis only to reconstruct the TM. After characterizing the TM in the Hadamard basis, we convert the measured TM in the canonical basis by a product with the Hadamard matrix [110].

After choosing the appropriate basis, it remains only to outline a method for measuring the output field. In fact, cameras are only able to measure the field intensity, losing the phase information. To measure phase, we must resort to an interferometric measurement. Typical interferometric measurements require the use of an external reference field, usually in the form of a broad, collimated Gaussian beam that approximates a plane wave. However, these techniques, while possible to implement [111], suffer from stability issues. Another approach is to use an internal reference [85]. This method relies on dividing the SLM into two parts:

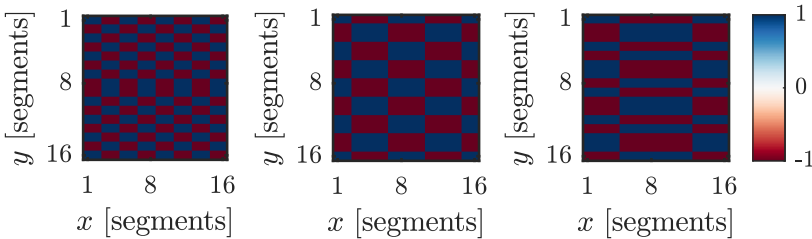


**Figure 4.7:** Examples of vectors of the Hadamard basis implemented with the SLM. We consider a SLM with  $16 \times 16 = 256$  segments. The initial column vectors are reshaped in order to be encoded into the SLM. Note that the vectors can only take values  $\{1, -1\}$ , which correspond to  $\{0, \pi\}$  phase, easily implementable with the SLM.

- one part of the SLM is used to implement the  $N$  phase-masks that constitute the Hadamard basis. Each input  $E_n^{\text{in}}$  generates an output speckle field, and we indicate the output field at the  $m$ -th camera pixel as  $E_{mn} = |E_{mn}|e^{i\phi_{mn}}$ ;
- the second part provides a reference field. It also generates a speckle pattern, which remains the same for any input vector. We denote as  $E_m^{\text{ref}} = |E_m^{\text{ref}}|e^{i\phi_m^{\text{ref}}}$  the output reference field at the  $m$ -th camera pixel (note that it does not depend on the particular input vector  $n$ , but it stays the same during the whole process of TM reconstruction).

We highlight this division in Fig. 4.8 using two different colors. At the SLM plane the two beams (which we can call *reference* and *Hadamard* beams) are spatially separated, but they get mixed during the propagation through the complex medium. Thus, the resulting speckle patterns spatially overlap, and they interfere at the camera plane. The intensity of the  $m$ -th camera pixel

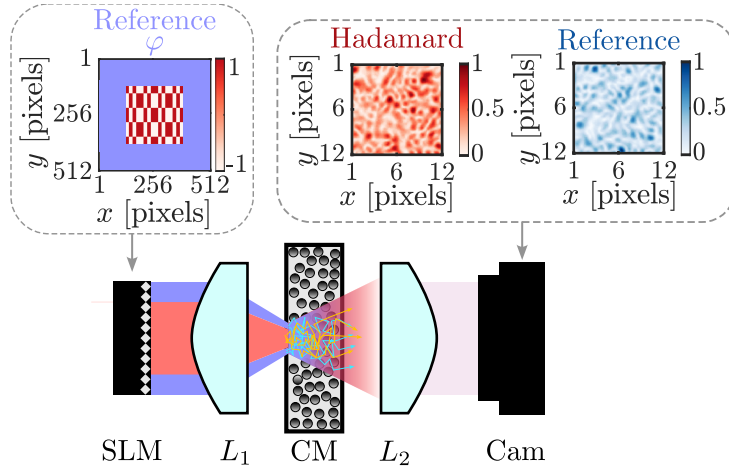


**Figure 4.8:** Internal reference for field reconstruction. The SLM is divided into two parts, which we highlight for illustration purpose with two different colors. A part of the SLM (in red) encodes the vectors of the Hadamard basis. The other part (in violet/blue) is used as a static reference, i.e., it remains the same for any vector of the basis. The resulting speckle patterns (reported independently for clarity) are superimposed and interfering at the camera plane. We measure the resulting intensity for different phases  $\varphi$  encoded in the reference part of the SLM, in order to reconstruct the phase of the output speckle pattern.

originating from the  $n$ -th SLM pattern is

$$I_{mn}^\varphi = |E_{mn}|^2 + |E_m^{\text{ref}}|^2 + 2|E_{mn}||E_m^{\text{ref}}|\cos(\phi_{mn} - \phi_m^{\text{ref}} + \varphi), \quad (4.4)$$

where  $\varphi$  is the global reference phase that we control. To reconstruct the complex amplitude, we shift the global phase  $\varphi$  and we measure the resulting intensity modulation. In our implementation, we choose to use "four phases method" [85, 112], i.e., we shift the reference phase by  $0, \pi/2, \pi$  and  $3\pi/2$ , and we use the measurements to compute the complex coefficient as

$$\frac{I_{mn}^0 - I_{mn}^\pi}{4} + i \frac{I_{mn}^{3\pi/2} - I_{mn}^{\pi/2}}{4} = E_{mn} (E_m^{\text{ref}})^* = t'_{mn}. \quad (4.5)$$

From this method we obtain an *effective* TM, since the reconstructed coefficient  $t'_{mn}$  also contains the information about the reference speckle. Nevertheless, it is possible to measure the constant  $E_m^{\text{ref}}$ , and use it to retrieve the original TM from the effective one. The downside of using internal reference is that it is only possible to characterize the TM in the camera pixels where the reference field is non-zero. Because also the reference field is a speckle pattern, there are many dark pixels where the phase cannot be measured. However, since our goal is to focus most of the light in only few points, not having access to the whole area of the camera is only a minor drawback compared to the significant advantage of greater stability. In fact, since the reference and Hadamard beams are co-propagating, their interference is not affected by the vibration and the drift of the optical components. On the other hand, an external reference propagates along a different optical path before recombining with the Hadamard beam. Therefore, any instabilities in the optical components of the setup introduce a phase noise which impairs the measurement of the phase of the TM.

### 4.1.3 Multi-port linear device

Suppose we have a single Gaussian input beam  $E_1^{\text{in}}$ . Through the system of SLM and complex medium, we generate a set of  $m$  output modes  $E_i^{\text{out}}$ , with  $i = 1, \dots, m$ , according to the transformation

$$\begin{bmatrix} E_{1,1}^{\text{out}} \\ E_{2,1}^{\text{out}} \\ \vdots \\ E_{m,1}^{\text{out}} \end{bmatrix} = \begin{bmatrix} t_{11} \\ t_{21} \\ \vdots \\ t_{m1} \end{bmatrix} E_1^{\text{in}}, \quad (4.6)$$

Our goal is to control the coefficients  $t_{i1}$ , with  $i = 1, \dots, m$ . Let us analyze the procedure. The input beam reaches a region of a phase-only SLM, where  $N$  segments of the SLM modulate the field locally, effectively generating  $N$  spatially separated modes with controlled phase. Thus, the input field  $E_1^{\text{in}}$  undergoes a transformation  $\hat{T}_{\text{SLM},1}$  with dimensions  $N \times 1$ . Next, the set of  $N$  modes enters the complex medium. We characterize the effect of the medium with a transmission matrix  $\hat{T}_{\text{CM},1}$ . The dimension of  $\hat{T}_{\text{CM},1}$  is  $M \times N$ , since it connects  $N$  input modes to  $M$  output speckles. We want to control only few modes out of the many ones at the output, and they should enclose the largest amount of the output power. We thus apply a projection  $\hat{P}$  (of size  $m \times M$ , where  $m$  is the number of modes we want to control) to select only the output speckles we are interested in, while zeroing out the intensity of the rest. The overall operation transforms an input beam into  $m$  outputs, according to the relation

$$\begin{bmatrix} E_{1,1}^{\text{out}} \\ E_{2,1}^{\text{out}} \\ \vdots \\ E_{m,1}^{\text{out}} \end{bmatrix} = \hat{P} \hat{T}_{\text{CM},1} \hat{T}_{\text{SLM},1} E_1^{\text{in}}. \quad (4.7)$$

Combining Eq. (4.6) and Eq. (4.7), we require that

$$\hat{P} \hat{T}_{\text{CM},1} \hat{T}_{\text{SLM},1} = \begin{bmatrix} t_{11} \\ t_{21} \\ \vdots \\ t_{m1} \end{bmatrix}. \quad (4.8)$$

To generate the output beams with the desired coefficients, we only need to invert Eq. (4.8) to find the transformation to be implemented with the SLM (note that we can freely choose  $\hat{P}$ , and  $\hat{T}_{\text{CM},1}$  is fixed and well characterized). In practice, we apply a phase conjugation, which has already been proven successful to focus light into few speckles [109]. Finally, we get the following relation:

$$\hat{T}_{\text{SLM},1} = \hat{T}_{\text{CM},1}^\dagger \hat{P}^\dagger \begin{bmatrix} t_{11} \\ t_{21} \\ \vdots \\ t_{m1} \end{bmatrix}, \quad (4.9)$$

which is the configuration that we encode into the SLM to implement the desired transformation.

Let us now move to the case of a set of mutually incoherent input beams. For the sake of concreteness, we focus on the case of 3 input and 3 output beams (a linear  $3 \times 3$ -port device) which we implement experimentally. Three mutually incoherent, non-overlapping beams  $E_1^{\text{in}}$ ,  $E_2^{\text{in}}$  and  $E_3^{\text{in}}$  reach different regions of the phase-only SLM, undergoing afterwards the same transformations described previously. Being mutually incoherent, each input beam generates its speckle pattern, which does not interfere with the others. Therefore, we can simply sum the independent speckle patterns to get the final result:

$$\begin{bmatrix} E_1^{\text{out}} \\ E_2^{\text{out}} \\ E_3^{\text{out}} \end{bmatrix} = \begin{bmatrix} \sum_{i=1}^3 E_{1,i}^{\text{out}} \\ \sum_{i=1}^3 E_{2,i}^{\text{out}} \\ \sum_{i=1}^3 E_{3,i}^{\text{out}} \end{bmatrix} = \sum_{i=1}^3 \hat{P} \hat{T}_{\text{CM},i} \hat{T}_{\text{SLM},i} E_i^{\text{in}} = \begin{bmatrix} t_{11} & t_{12} & t_{13} \\ t_{21} & t_{22} & t_{23} \\ t_{31} & t_{32} & t_{33} \end{bmatrix} \begin{bmatrix} E_1^{\text{in}} \\ E_2^{\text{in}} \\ E_3^{\text{in}} \end{bmatrix}. \quad (4.10)$$

Knowing from Eq. (2.40) the target coefficients  $t_{ij}$ , we only need to use Eq. (4.9) to correctly program each individual region of the SLM and obtain the desired output coherence matrix. Note that the required linear transformation  $\hat{T} = \sum_{i=1}^3 \hat{P} \hat{T}_{\text{CM},i} \hat{T}_{\text{SLM},i} = \sqrt{\mathbb{K}_{\text{out}}}$  is in general non-unitary (see App. B.1). This is not an issue for our implementation, since, due to the non-unitary nature of the TM, the overall transformation  $\hat{T}$  can be non-unitary. Interestingly, the expression of  $\hat{T}$  is not constrained by any requirement other than the passive modulation of the SLM [95].

## 4.2 Coherence control: experimental realization

In Fig. 4.9 we show the experimental setup, which comprises two main blocks. The first one (preparation) generates three fields characterized by a programmed coherence matrix, while the second block (verification) verifies that the encoded degrees of coherence correspond to the desired ones.

We use two phase-only SLMs (Meadowlark Optics P512) with  $512 \times 512$  pixels each. In the preparation stage, we use a first SLM (SLM<sub>1</sub>) to modulate three mutually incoherent input lasers (Thorlabs HRP050 and Meredith Instruments 633 nm HeNe lasers, and  $\approx 650$  nm FOSCO BOB-VFL650-10, see App. B.5). Next, we focus them onto an optical complex medium (ground glass diffuser, Thorlabs DG10-1500). The SLM<sub>1</sub> and the scattering medium together form the programmable multi-port linear device. Through wavefront shaping, the light scattered by the medium and collected by a lens forms three output beams.

In the verification stage, we use a second SLM (SLM<sub>2</sub>) to modulate the phase of the beams before a lens. This allows us to control which beam is

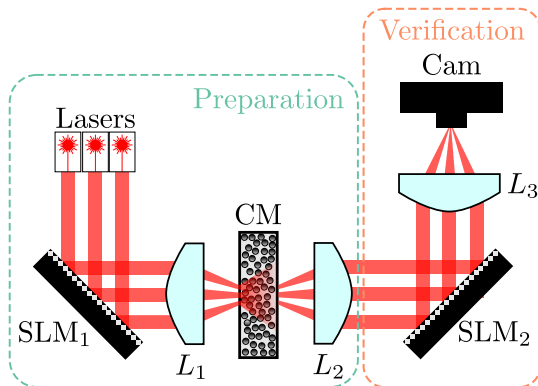


**Figure 4.9:** Experimental setup. We employ three different lasers as mutually incoherent inputs. The three lasers are modulated by a phase-only SLM, then they are focused onto a complex medium (ground glass diffuser) by a lens. The propagating beams are mixed by the complex medium and then collected by another lens. Through wavefront shaping, we obtain three output beams with the desired coherence matrix. The three output beams are focused by a third lens and interfere in the camera plane. A second SLM is used to characterize the degrees of coherence from the interference patterns.  $L_1$ ,  $L_2$ ,  $L_3$ : lenses; CM: complex medium; Cam: camera.

focused onto the camera plane and to which location. From the interference patterns measured with the camera (Basler acA640-750um), we reconstruct the mutual degree of coherence. In the following sections, we describe the procedures used to encode and measure the coherence matrix of the output fields.

### 4.2.1 Preparation

The transmission matrix of the complex medium must be characterized to employ it as a part of the reconfigurable multi-port linear device. Each element of the TM connects the field modulated by the  $n$ th pixel of  $SLM_1$  to the complex field of the  $m$ th output mode (a camera pixel used for TM characterization). We reconstruct the TM by configuring the SLM with each vector of a complete basis of the input modes, and measuring the corresponding complex fields at the output camera (see Sec. 4.1.2).

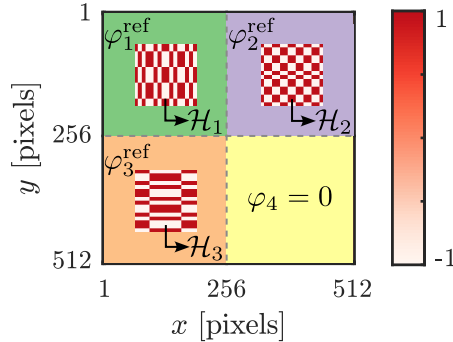
As discussed in Sec. 4.1.3, the speckle patterns generated by each input field are mutually incoherent, thus they do not interfere. Therefore, we assign a different transmission matrix  $\hat{T}_{CM,i}$  to each of the three non-overlapping input beams. Each laser is spatially phase modulated by a different quadrant

consisting of  $256 \times 256$  pixels of  $\text{SLM}_1$ , out of a total of  $512 \times 512$  pixels. The outer part of each quadrant is used as a static reference for the interference measurement, while we use an area of  $128 \times 128$  pixels (divided into 4096 square segments of 4 pixels each) to encode the Hadamard basis employed in the TM reconstruction (see Fig. 4.10). Once we have reconstructed the TM for each input laser, we can implement any desired linear transformation according to Eq. (4.9).

### 4.2.2 Linear port characterization

In this section we characterize the  $3 \times 3$ -port implemented with the system of complex medium and SLM. Each input  $E_i^{\text{in}}$  generates three outputs according to  $E_1^{\text{out}} = t_{1i}E_i^{\text{in}}$ ,  $E_2^{\text{out}} = t_{2i}E_i^{\text{in}}$  and  $E_3^{\text{out}} = t_{3i}E_i^{\text{in}}$ . Turning off two of the three inputs, we can experimentally measure the coefficients  $t_{1i}$ ,  $t_{2i}$  and  $t_{3i}$ .

Let us consider the input  $E_1^{\text{in}}$ , and we measure the output intensities  $I_1 = |t_{11}E_1^{\text{in}}|^2$ ,  $I_2 = |t_{21}E_1^{\text{in}}|^2$  and  $I_3 = |t_{31}E_1^{\text{in}}|^2$ . We show an example of the resulting intensity distributions in Fig. 4.11b. The output beams, resulting from a speckle pattern, do not show a clean Gaussian profile. This is detrimental for the reconstruction of the degree of coherence from the interference pattern. Therefore, we introduce three small circular apertures (0.5mm in diameter, spaced by roughly 2mm) before the second SLM (Fig. 4.11a). We show in



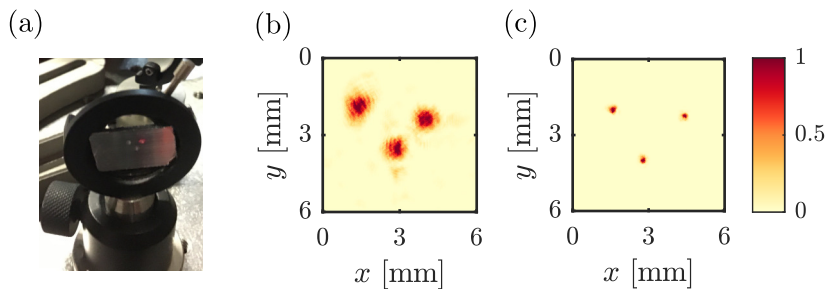
**Figure 4.10:** TM reconstruction with three mutually incoherent beams. The SLM area is divided into four quadrant, three of which are used for the independent modulation of the input beams (the fourth quadrant remains unused in our case). Note that each beam only illuminates the correspondent part of the SLM, without overlapping with the others. The central part of each quadrant ( $128 \times 128$  pixels) is used to encode the Hadamard basis. The outer part is used as internal reference for the reconstruction of the complex coefficients of the TM.



Fig. 4.11c the resulting spatially filtered beams.

We then characterize the output intensities when we modify the encoded coefficients. Given the desired coefficients, we calculate the needed SLM mask  $\hat{T}_{\text{SLM},i}$  according to Eq. (4.9). We then increase the magnitudes of  $t_{21}$  and  $t_{31}$  from 0 to 1, keeping  $t_{11}$  constant and equal to 1 (Fig. 4.12a). We measure that  $I_1$  decreases while we increase the intensities  $I_2$  and  $I_3$ . This happens mainly because the overall power distributed in the three outputs is conserved between the transformations. Thus, if we increase the intensities of the second and third output, then  $I_1$  must decrease accordingly. The linear port we want to implement is always normalized to the intensity of one focus, thus we are interested to the intensity ratios  $I_2/I_1$  and  $I_3/I_1$ , reported in Fig. 4.12b. We repeat the measurement 100 times (for a total time of about 30 minutes), resulting in the reported error bars, which show the maximum deviation from the mean value. From this characteristic, we can generate a look-up-table that tells us which coefficients  $t_{21}$  and  $t_{31}$  correspond to the desired output intensity ratio.

The next step is to characterize the cross-talk between the output beams. In fact, if the outputs are not completely independent, changing the intensity of one of them will affect the other two. In Fig. 4.12c we increase the intensity of the output  $I_2$  ( $t_{21}$  from 0 to 1), while keeping  $I_1$  and  $I_3$  constant. We then repeat the measurement increasing the magnitude of  $t_{31}$ . We find that the fluctuations of the intensity  $I_3/I_1$  are within the error bar of  $I_2/I_1$ , which is comparable to the typical error that we report in Fig. 4.12b. We then conclude that the systematic cross-talk is below the statistical noise, hence not relevant.



**Figure 4.11:** Spatial filtering. (a) Picture of the three small aperture (placed before SLM<sub>2</sub>) which are spatially filtering the generated beams. (b,c) Output fields' intensity distributions (b) before and (c) after the apertures.

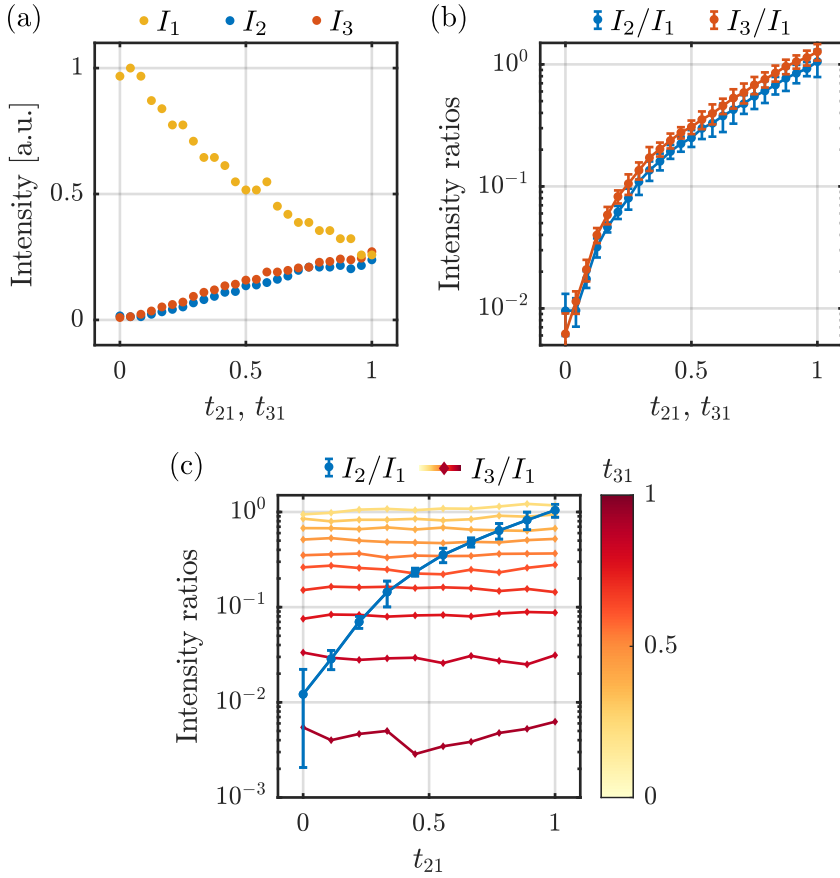


**Figure 4.12:** Linear port characterization. (a) Power conservation. If we increase  $t_{21}$  and  $t_{31}$ , keeping constant  $t_{11}$ , the amplitude of the high intensity output reduces, to conserve the overall power shared between the outputs. (b) Intensity ratios. We measured the ratios  $I_2/I_1$  and  $I_3/I_1$  for increasing  $t_{21}$  and  $t_{31}$ . The error bars (which show the maximum deviation from the mean value) are obtained repeating the measurement 100 times. (c) Cross-talk analysis. We modulate  $t_{21}$  from 0 to 1, while keeping  $t_{31}$  constant. We repeat the measurement changing the value of  $t_{31}$ . The error bars on  $I_2/I_1$  show the maximum deviation from the mean value.

### 4.2.3 Verification

The linear port described above is able to encode any desired coherence matrix. To verify the correctness of the encoding, we measure each entry of the coherence matrix, that is the mutual degree of coherence  $\gamma_{ij}$  of each field pair. We follow the measurement procedure described in Sec. 2.1.2, employing a focusing lens and a camera. The mutual coherence  $|\gamma_{ij}|$  can be derived from the following relations [see Eq. (2.23) and Eq. (2.24)]

$$|\gamma_{ij}| = \frac{I_i + I_j}{2\sqrt{I_i I_j}} \mathcal{V}, \quad (4.11a)$$

$$\mathcal{V} = \frac{I_{\max} - I_{\min}}{I_{\max} + I_{\min}}, \quad (4.11b)$$

where  $\mathcal{V}$  is the visibility,  $I_{\max}$  and  $I_{\min}$  are the maximum and minimum of the interference fringes, respectively, and  $I_i$  and  $I_j$  are the single fields' intensities. We highlight that all the quantities are defined at a single point in the camera plane, given that we can tune the relative phase of the interfering beams, as we discuss later. Moreover, even if  $\gamma_{ij}$  is a complex quantity, we only consider its magnitude, as a change in the phase results in a trivial shift of the interference fringes. In the following, in writing degree of coherence  $\gamma_{ij}$  we will always refer to its magnitude.

In Fig. 4.13 and Fig. 4.14, we summarize the procedure employed to measure the degree of coherence. Firstly, we use SLM<sub>2</sub> to apply a linear phase grating to two of the three output beams [113]. In the focal plane, which corresponds to the camera plane, the phase grating spatially displaces the two beams, allowing us to measure the intensity of the remaining one. In Fig. 4.13a and Fig. 4.13b, we show the intensity distribution of the first and the second beam, respectively, when the other two are displaced. We then use the phase grating to displace only one beam, and let the other two interfere, leading to the typical sinusoidal modulation across the area of the camera, as shown in Fig. 4.13c and Fig. 4.13d. In particular, Fig. 4.13c shows the intensity distribution when the mutual degree of coherence of the two interfering beams is low ( $\gamma_{ij} = 0.2$ ), while Fig. 4.13d shows the case of high degree of coherence ( $\gamma_{ij} = 0.8$ ), as visible from the contrast of the interference fringes. Figure 4.14a shows a cross-section of the interference fringes for three degrees of coherence ( $\gamma_{ij} = 0.2, 0.5, 0.8$ ). The modulation depth increases for higher degrees of coherence, as expected. Next, we modulate the phase of one of the beams (termed reference phase later) from 0 to  $2\pi$ . This modulation results in a spatial shift of the interference fringes. Thus, we are able to measure the visibility

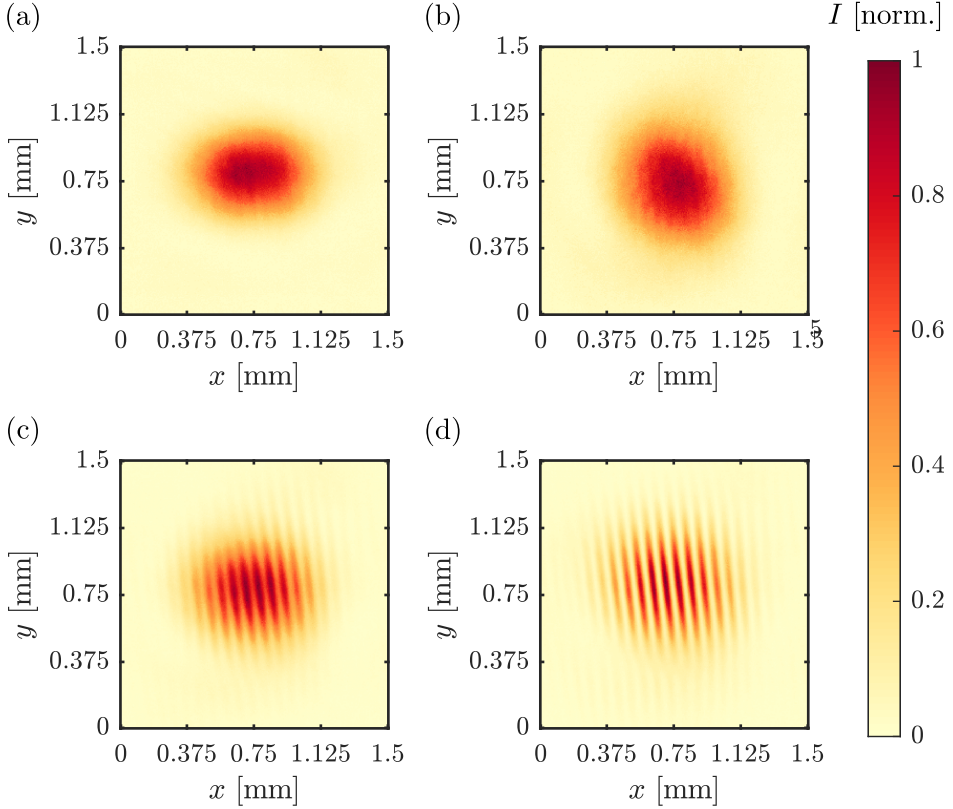


**Figure 4.13:** Reconstruction of the degree of coherence. (a, b) Intensity  $I$  of the (a) first and the (b) second beam. (c, d) Interference patterns for the degree of coherence ( $\gamma$ ) equal to (c) 0.2 and (d) 0.8.

at each pixel of the camera. Figure 4.14b shows examples of the intensity at a camera pixel with respect to the reference phase for three different degrees of coherence ( $\gamma_{ij} = 0.2, 0.5, 0.8$ ). From the visibility and the intensities of the single beams, we reconstruct the degree of coherence at a specific location, according to Eq. (4.11). As the reconstruction of the degree of coherence is noisier for regions of low intensities, we choose to only consider pixels where both the single-beam intensities are above 60% of their maximum value. We perform the previous procedure in parallel for all the considered pixels, and average the results to obtain the reconstructed degree of coherence  $\gamma_{ij}$ .

Inevitably, the encoding of a chosen coherence matrix is subject to errors, mainly due to non-perfect phase response of the SLM and errors in the TM characterization, leading to a discrepancy between the encoded and the recon-

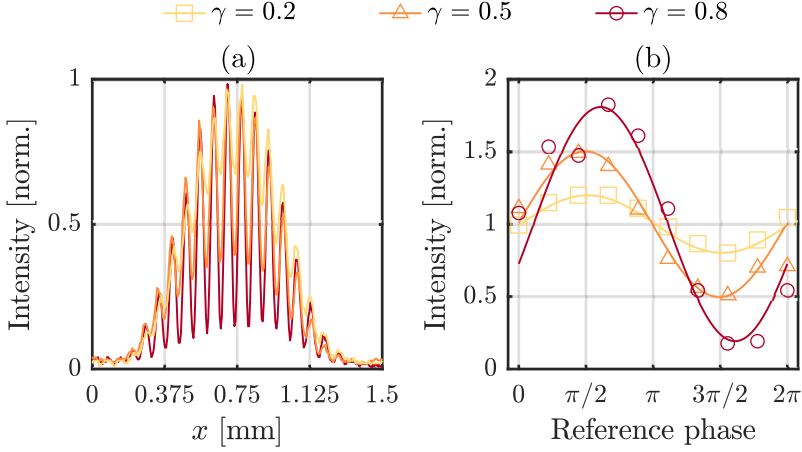


**Figure 4.14:** Modulation of the interference fringes. (a) Cross-sections of the intensity distributions for different values of  $\gamma$ . (b) Normalized intensity distribution at a fixed pixel as a function of the phase of one of the interfering beams (reference phase), which is swept from 0 to  $2\pi$ . The different colored dots correspond to measurements taken for different degrees of coherence. The solid lines are the cosine fits of the data points.

structured  $\gamma_{ij}$ . To minimize this discrepancy, we implement a gradient descent algorithm to optimize the multi-port linear device for minimum error. We illustrate this feedback mechanism considering a pair of fields  $E_i$  and  $E_j$ . At the  $n$ th iteration step, we encode the degree of coherence  $\gamma_{ij}^{\text{enc}}(n)$ , and reconstruct  $\gamma_{ij}^{\text{rec}}(n)$ . We evaluate the encoding error  $\varepsilon(n) = \gamma_{ij}^{\text{rec}}(n) - \gamma_{ij}^{\text{enc}}(n)$  and, for the next iteration, we correct the encoded value following the relation

$$\gamma_{ij}^{\text{enc}}(n+1) = \gamma_{ij}^{\text{enc}}(n) + \eta\varepsilon(n), \quad (4.12)$$

where  $\eta$  is the feedback strength, that we used for all the coherence matrices. From the new values of  $\gamma_{ij}^{\text{enc}}(n+1)$  for each pair, we construct the corrected linear port. We reiterate the process until we are satisfied with the final encoding error ( $\varepsilon < 0.01$  in our case). The gradient descent is performed a single time in order to obtain the correct SLM phase mask that leads to the desired output coherence matrix. The phase masks obtained with this final procedure would generate the correct coherence matrix as long as the optical system is stable (note that in the case of ground glass diffusers we are not limited by the stability of the complex medium, but mainly by the pointing stability of the lasers [95]). We illustrate the optimization procedure in Fig. 4.15. We want to encode the values  $\gamma_{12} = 0.3$ ,  $\gamma_{13} = 0.5$  and  $\gamma_{23} = 0.6$ . At each iteration, we correct

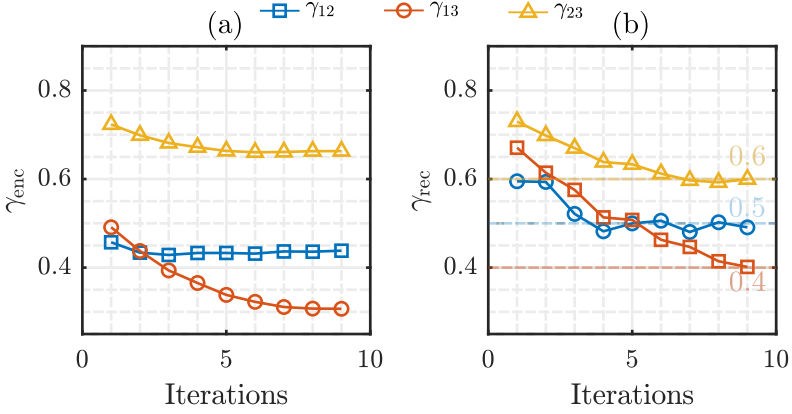


**Figure 4.15:** Feedback. (a) The encoded values  $\gamma_{enc}$  are iteratively corrected using the error between the desired and the measured degrees of coherence. (b) Consequently, the reconstructed degrees of coherence  $\gamma_{rec}$  converge to the desired values, which in this case are  $\gamma_{12} = 0.3$ ,  $\gamma_{13} = 0.5$  and  $\gamma_{23} = 0.6$ . Note that the encoded values do not start from the desired degrees of coherence because there are few prior feedback iterations that are not shown in the figure.

the encoded values (Fig. 4.15a), while the reconstructed degree of coherence converge to the desired quantity (Fig. 4.15b).

Figure 4.16 shows an example of the achieved precision in the control of the degree of coherence. Here, we report the reconstructed degrees of coherence  $\gamma_{rec}$ , with respect to the encoded values  $\gamma_{enc}$ . We encoded coherence matrices with identical degrees of coherence between each field pair, i.e.,  $\gamma_{12}^{enc} = \gamma_{13}^{enc} = \gamma_{23}^{enc}$ , ranging from 0 to 1. The reconstructed and the encoded degrees of coherence agree to within an average error of 0.004 in the region between 0.2 and 0.8. Outside this range, we observe deviations from the expected behavior. For low coherence, the measurement of  $\gamma_{ij}$  is affected by the background noise caused by the uncontrolled modes of the complex medium, whereas for high coherence we are limited by the self-coherence of the input lasers (see App. B.4).

#### 4.2.4 Results

We now show the level of control over the coherence matrix achievable with the presented implementation. The coherence matrix is completely defined by its off-diagonal values, which are the mutual degrees of coherence of the field-field pairs. We can therefore assign to each coherence matrix a vector

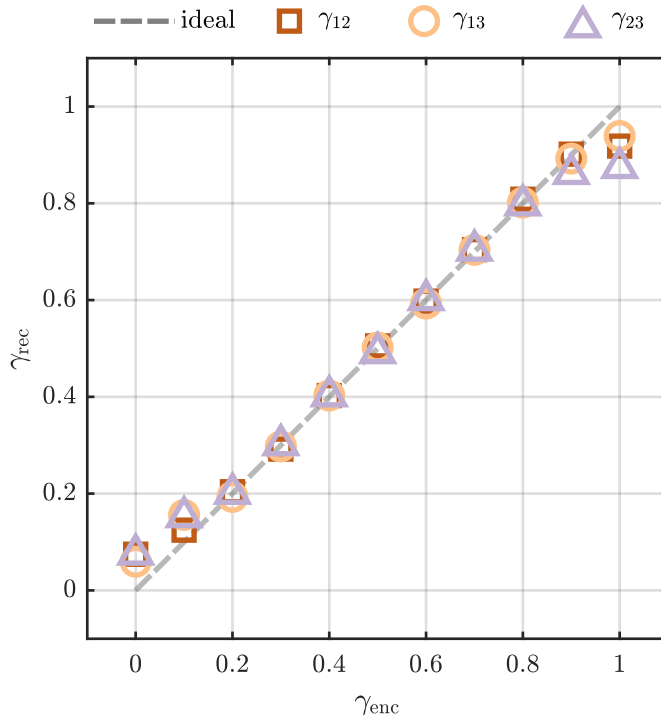


**Figure 4.16:** Reconstruction of the degree of coherence. Example of degree of coherence control. We show the reconstructed degrees of coherence ( $\gamma_{rec}$ ) with respect to the encoded ones ( $\gamma_{enc}$ ). We choose the degrees of coherence of the three pairs of fields ( $\gamma_{12}$ ,  $\gamma_{13}$  and  $\gamma_{23}$ ) to be equal.

$\boldsymbol{\gamma} = [\gamma_{12}, \gamma_{13}, \gamma_{23}]$ , and visualize all the possible vectors in a space where the axes are the magnitudes of the mutual degrees of coherence. Note that the positive semi-definiteness of the coherence matrix bounds the domain of allowed vectors (see Sec. 2.1.3). We discretize the three-dimensional space in a cubic grid with a step size of 0.1. In Fig. 4.17a, we show the experimentally achieved coherence matrices. The blue (red) dots represent the measured (encoded) vectors. We restrict ourselves to the region of degrees of coherence between 0.2 and 0.8, where the reconstructed coherence matrices do not have a large deviation with respect to the encoded ones, caused by technical limitations (see Fig. 4.16 and App. B.4). To graphically make more evident the typical distance between encoded and reconstructed coherence matrices, we show in Fig. 4.17b-d the orthographic projections of the three-dimensional space. The blue dots represent the reconstructed vectors, while the red circles with a radius

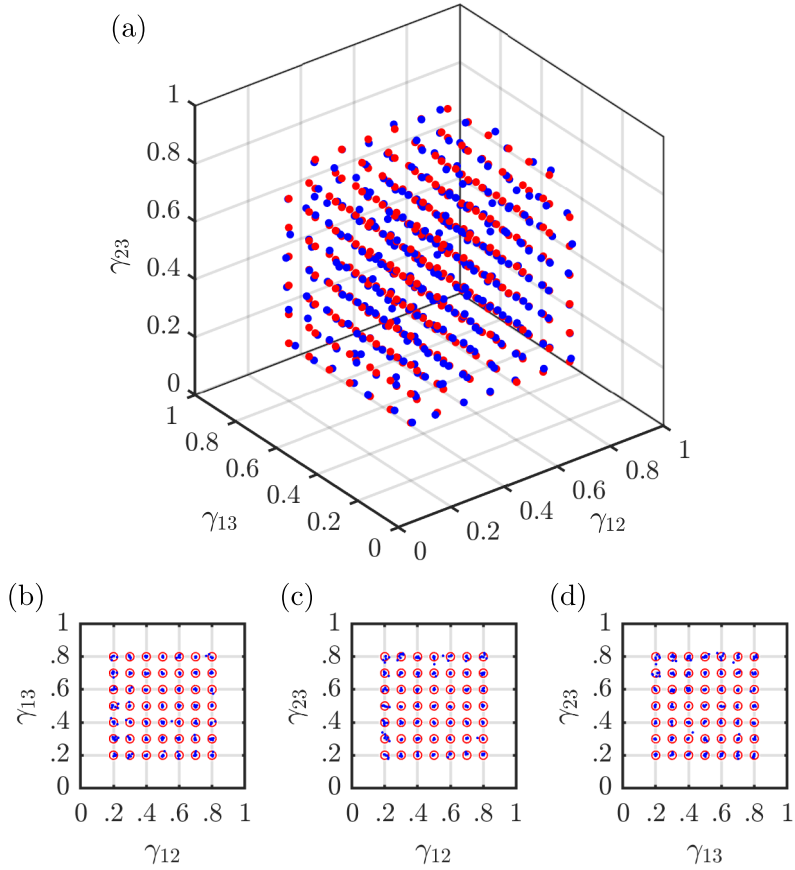


**Figure 4.17:** Coherence matrix control. (a) Coherence matrix space. Each point of the space represents a different coherence matrix, for which the off-diagonal elements are given by the three coordinates of the point  $[\gamma_{12}, \gamma_{13}, \gamma_{23}]$ . The blue and the red dots are the encoded and reconstructed coherence matrices, respectively. The encoded degrees of coherence range from 0.2 to 0.8, and the grid has a step size of 0.1. (b-d) Two-dimensional orthogonal projections of the three-dimensional space. The blue dots represent the measured vectors, while the red circles with radius 0.025 are centered on the encoded vectors.



of 0.025 are centered on the encoded matrices, and provide a visual reference.

As a quantitative measure for the accuracy of our coherence matrix control scheme, we define, for each measured point, the error  $\varepsilon$  as the root-mean-square distance between the encoded and the reconstructed vector in the space of the coherence matrices:

$$\varepsilon = \sqrt{\sum_i (\gamma_i^{\text{enc}} - \gamma_i^{\text{rec}})^2}. \quad (4.13)$$

Here the subscript  $i$  indicates the field-field pairs  $i = \{1,2\}, \{1,3\}, \{2,3\}$ . Figure 4.18a shows the histogram of the errors. For the majority of the coherence matrices, the error is below 0.01, which is the threshold value set in the gradient descent optimization. The mean value of the error is 0.01.

Next, we characterize the statistical error associated with the measured  $\gamma$ . To do so, we repeat the previously described reconstruction procedure 10 times for each vector of the space. We then estimate the statistical error  $\sigma$  as the standard deviation of the measured ensemble. In Fig. 4.18b we plot the histogram of  $\sigma$ . The average statistical error is 0.008. This justifies the chosen threshold in the optimization algorithm.

Finally, we characterize the whole system of fields with a single quantity, i.e., the overall coherence. The overall coherence  $\mathcal{S}$  is a real number ranging from 0 (full incoherence) to 1 (full coherence) and measures the coherence of the whole system, independently of how it is shared between the degrees of

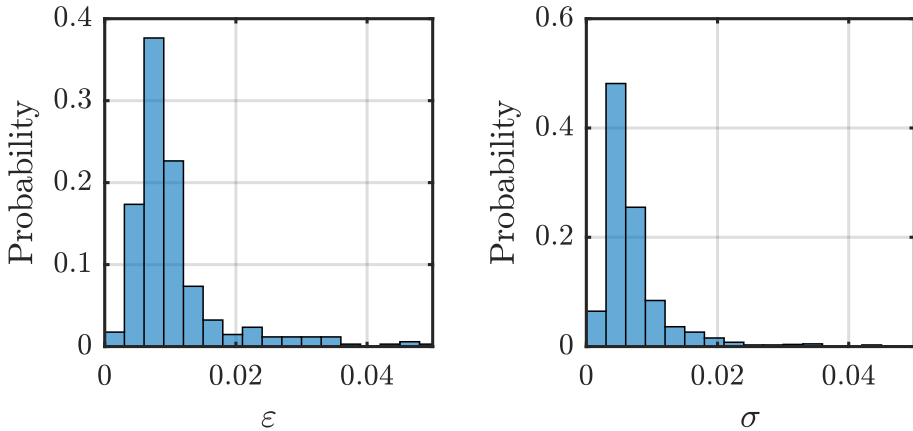


**Figure 4.18:** Systematic and statistical errors. (a) Histogram of the error  $\varepsilon$ , i.e., the distance between the reconstructed and the encoded values. (b) Histogram of the statistical error  $\sigma$ . For each encoded coherence matrix, we repeat the reconstruction of the three degrees of coherence 10 times. The statistical error  $\sigma$  is calculated as the standard deviation of each ensemble.

coherence (see Sec. 2.1.3). In Fig. 4.19, we plot the reconstructed ( $\mathcal{S}_{\text{rec}}$ ) versus encoded ( $\mathcal{S}_{\text{enc}}$ ) overall coherence, computed from all the measured vectors shown in Fig. 4.19. The average error (defined as  $|\mathcal{S}_{\text{enc}} - \mathcal{S}_{\text{rec}}|$ ) over all the measurements is 0.003.

### 4.3 Conclusion

In summary, we have presented an experimental technique to program the coherence matrix of a set of spatially separated fields, based on a  $3 \times 3$ -port linear optical device, implemented with wavefront shaping of mutually incoherent inputs that propagate through a complex medium. By sampling the set of allowed coherence matrices, we have shown that we can encode and successfully retrieve the majority of the matrices within an average error of 0.01. Remarkably, to our best knowledge this is the first time that the spatial coherence of multiple fields is controlled in a single-shot fashion. Single-shot means that, once the correct phase mask is programmed into the SLM, the spatial coherence modulation occurs after a single propagation through the system, in contrast with previous works which rely on the collection of a large ensemble of phase masks introduced by some active device [72–74].

Our work adds an important tool to the available methods for controlling various attributes of light. In particular, our complex medium-based device can be especially useful for the implementation of large-scale multi-port devices. In fact, to increase the number of controlled fields with the same performance in terms of coherence control, it is sufficient to maintain a constant background,

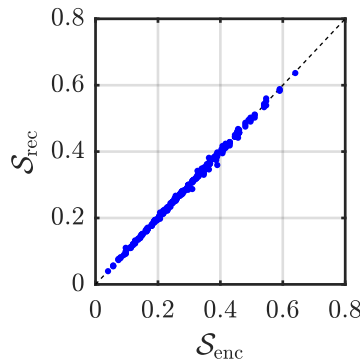


**Figure 4.19:** Encoded overall coherence  $\mathcal{S}_{\text{enc}}$  vs. reconstructed one  $\mathcal{S}_{\text{rec}}$ . The blue dots are the measured values, while the dashed line represents the ideal relation.

which allows us to retain the same minimum coherence (see App. B.4). We can achieve this by maintaining a constant number of SLM pixels per input laser [109], for example by employing a larger SLM. Increasing the number of SLM pixels (i.e., the active area) is a trivial task compared to stabilizing a large interferometer, as needed in the case of photonic integrated circuits. Finally, complex media may prove particularly useful when planning to extend coherence control to other degrees of freedom of light. Indeed, a multi-scattering medium is not limited to spatial modes, but mixes several other degrees of freedom, such as time, polarization, and transverse mode. We can exploit this property by generating a linear port that operates over multiple degrees of freedom, thus opening up the control of a coherence matrix to multiple degrees of freedom. We will elaborate on this topic in the outlook section.

# 5

---

## Conclusions & Outlook

Optical coherence is a topic of fascinating depth, that continues to be rich in phenomena to investigate even two centuries after Thomas Young's first experiments on the double-slit [114]. Already the interference fringes measured in those experiments help us to appreciate the large influence that coherence has on science. In fact, even though they constitute the foundation of coherence theory, they are still essential for the study of particle-wave duality [24]. Regarding more recent findings, Wolf presented a unified theory of coherence and polarization, highlighting the intimate relationship between these two phenomena, and, consequently, the greater impact of coherence on statistical optics [40, 115]. Since then, the concept of coherence matrix has evolved to include other degrees of freedom [41, 116]. However, in terms of coherence control, previous research was only able to control the properties of a single light source or a pair of fields [72–77]. In this thesis, a technique and application for controlling the coherence matrix of a set of fields are presented for the first time. We hope that this work will serve as inspiration for further research on the topic.

We will now summarize the findings and discuss their implications. In Ch. 2, we presented a general technique that enables us to manipulate the coherence matrix of a set of fields via a linear transformation. This is the first proposal for a method that controls the mutual coherences between an arbitrary number of fields, and it serves as the basis for the rest of the results presented in this

work. We then proposed in Ch. 3 a communication system that encodes the data to be transmitted in the coherence matrix. We analyzed the performance of this communication scheme, so to compare it quantitatively with other techniques, deriving the SNR, the maximum bit-rate and the spectral efficiency with respect to the number of transmitted light beams. We concluded that the maximum bit-rate increases quadratically with the number of transmitted fields, until it saturates at approximately the value of the input sources linewidth, thus leading to attractive data rates. As an example, a LED have a typical bandwidth (full width at half maximum) of  $\approx 25$  THz [117], resulting in the saturation of the maximum bit-rate at  $\approx 27$  THz (see Eq. (3.38)). However, the quadratic gain in bit-rate occurs at the cost of spectral efficiency, which instead decreases quadratically with the number of field pairs. As we have seen in the introduction (Ch. 1), researchers are already squeezing the available capacity of current fiber technology, trying to exploit the entire low-loss spectral window with high spectral efficiency [5]. Without the ability to increase the input linewidth because it is not supported by transmission fibers, the low spectral efficiency renders mutual coherence coding unsuitable for long-haul fiber communications. Nevertheless, this limitation is not present in FSO. In fact, beams sent through the atmosphere are not restricted in linewidth: we could use LEDs with bandwidth limited only by our technical ability to compensate for dispersion and modulate broadband light. This could further improve the maximum bit-rate, bringing FSO performance toward that reached by fiber-based communications.

Finally, in Ch. 4, we experimentally realize an implementation of the coherence matrix control based on wavefront shaping of light propagating through a complex medium. Importantly, this is a passive implementation, meaning that, once the SLM is programmed, the coherence modulation occurs with a single pass through the device. This allows the technique to be much faster than other previous implementations, that rely on the collection of a large ensemble of phase masks introduced by some active device [72–74]. Currently, employing SLMs does not appear as a winning option over integrated circuits because of their very limited refresh rates (ranging from 10 to 100 Hz for a liquid-crystal SLM to tens of kHz for DMDs [118]). It is worth noting, however, that there are proposals to fabricate SLMs that operate in the GHz range [119, 120], which would push our complex media-based linear port to work at electronic frequencies, thus making it suitable for applications. On the other hand, SLMs are very attractive because of the millions of degrees of freedom they provide to modulate the light field, allowing us to control the propagation through the complex medium to realize the desired linear port. The

---

most interesting aspect is that to increase the number of fields involved, we only need to increase the size of the SLM or use more than one. This is in stark contrast to photonic integrated circuits, which require a complicated network of interferometers to implement a linear port, that rapidly become impractical with increasing number of input fields. This particular implementation based on free-space optics is particularly suited for being employed in FSO. Using broadband input light is favorable for FSO, where partially coherent beams are less affected by atmospheric turbulence compared to the coherent counterpart [21, 37]. In addition, the implementation would be much cheaper than the high-capacity fiber-based systems. In fact, long-haul communication systems need very stable lasers with countless narrow frequency bands that can be addressed independently with fast modulators, and spectrometers that are used to detect the complex quadrature modulated signals multiplexed in hundreds of wavelengths. Our proposal for the implementation of mutual coherence coding, in contrast, only need LEDs, SLMs and balanced photodetectors. This is in line with the main advantages of FSO, including low installation and maintenance costs. We can therefore conclude that our implementation has the promising prospect of becoming a useful resource for free-space optical communications, once SLM technology will provide modulators fast enough to be comparable to driving electronics.

**Outlook: combining degrees of freedom** Throughout this thesis, we were mainly concerned with the spatial degree of freedom (DoF). This is the most extensively studied DoF in the field of complex media, as it is the most obviously affected by multiple scattering. However, as it has been previously reported, complex media also act on many other DoFs, such as polarization [121], time [92] and transverse electromagnetic (TEM) modes [122]. We can exploit this phenomenon to extend the linear port concept to other DoFs. Using wavefront shaping and complex media provides a particularly compact implementation that extends the control to additional DoFs without requiring other dedicated components (e.g., birefringent materials for polarization and SLM or phase plates for TEM modes). Having access to a multi-DoF linear port opens up the possibility of manipulating a multi-DoF coherence matrix [41, 116]. To illustrate the concept, let us consider the case of two light beams (spatial positions  $s \in \{1, 2\}$ ), with two possible polarization states (horizontal and vertical,  $p \in \{H, V\}$ ) and two TEM modes (e.g., orbital angular momenta (OAM)  $\ell \in \{+, -\}$ ). We can collect all the orthogonal modes in a single vector

$$\mathbf{Y} = \left[ Y_{1,H}^+, Y_{1,H}^-, Y_{1,V}^+, Y_{1,V}^-, Y_{2,H}^+, Y_{2,H}^-, Y_{2,V}^+, Y_{2,V}^- \right]^T. \quad (5.1)$$

In analogy with Eq. (2.25), we then define a coherence matrix  $\mathbb{K}_Y$  which includes the three degrees of freedom

$$\mathbb{K}_Y = \langle \mathbf{Y} \mathbf{Y}^\dagger \rangle = \begin{bmatrix} \gamma_{1,1,H,H}^{+,+} & \gamma_{1,1,H,H}^{+,-} & \gamma_{1,1,H,V}^{+,+} & \cdots & \gamma_{1,2,H,V}^{+,-} \\ \gamma_{1,1,H,H}^{-,+} & \gamma_{1,1,H,H}^{-,-} & \gamma_{1,1,H,V}^{-,+} & \cdots & \gamma_{1,2,H,V}^{-,-} \\ \gamma_{1,1,V,H}^{+,+} & \gamma_{1,1,V,H}^{+,-} & \gamma_{1,1,V,V}^{+,+} & \cdots & \gamma_{1,2,V,V}^{+,-} \\ \vdots & \vdots & \ddots & \ddots & \vdots \\ \gamma_{2,1,V,H}^{-,+} & \gamma_{2,1,V,H}^{-,-} & \gamma_{2,1,V,V}^{-,+} & \cdots & \gamma_{2,2,V,V}^{-,-} \end{bmatrix}. \quad (5.2)$$

where

$$\gamma_{s_1, s_2, p_1, p_2}^{\ell_1, \ell_2} = \frac{\langle Y_{s_1, p_1}^{\ell_1} (Y_{s_2, p_2}^{\ell_2})^* \rangle}{\sqrt{\langle |Y_{s_1, p_1}^{\ell_1}|^2 \rangle \langle |Y_{s_2, p_2}^{\ell_2}|^2 \rangle}}, \quad (5.3)$$

with  $s_1, s_2 \in \{1, 2\}$ ,  $p_1, p_2 \in \{H, V\}$  and  $\ell_1, \ell_2 \in \{+, -\}$ . This coherence matrix contains all the correlations between the different orthogonal modes, thus providing a complete description of the statistical properties of the optical system. We can show that the method explained in Sec. 2.2 and Sec. 4.1.3 remains valid also in the case of different DoF, allowing us to control the coherence matrix  $\mathbb{K}_Y$ . Let us start from  $N_f$  incoherent fields  $\mathbf{X} = [X_1, X_2, \dots, X_{N_f}]$ . Note that the number of inputs is given by the product of the dimensionality of each DoF. For instance, for  $n = 2$  spatial positions,  $m = 2$  TEM modes and  $r = 2$  polarization states, we get  $N_f = n \times m \times r = 8$ . Each field  $X_i$  is modulated by a region of an SLM, applying a transformation  $\hat{T}_{\text{SLM}, i}$ . Then each field propagates through the complex medium, which redistributes the field power to the orthogonal modes in all the three DoFs through a transformation  $\hat{T}_{\text{CM}, i}$ . Finally, we apply a projection  $\hat{P}$  that selects the fields at two spatial positions, two polarizations and 2 TEM modes. The output field vector  $\mathbf{Y}$  is

$$\mathbf{Y} = \begin{bmatrix} Y_{1,H}^+ \\ Y_{1,H}^- \\ \vdots \\ Y_{2,V}^- \end{bmatrix} = \sum_{i=1}^{N_f} \hat{P} \hat{T}_{\text{CM}, i} \hat{T}_{\text{SLM}, i} X_i = \hat{T} \mathbf{X}. \quad (5.4)$$

If we then consider the beams that need to be transmitted for communication purposes, we only have two of them:

$$\begin{aligned} Y_1 &= Y_{1,H}^+ + Y_{1,H}^- + Y_{1,V}^+ + Y_{1,V}^-, \\ Y_2 &= Y_{2,H}^+ + Y_{2,H}^- + Y_{2,V}^+ + Y_{2,V}^-. \end{aligned} \quad (5.5)$$

---

Formally, the relationship between the output coherence matrix  $\mathbb{K}_Y$  and the linear transformation  $\hat{T}$  is still the same as that derived in Eq. 2.39 and Eq. 2.40. To control the output coherence matrix, it is then sufficient to program the SLM with the amplitude and phase derived according to Eq. 4.9, analogously to the case restricted to spatial coherence. The experimental challenge comes from the characterization of the multi-DoF transmission matrix (MDoF-TM)  $\hat{T}_{\text{CM},i}$  of the multi-scattering medium. Note that this was already achieved in multi-mode fibers with time, polarization and spatial degrees of freedom [123]. Let us address the task one degree of freedom at a time. We have already explained in Sec. 4.1.2 how to characterize the spatial-TM. Next step is the characterization of the polarization-TM, which is a relatively easy task since it only involves two orthogonal modes. The combination of spatial and polarization TM (PS-TM) has already been reported [121, 124]. We also conducted a similar experiment, the setup of which is illustrated in Fig. 5.1a. Our version is simpler than the ones previously reported, because it only consider a vertically polarized input field, which is the case we are interested in for the implementation of the linear port. Manipulating only one input polarization state reduces the complexity of the optical setup, at the cost of a reduced control over the output field. A gaussian vertically polarized laser beam is modulated by an SLM and pass through a complex medium. The resulting speckle pattern is divided into orthogonal polarizations with a polarizing beam splitter (PBS), and then measured with two independent cameras, which provide the spatial resolution. For each vector of the input basis generated by the SLM (see Sec. 4.1.2), we measure the spatially and polarization resolved output field, reconstructing a TM which contains both spatial and polarization information. We then use the measured PS-TM to generate foci with arbitrary polarization. We show in Figs. 5.1b-d two generated foci at two desired positions, with orthogonal polarizations (horizontal and vertical) and different intensity. The experimental verification consists of measuring the intensity of the two foci after a linear polarizer with different rotations (horizontal, vertical and diagonal, in Figs. 5.1b,c,d, respectively). We also generated a single field with circular polarization, as a superposition of two orthogonally polarized foci ( $Y_1^H$  and  $Y_1^V$ ) in the same spatial position (1) and with  $\pi/2$  phase difference, i.e.,

$$Y_1 = Y_1^H + i Y_1^V . \quad (5.6)$$

We report in Fig. 5.2a the measured intensity for different rotation of the linear polarizer. In Fig. 5.2b we show the dependence of the peak focus intensity on the angle of the main axis of the linear polarizer. For a circularly polarized beam, we would expect a constant intensity, independent of the angle of the



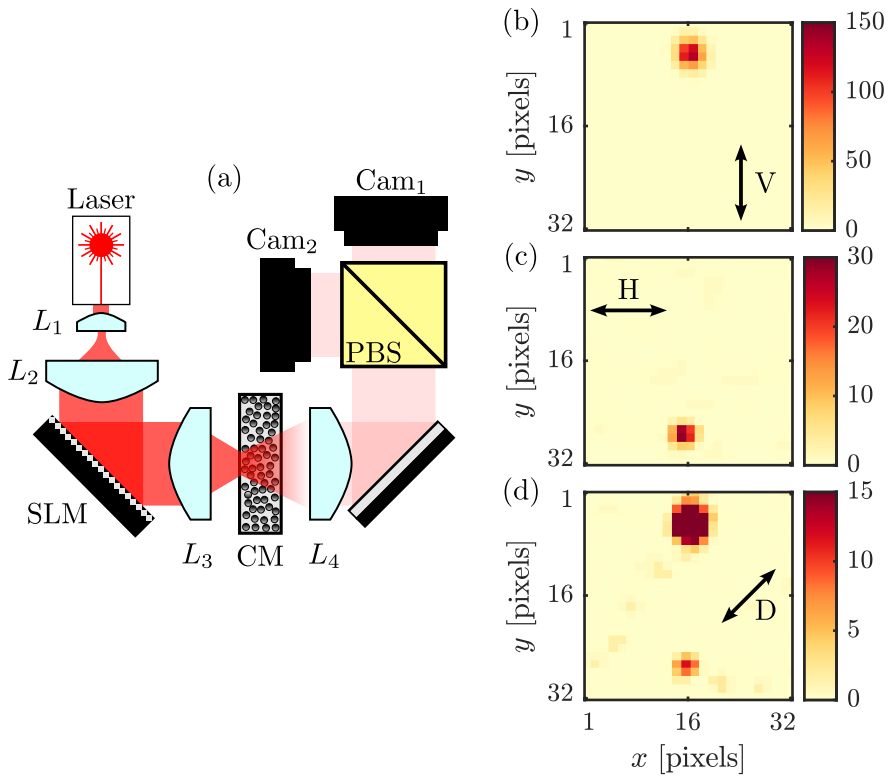


**Figure 5.1:** Polarization and spatial transmission matrix (PS-TM). (a) Experimental setup for the PS-TM reconstruction. A laser beam is expanded to match the SLM aperture. After propagation through the complex medium, a polarizing beam splitter is used to divide the resulting speckle patterns in two orthogonal components. The two cameras measure the spatially and polarization resolved speckle for the TM reconstruction. (b-d) Employing the knowledge of the PS-TM, we generate two foci with orthogonal polarizations. We use a linear polarizer to measure only one polarization component: (b) vertical, (c) horizontal and (d) diagonal.

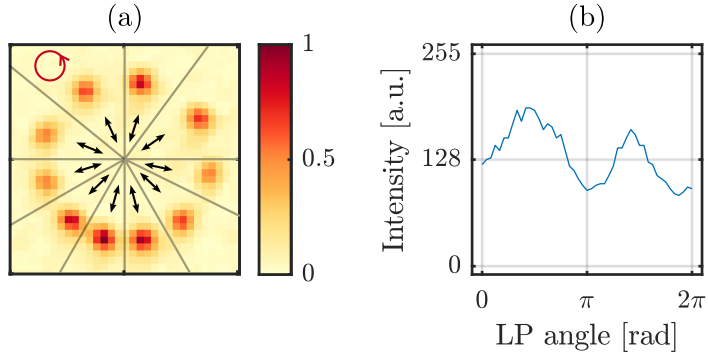


**Figure 5.2:** Generating circularly polarized light after the complex medium. (a) We generate a single focus with circular polarization, as a superposition of horizontally and vertically polarized foci with a  $\pi/2$  relative phase. The focus is always in the same position, but we show it displaced for easier visualization. The black arrow represents the angle of the main axis of the linear polarizer. (b) Dependence of the peak focus intensity on the angle of the LP. For circularly polarized light the intensity should remain constant. The modulation is caused by residual ellipticity in the polarization of the generated focus.

linear polarizer. The reported modulation is caused by residual ellipticity in the generated focus.

The following step is to characterize the TEM-TM. This is a challenging goal, which, to the best of our knowledge, has not yet been reported for the case of a multi-scattering medium, while it has been achieved for multi-mode fibers [123], whose working principle is based on TEM mode mixing. So far, researchers used a Fourier filtering technique to control the TEM mode of a single speckle [94, 122] or of the whole speckle pattern [111]. Reconstructing the TEM-TM, though, requires to measure the mode content of each speckle. We can propose the following experimental procedure. At the output of the complex medium, we select a single speckle with an iris to disregard the spatial degree of freedom. We then use a mode sorter, which redirects the energy carried by each mode composing the speckle to a different spatial position. It can be implemented using a SLM in combination with another optical element, such as a mirror [125], or even a complex medium, like a multiple scattering material [126] or a multi-mode fiber [127]. For each input vector (note that we again restrict ourselves to controlling only the phase of the input), we use the mode sorter to measure the mode content of the speckle (up to 55 simultaneous modes [125]). We repeat the measurement for the whole input basis, until

we reconstruct the TEM-TM of the complex medium. To combine also the spatial information, we need to perform the mode sorting for more speckles, which, although experimentally challenging, it is a straightforward extension of the TEM-TM reconstruction. Finally, adding a PBS we can reconstruct the 3DoF-TM. In order to use the system as a linear port, one would need to reconstruct the 3DoF-TM for each incoherent input beam. We show in Fig. 5.3 the proposed setup in the case of a 3DoF-TM with two spatial positions, two TEM modes and two polarization states.

Performing this experiment would lead to the following interesting results:

- characterizing a polarization-TEM-TM would allow to generate vector fields after a multi-scattering medium (note that this was already achieved in multi-mode fibers [123]), with potential applications in the area of super-resolution microscopy [128];
- to the best of our knowledge, it would be the first implementation of a linear port that operates with multiple degrees of freedom, adding an interesting tool for photonics technology;

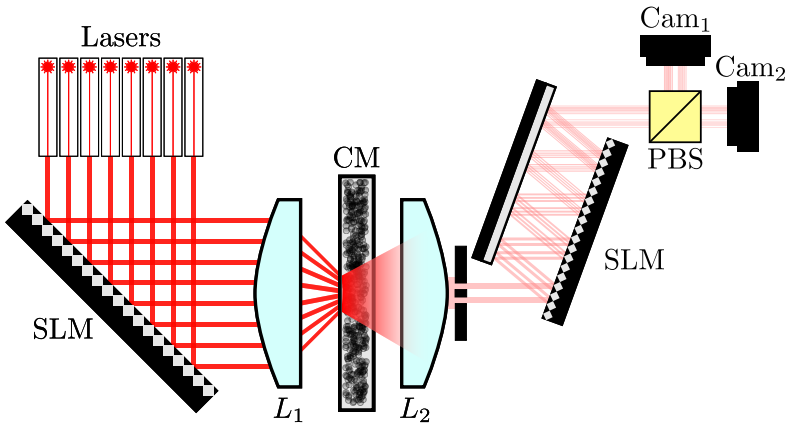


**Figure 5.3:** Multi-DoF linear port. The linear port controls the relationship between 8 input mutually incoherent beams and 8 output modes, combinations of spatial, polarization and TEM degrees of freedom. To realize the linear port, we need to measure the 3DoF-TM of the complex medium for each input field. To decouple the output modes, we use an iris to select two speckles (spatial DoF), a mode sorter (composed of a SLM and a mirror) that decompose each of the two speckles in its constituent TEM modes, and a PBS, which separates the two orthogonal polarizations. Two cameras measure the two resulting distributions, from which we can extract the information about spatial, polarization and TEM degrees of freedom.

- we can employ the obtained linear port to control a multiple DoFs coherence matrix. This is relevant for the field of statistical optics, since it would be the first demonstration of fine control of a multi-DoF coherence matrix. Moreover, if applied to mutual coherence coding, it would lead to an increased number of signals per transmission fiber. In fact, given  $n$  fibers (or light beams in FSO), each carrying  $m$  transverse modes (e.g., using few-modes fibers [5]) and  $p = 2$  orthogonal polarizations, the number of mutual coherences that we can control is  $N_p \approx (n \times m \times p)^2/2$ . The communication scheme is sketched in Fig. 5.4. Interestingly, this new approach would not change the analysis reported in Sec. 3.3.2. In fact, the detected signal  $S_{s_1, s_2, p_1, p_2}^{\ell_1, \ell_2}$  is

$$S_{s_1, s_2, p_1, p_2}^{\ell_1, \ell_2} \propto \left\langle Y_{s_1, p_1}^{\ell_1} \left( Y_{s_2, p_2}^{\ell_2} \right)^* \right\rangle = \left\langle \sum_{n=1}^{N_f} t_{in} X_n \sum_{m=1}^{N_f} t_{jm}^* X_m^* \right\rangle, \quad (5.7)$$

and it still formed by  $N_f(N_f - 1)$  incoherent field pairs, which give rise to the same optical beat noise, limiting factor of mutual coherence coding. However, although resorting to more DoFs does not affect the performance in terms of bit-rate, SNR and spectral efficiency, controlling the multi-DoF coherence matrix adds the technical opportunity to increase the number of signals sent, without increasing the number of transmission

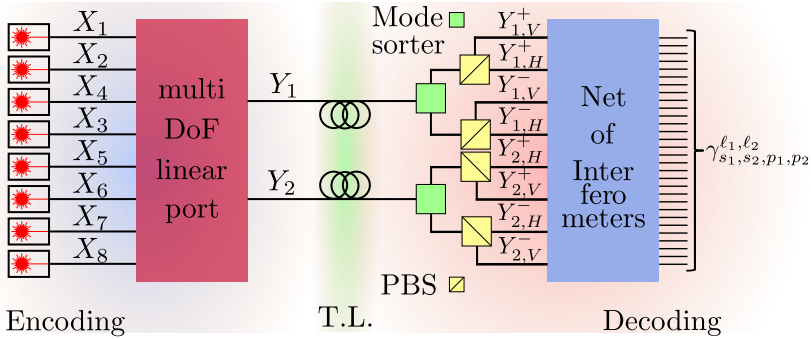


**Figure 5.4:** Mutual coherence coding with multiple DoFs. A multi-DoF linear port generates two fields  $Y_1$  and  $Y_2$  with controlled multi-DoF coherence matrix, starting from a set of mutually incoherent fields. The two fields are transmitted to the receiver side, which uses a set of mode sorters and PBS to decouple the different DoFs, generating 8 fields with different combinations of spatial position, polarization and TEM mode. Finally, after an appropriate mode conversion, we use a net of interferometers to reconstruct the 28 mutual coherences encoded with the multi-DoF linear port.

paths. Finally, we also note that the receiver, illustrated in Fig. 5.4 with discrete components, can also be implemented with a single system of SLM and complex medium (similar to the linear port), greatly reducing the number of components needed.

In conclusion, throughout this thesis, we have provided novel solutions to address old problems in optical coherence and communication. Certainly a company will not find mature engineering results that can have an immediate impact on the market. Nevertheless, we hope that, from these pages, curious scientists and engineers will find new inspirations and alternative perspectives, allowing them to produce useful technologies that otherwise would not have been considered.



## Related project: towards a three-dimensional quartic intensity

Light propagation is most commonly treated with the theoretical tools of Fourier optics [42]. Under the assumptions of Fourier optics, techniques such as the Gerchberg-Saxton algorithm allow the two-dimensional control of the focal intensity through the shaping of the amplitude and phase of the field in the back focal plane [129]. However, when a beam is strongly focused with a high numerical aperture (NA) objective, the relationships of Fourier optics do not apply, and we have to resort to a full vectorial treatment of the field [130]. Interestingly, thanks to the added degree of freedom given by polarization, our control of the intensity distribution is not restricted to the focal plane. In fact, by shaping amplitude, phase and polarization of the field in the back focal plane of the objective, we gain control over the three-dimensional spatial distribution of the focal intensity [131, 132]. Full control over the vector field in a given plane has already been demonstrated using SLMs [133] and digital micro-mirror devices [134]. In this chapter, we make use of the expertise acquired in the use of SLMs (see Ch. 4) to build an experimental setup capable of generating an complex vector field in the back focal plane of a high-NA lens. We plan on employing this control to realize a three-dimensional quartic (3DQ) focal intensity, i.e., an intensity distribution that has zero curvature along the three Cartesian components. Generating a 3DQ intensity could find applications in laser cutting of metals and microlithography [132]. Moreover, in the field

of levitated nanoparticles, a non-quadratic intensity distribution represents an exciting opportunity to reconstruct non-Gaussian quantum motional states [135]. A 3DQ intensity can also be of interest for Bose-Einstein condensates, where a three-dimensional (quasi)uniform potential is desirable [136].

## A.1 Theory

Let us consider the intensity distribution  $I$ , defined in the focal space whose Cartesian coordinates are  $x$ ,  $y$  (transverse) and  $z$  (longitudinal). The distribution  $I$  is 3DQ if it has zero curvature along  $x$ ,  $y$  and  $z$ , i.e.,

$$\frac{\partial^2 I}{\partial i^2} = 0, \quad \text{for } i \in \{x, y, z\}. \quad (\text{A.1})$$

The paraxial beam (i.e., the field in the back focal plane) needed to generate a 3DQ intensity distribution results from the superposition of an azimuthally polarized (AP) field and a radially polarized (RP) field [132]. Even when strongly focused, RP and AP fields maintain orthogonal local polarization states, thus they do not interfere in the focal space. In addition, for a high enough NA, the focus of a RP beam is characterized by a central maximum (Fig. A.1c), whereas the focus of an AP beam assumes a doughnut shape (Fig. A.1d). Given the aforementioned properties, it is possible to design a recipe to derive the paraxial distributions which result in a 3DQ intensity when strongly focused:

- we shape amplitude and phase distributions of the RP component, so as to obtain a quartic distribution along  $z$  (Fig. A.1a). For this first step, we can disregard the AP component, since it has zero intensity along the optical axis (Fig. A.1b);
- then, we obtain a flat-top intensity in the focal plane by compensating the RP intensity (Fig. A.1d) with the AP doughnut distribution (Fig. A.1c).

The resulting 3DQ intensity is reported in Figs. A.1e,f. A rigorous derivation of the complex vector field that, strongly focused, results in a 3DQ intensity can be found in Ref. [132]. We followed an alternative solution derived by R. Gutiérrez-Cuevas and M. A. Alonso [137]. They provide the expressions of amplitude, phase and polarization distributions to obtain a 3DQ intensity in the focus. The amplitude and phase distributions of orthogonal polarization components of the derived field are reported in Fig. A.2.

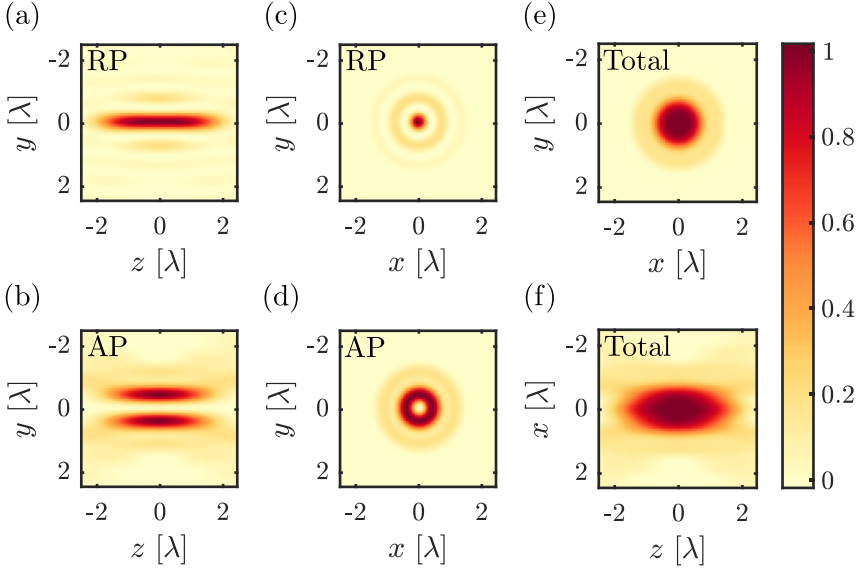


**Figure A.1:** Radially polarized (RP) and azimuthally polarized (AP) components of the 3DQ intensity. (a,b)  $xz$ -plane ( $y = 0$ ) of the (a) RP and (b) AP components of the 3DQ intensity. Note that the distribution is symmetric around the  $z$  axis. (c,d)  $xy$ -plane ( $z = 0$ ) of the (c) RP and (d) AP components. (e,f) Total 3DQ distribution in the (e)  $xy$ -plane and (f)  $xz$ -plane.

## A.2 Experiment

For the experimental realization of the 3DQ intensity distribution we need to be able to generate a desired distribution of phase, amplitude and polarization in the back focal plane of a high-NA objective. To control the field distribution, we make use of a pair of SLMs, one to control amplitude and phase of the modulated field, and the second one to locally rotate the polarization. We name this section of the setup *generation* part. We then strongly focus the programmed beam with a high-NA oil-immersion objective. To measure the intensity distribution in the focus, we resort to a nano-scatterer, which is able to detect the local intensity with sub-wavelength resolution. This *reconstruction* part of the setup allows us to measure the three-dimensional intensity distribution in a spatial region around the focus.



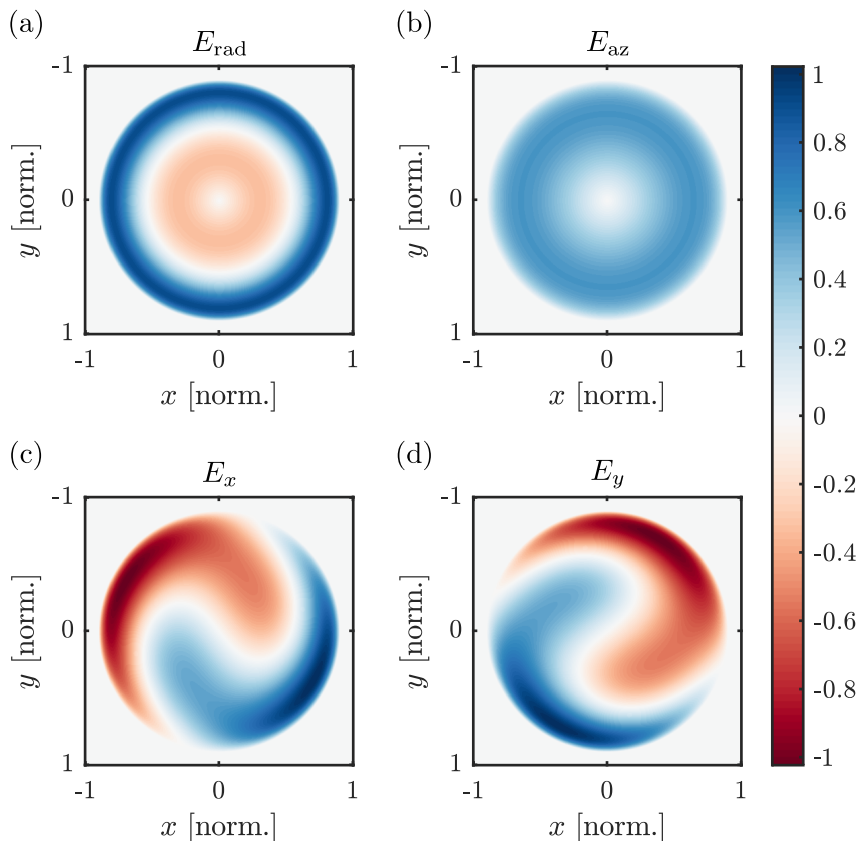


**Figure A.2:** Field distributions in the back focal plane of a high-NA objective to obtain a 3DQ focus. (a,b) Total paraxial field divided into (a) radially polarized component  $E_{\text{rad}}$  and (b) azimuthally polarized component  $E_{\text{az}}$ . (c,d) Total paraxial field divided into (c) horizontally polarized component  $E_x$  and (d) vertically polarized component  $E_y$ .

### A.2.1 Generation setup

The generation part of the setup is sketched in Fig. A.3. A He-Ne laser (Thorlabs HRP050, 633 nm) is coupled into a single mode fiber (SMF) to obtain a clean fundamental Gaussian mode. Next, a telescope (lenses  $L_1$  and  $L_2$ ) is used to obtain a nearly constant intensity across the SLM aperture. We also use a linear polarizer (LP) to ensure vertical polarization, that matches the SLM phase modulation axis. A beam splitter (BS) is used to redirect the light towards the first SLM ( $\text{SLM}_1$ ), and to produce a reference beam that we can employ to perform an interference measurement to detect the phase of the programmed

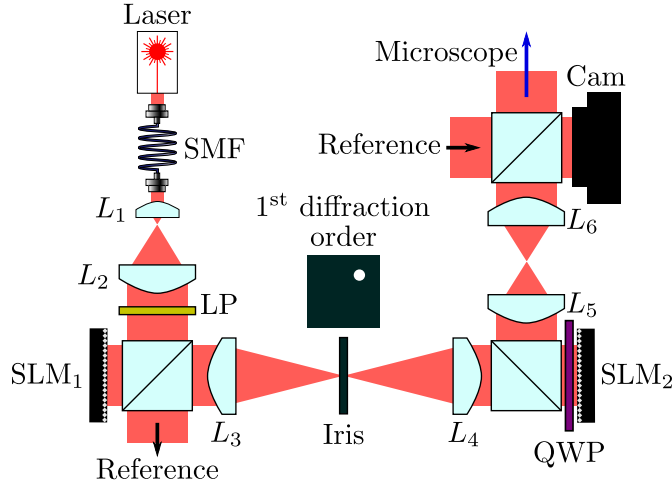


**Figure A.3:** Generation part of the setup. A HeNe laser (633 nm) is coupled into a single mode fiber (SMF) to obtain a clean fundamental Gaussian beam. Then, the beam is expanded with a telescope (lenses  $L_1$  and  $L_2$ ) to get a nearly-constant intensity illuminating the first SLM ( $SLM_1$ ). A linear polarizer (LP) select the vertical polarization matching the SLM modulation axis. A beam splitter (BS) redirects part of the light towards the SLM, while the rest is used as a reference for the interference measurement. The modulated beam is imaged with a  $4f$ -system (lenses  $L_3$  and  $L_4$ ) to the plane of the second SLM ( $SLM_2$ ). We position an iris in the focal plane of lens  $L_3$  to select only the first diffraction order. In front of  $SLM_2$  we place a quarter-wave plate (QWP) to implement the polarization rotation. A second BS is used to redirect the light towards the microscope (reconstruction part). A pair of lenses in a  $4f$ -configuration ( $L_5$  and  $L_6$ ) images the  $SLM_2$  plane to the back focal plane of the objective and to a camera. A final BS is used to mix the modulated light with the reference field for interference measurements. To avoid power losses, the two BSs in front of the SLMs can be replaced by D-shaped mirrors.

field distribution. After the  $SLM_1$  phase modulation, the beam propagates again through the BS and continues towards the second SLM ( $SLM_2$ ). A  $4f$ -system (lenses  $L_3$  and  $L_4$ ) is used to image the  $SLM_1$  plane onto the  $SLM_2$  plane. An iris is positioned in the focal plane of  $SLM_1$  to select the first diffraction order and perform simultaneous amplitude and phase modulation with a single SLM (see following section and Refs. [138–140]). Before reaching the second SLM, the beam polarization is modified by a quarter-wave plate (QWP). The beam is then modulated and reflected by  $SLM_2$ . It passes again through the QWP, and it gets redirected towards the microscope (reconstruction setup). The system of

SLM and QWP is used to locally control the polarization angle [141, 142]. A final pair of lenses ( $L_5$  and  $L_6$ ) generates the image of the SLM<sub>2</sub> plane in the back focal plane of the microscope objective. Another BS is added after  $L_6$ , redirecting the light towards a camera, to characterize the field distribution in the back focal plane. In particular, to measure the phase distribution, we let the aforementioned reference (nearly constant, unmodulated Gaussian beam) and the generated field interfere in the camera plane. Note that, to avoid power loss, the beam splitters can be eliminated, using a D-shaped mirror and a slight tilt in the SLM to redirect the reflected light.

### A.2.2 Field distribution control with two SLMs

Here, we will describe how to use a system of two SLMs to generate a controlled field distribution in amplitude, phase and polarization. The first SLM is used to control both amplitude and phase. There are various techniques that allow such control [139]. The common trait of this class of methods is that they rely on phase gratings, which allow to locally redirect a tunable portion of the field's power to the first diffraction order in the Fourier space of the SLM. A lens is then placed at focal distance from the SLM to generate its Fourier image (lens  $L_3$  in Fig. A.3). An iris positioned in the focal plane of  $L_3$  is finally used to select only the first diffraction order. On top of the phase grating (which is used for amplitude modulation), a slower phase envelope spatially modulates the phase of the input beam. These powerful techniques allows to independently control both amplitude and phase distributions with a single SLM, adding the advantage of filtering out the unwanted portion of unmodulated light which is reflected by the dead spaces between the pixels of the SLM [139].

The polarization control is instead achieved using a system of a QWP and an SLM [141]. In Fig. A.4 we show the evolution of the polarization state rotated through the interaction with the SLM and the QWP. We can analyze the working principle with Jones calculus [143]. The vertically polarized input beam ( $E_{\text{in}} = [0, 1]^T$ ) is converted to circular polarization through a QWP with its fast axis oriented  $+45^\circ$  (counterclockwise) from the horizontal axis. The beam is then modulated and reflected by the SLM, resulting in a change of sign for the horizontally polarized component of the field, and a pixel-wise added phase  $\phi_{x,y}$  for the vertically polarized component, where  $\{x, y\}$  is position of the considered pixel. Finally, the beam passes again through the QWP, but with opposite propagation direction. Thus, effectively the QWP behaves as having its fast axis oriented  $-45^\circ$  (counterclockwise) from the horizontal axis. We multiply the individual Jones matrices to find the combined operation  $\hat{T}_{x,y}$  for

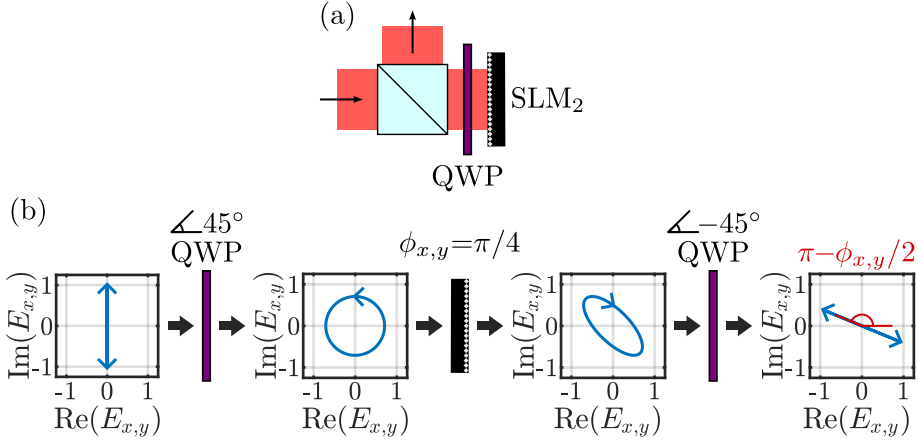


**Figure A.4:** Polarization modulation. (a) Experimental setup for the pixel-wise polarization rotation. (b) Polarization state evolution. The vertically polarized light is converted into right-hand circular by a QWP with its fast axis oriented  $45^\circ$  counterclockwise with respect to the horizontal axis. Then the pixel  $\{x, y\}$  SLM add a phase  $\phi_{x,y}$  to the vertical component of the field, resulting in an elliptical polarization (in this case  $\phi_{x,y} = \pi/4$ ), and the reflection adds a  $\pi$  phase to the horizontal component. Finally, the second pass through the QWP converts the light back to linear polarization, but with its angle rotated by  $\pi/2 - \phi_{x,y}/2$ .

the  $\{x, y\}$  SLM pixel we get

$$\begin{aligned} \hat{T}_{x,y} &= \frac{1}{\sqrt{2}} \begin{bmatrix} 1 & -i \\ -i & 1 \end{bmatrix} \begin{bmatrix} -1 & 0 \\ 0 & e^{i\phi_{x,y}} \end{bmatrix} \frac{1}{\sqrt{2}} \begin{bmatrix} 1 & i \\ i & 1 \end{bmatrix} \\ &= e^{i(\phi_{x,y} + \frac{\pi}{2})} \begin{bmatrix} \cos\left(\frac{\pi}{2} - \frac{\phi_{x,y}}{2}\right) & \cos\left(\pi - \frac{\phi_{x,y}}{2}\right) \\ \sin\left(\frac{\pi}{2} - \frac{\phi_{x,y}}{2}\right) & \sin\left(\pi - \frac{\phi_{x,y}}{2}\right) \end{bmatrix}. \end{aligned} \quad (\text{A.2})$$

Therefore, the resulting effect is to rotate pixel-wise the polarization axis counterclockwise by  $(\pi/2 - \phi_{x,y}/2)$ . Moreover, we add an unwanted phase  $(\pi/2 + \phi_{x,y}/2)$ , which needs to be carefully compensated by the first SLM (which controls the phase). Therefore, it is crucial to carefully align the two SLMs, to avoid introducing phase distortions.

In Fig. A.5, we show an example of programmed field distribution, i.e., a radially polarized second order Laguerre-Gaussian beam. We show the simulated and the measured distributions for the total intensity (Figs. A.5a and A.5d), and the intensity of the horizontally polarized (Figs. A.5b and A.5e) and vertically polarized components (Figs. A.5c and A.5f). In Figs. A.5g and A.5h we show

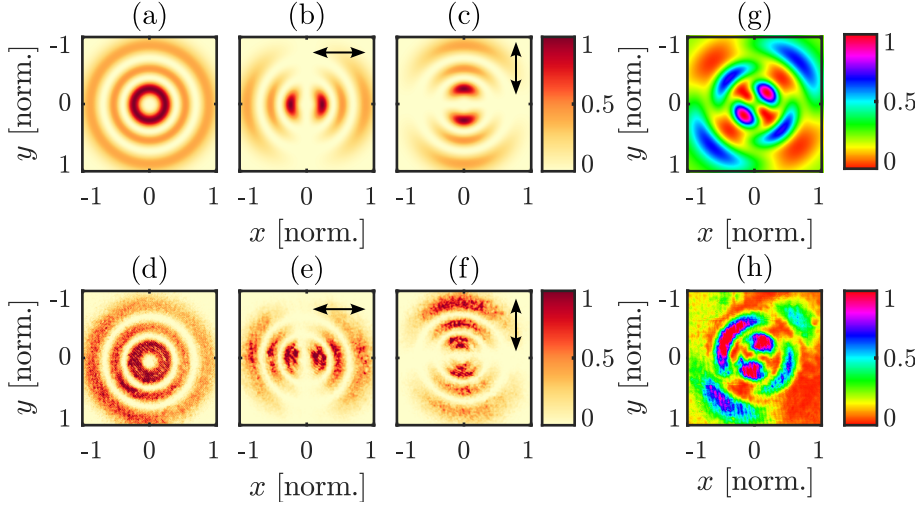


**Figure A.5:** Generation of a radially polarized second order Laguerre-Gaussian field. (a-c, g) Simulated and (d-f, h) measured distributions. (a,d) Total intensity. (b,c,e,f) Intensity of the (b,e) horizontal and (c,f) vertical component of the generated field. (g,h) Intensity distribution resulting from the interference of the second order Laguerre-Gaussian field (linearly polarized for this measurement) and a reference beam with constant amplitude equal to the maximum amplitude of the generated field.

respectively the simulated and measured intensity distributions resulting from the interference of the generated field and a plane reference field with same peak intensity. Note that for this last measurement the generated beam was set to linear polarization.

### A.2.3 Field distribution correction

Mainly due to deviations from flatness of the reflective surfaces of the SLMs, caused by production process [144], the fields generated with our system deviates from the desired distributions. Many techniques are present in the literature to correct for the non-ideal response of SLMs [144–146]. In the following, we will explain the different strategies that we implemented to correct each of the controlled degrees of freedom.

**Amplitude correction:** We use our system to generate a field with the desired amplitude distribution  $A_{\text{target}}$ . We first characterize the amplitude of the generated beam from the intensity measured by the camera in Fig. A.3. Then,

we subtract the desired intensity ( $I_{\text{target}} = A_{\text{target}}^2$ ) and the measured one ( $I_{\text{meas}}$ ) to derive the pixel-wise error  $\varepsilon = I_{\text{target}} - I_{\text{meas}}$ . Next, we use the measured error to correct the encoded amplitude. Ideally, one iteration would be enough to obtain the desired output intensity. However, we found it experimentally more convenient to use an iterative approach. Therefore, for each iteration we encode a new amplitude of the form  $A_{n+1} = \sqrt{A_n^2 + \eta \varepsilon_n}$ , where  $\eta$  is a suitable constant (in our case  $\eta = 0.1$ ). The protocol continues until the average error reaches the desired value (in the order of 0.001 in our implementation). An example of the measured intensity before and after amplitude correction is reported in Figs. A.6a and A.6b.

**Phase correction:** Aberrations, i.e., phase distortions, are a severe problem affecting any optical system. The need to compensate for aberrations in astronomy initiated the field of *adaptive optics* [147], which later led to wavefront shaping (see Ch. 4). Here, we choose to follow the method proposed in Ref. [144] to correct for the aberrations introduced by the SLMs. The method makes use of a Gerchberg-Saxton (GS) algorithm [129] to determine the phase errors from the distorted shape of a focused Laguerre-Gaussian (LG) beam. To this aim, we use our generation setup to obtain a first-order LG mode, i.e., a beam with a spiral phase, constant amplitude and homogeneous linear polarization (phase mask in Fig. A.7a). We then focus it with a lens and we record the focal plane with a camera. In Fig. A.7c we show an example of a distorted intensity

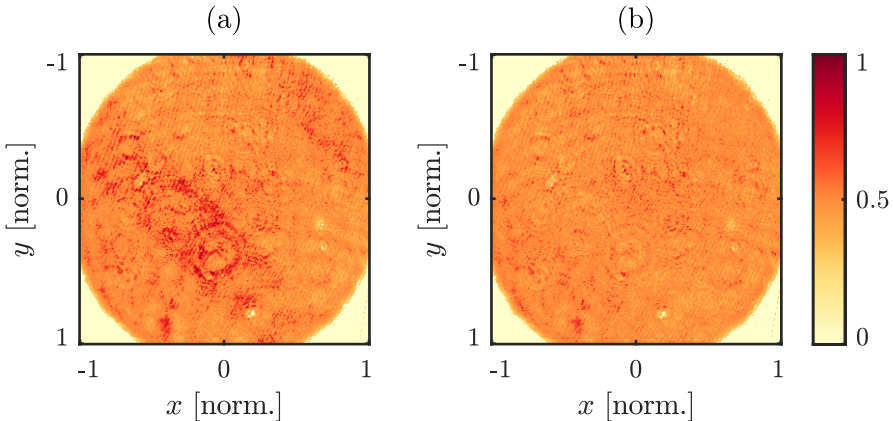


**Figure A.6:** Amplitude correction. The target distribution is a disk with constant amplitude. (a,b) Measured intensity (a) before and (b) after performing amplitude correction.

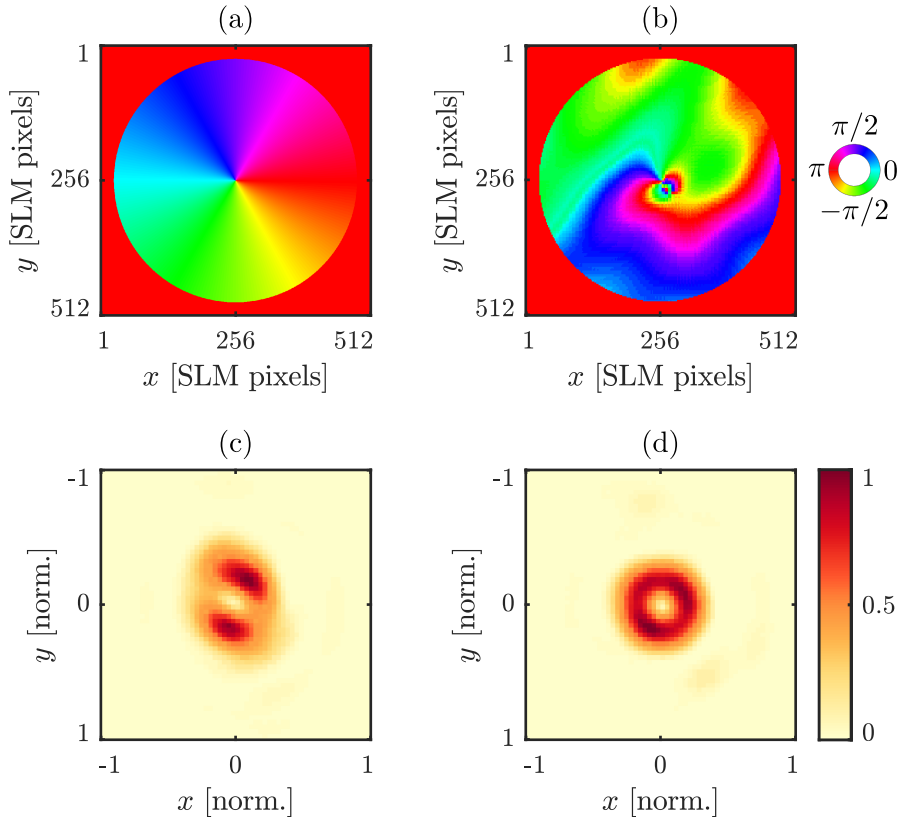


**Figure A.7:** Phase correction. (a,b) Phase masks implemented with the SLM. (c,d) Intensity distribution recorded in the focal plane. The initial phase mask (a) leads to a distorted focus (c). After the phase correction we obtain the corrected phase mask (b), leading to the desired doughnut shape in the focus (d).

distribution recorded in the focal plane. From the GS algorithm, we extract the phase distortion that leads to the measured intensity, and we use it to correct the SLM phase mask (see Fig. A.7b) and retrieve the target intensity distribution (Fig. A.7d). Interestingly, the derived correction for the SLM mask is still valid for different generated field distributions [144]. Moreover, this technique has the added advantage of optimizing the entire optical setup, since the extracted aberrations include the effect of optical elements other than the SLMs.

**Polarization correction:** In order to correct for polarization inhomogeneities, we again make use of the camera image of the generated beam. Our polarization

control consists of locally rotating the polarization, which remains linear. Therefore, by simply adding a horizontal linear polarizer, we can measure from the resulting intensity the polarization rotation introduced by each pixel. Given a linearly polarized input with constant amplitude and phase ( $E_{\text{in}} = [0, 1]^T$ ), the pixel-wise intensity  $I_{x,y}$  dependence on the phase  $\phi_{x,y}$  introduced by a pixel in position  $\{x, y\}$  of SLM<sub>2</sub> is

$$I_{x,y} = |\hat{T}_{HLP} \hat{T}_{x,y} E_{\text{in}}|^2 = \frac{1 + \cos(\phi_{x,y})}{2}, \quad (\text{A.3})$$

where  $\hat{T}_{HLP}$  is the Jones matrix of the horizontally oriented linear polarizer [143], and  $\hat{T}_{x,y}$  represents the rotation of the polarization axis operated by the system of SLM<sub>2</sub> and QWP [see Eq. (A.2)]. We can then measure the resulting intensity corresponding to a phase  $\phi_{x,y}$  ranging from 0 to  $2\pi$ , and correct with a look-up table for any deviation from the ideal characteristics expected from Eq. (A.3). In Fig. A.8, we show the intensity (measured after a horizontal LP) of a beam programmed to have constant horizontal polarization, before (Fig. A.8a) and after (Fig. A.8b) correction.

#### A.2.4 Reconstruction setup

The generation part of the setup allows us to obtain a desired complex vector field distribution in a given plane. We make sure that this plane coincides with the back focal plane of a high-NA, oil immersion objective (Plan Apo 100X,

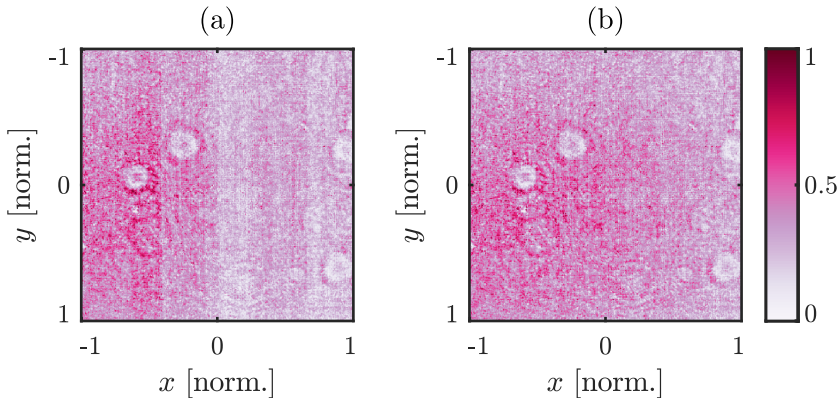


**Figure A.8:** Polarization correction. (a,b) Recorded intensity of a beam with constant amplitude and horizontal polarization after a horizontal linear polarizer. (a) Before and (b) after correction. The circles are caused by dirt present in the camera.



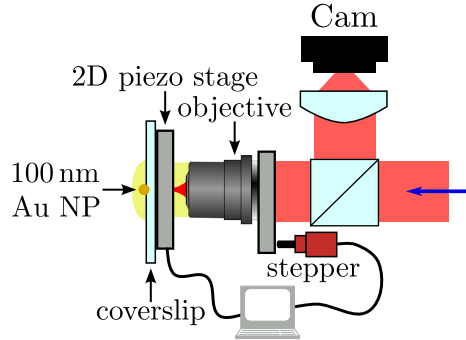


**Figure A.9:** Reconstruction setup. The generated beam is focused by a high-NA oil-immersion objective. The focused intensity is probed by a gold nanoparticle (100 nm in diameter), which is moved in the transverse plane by a 2D piezo stage, and along the optical axis by a stepper motor. Index-matched oil is present between the objective and the coverslip and on top of the coverslip, to minimize unwanted reflections of the laser. The light back-scattered by the particle is collected by the objective, redirected by a BS, focused by a tube lens and integrated by a camera. The back-scattered power is directly proportional to the local intensity of the strongly focused beam at the particle’s position.

NA = 1.4). We use a gold nanoparticle (NP) to probe the local intensity of the strongly focused beam. The particle is mounted on a coverslip, which we can freely move in the transverse plane (through a 2D piezo-stage) and along the optical axis (using a stepper motor). We use index-matched oil (between the objective and the coverslip, and on top of the coverslip) to minimize reflections. The only back-reflected light is therefore caused by NP scattering. Finally, the collected light is redirected by a BS, focused by a tube lens and imaged with a camera. Integrating over the pixels of the camera, we obtain a measurement of the scattered power. Importantly, the power of the back-scattered light is proportional to the local intensity of the field at the particle’s position. Therefore, employing the piezo-stage and the stepper motor to raster scan the focal area, we reconstruct the three-dimensional focal intensity, with a resolution limited by the NP size (100 nm in our case). The experimental setup described above is sketched in Fig. A.9.

In Fig. A.10, we show as an example the 3D reconstruction of a linearly polarized gaussian beam (note that we used an objective with NA = 1.3 in this case). The full width at half maximum corresponds to  $0.3336 \mu\text{m}$  along  $x$  and  $0.3636 \mu\text{m}$  along  $y$ . This value deviates from the theoretical one [ $\lambda/(2\text{NA}) = 0.2435$ ] by  $\approx 40\%$ , which is in line with what reported in literature [148].

Considering the distribution along  $z$ , we recognize two lobes appearing at negative  $z$  values, and a smearing in the opposite direction. This effect is well known and is caused by spherical aberrations introduced by the objective [149].

### A.3 Results: towards a 3DQ intensity

In this section, we show the results achieved so far towards the realization of a 3DQ focus. In Fig. A.2 we have already shown the field that we need to generate in order to experimentally realize the 3DQ intensity. Using the generation setup described in Sec. A.2.1, we can program the desired field distribution in the back focal plane of the high-NA objective. We show in Fig. A.11 the simulations and measurements of the generated intensity distribution when

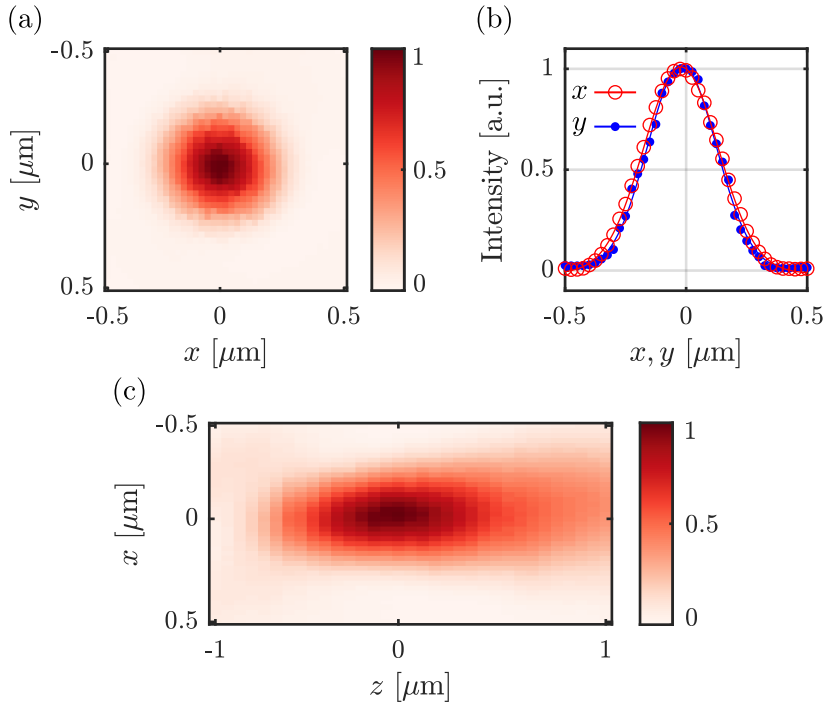


**Figure A.10:** Focus reconstruction of a strongly focused linearly polarized Gaussian beam. (a) Intensity distribution in the  $xy$ -plane ( $z=0$ , i.e., focal plane). (b) Intensity cross-sections at the center of the focus. (c) Intensity distribution in the  $xz$ - plane ( $y=0$ );

filtered by a horizontally (Fig. A.11a and Fig. A.11c) or vertically (Fig. A.11b and Fig. A.11d) oriented linear polarizer. The measurements are performed by the camera in Fig. A.3.

After characterizing the field distribution in the back focal plane of the objective, we moved to the reconstruction of the focal intensity. To address the task in incremental steps, we first characterized the focus of a field modulated only by the first SLM, i.e., with programmed amplitude and phase distributions, but linear polarization. In particular, we programmed a field with amplitude  $A$  given by  $A = \sqrt{|E_x|^2 + |E_y|^2}$ , where  $E_x$  and  $E_y$  are the distributions showed in Fig. A.2, and the phase of the  $E_x$  component. We chose this combination of amplitude and phase because it results in a peculiar intensity shape in the focal plane, as reported from simulation in Fig. A.12a. The reconstructed intensity (Fig. A.12b) is in good agreement with the simulated distribution. This promising result shows the control achieved over the focal intensity distribution. In the next section, we will discuss the experimental steps that we plan in order to include the polarization distribution in the paraxial field to obtain the 3DQ focus.

## A.4 Outlook: including polarization

The next step towards the measurement of the 3DQ focus is to include the polarization distribution in the paraxial field. To this aim, we propose the following experimental steps:

- we independently generate the radially polarized (RP) and the azimuthally polarized (AP) components of the paraxial beam (see Fig. A.2), and we confirm that the intensity distributions in the focal plane correspond to the simulated ones (Figs. A.1c and A.1d);
- next, we generate the superposition of the RP and AP components, controlling their relative weight to obtain a flat-top intensity (Fig. A.1e). This experimental approach allows us to compensate for eventual non-idealities (e.g., lower effective NA) that modify the relative strength of the two components;
- we then optimize the amplitude and phase distributions of the RP component to obtain the quartic intensity along the optical axis (Fig. A.1a). Next, we adjust the weight of the AP component accordingly to achieve the quartic intensity in the focal plane. Finally, this would lead to the generation of a 3DQ intensity distribution.

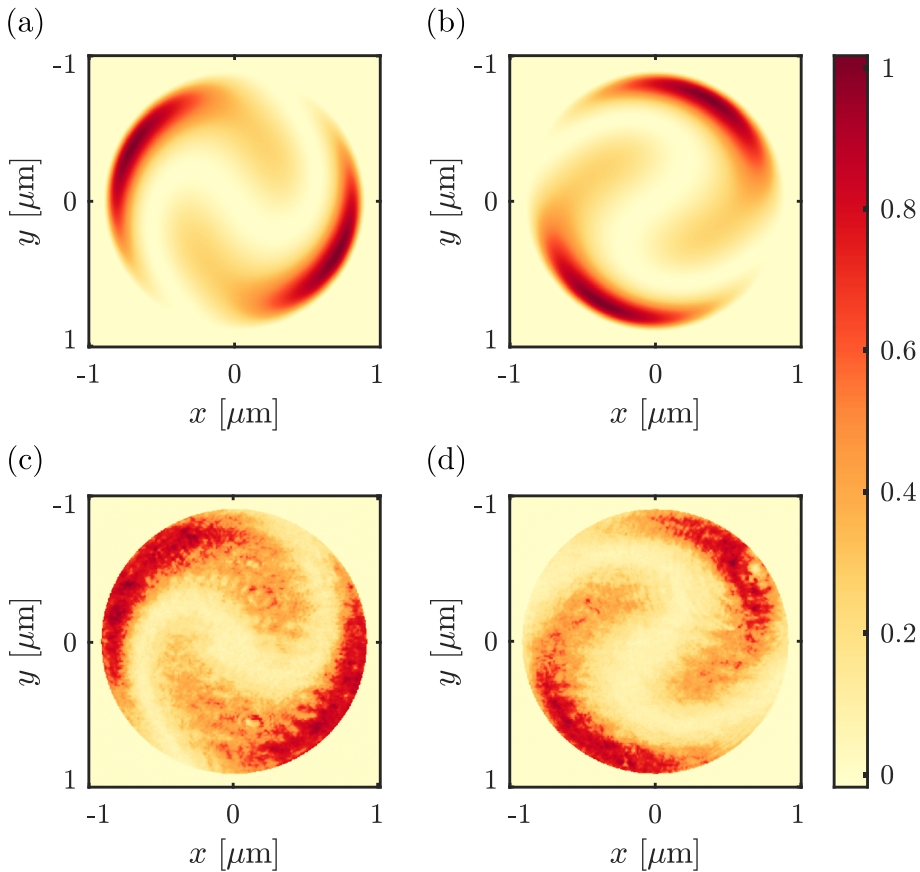


**Figure A.11:** Paraxial beam generation. (a,b) Simulation of the intensity of the (a) horizontally and (b) vertically polarized components. (c,d) Measurement of the generated intensity when filtered with a (c) horizontally and (d) vertically oriented linear polarizer.

## A.5 Conclusion

A three-dimensional quartic intensity is given by an intensity distribution with zero-curvature along the three Cartesian axis in the focal space. In this chapter, we presented a recipe to obtain a 3DQ intensity, that relies on the generation of the superposition of azimuthally and radially polarized fields in the back focal plane of a high-NA objective. We then showed that we are able to generate a desired complex vector field distribution in a given plane employing a system of two SLMs. We use it to generate a paraxial beam that, when strongly focused,

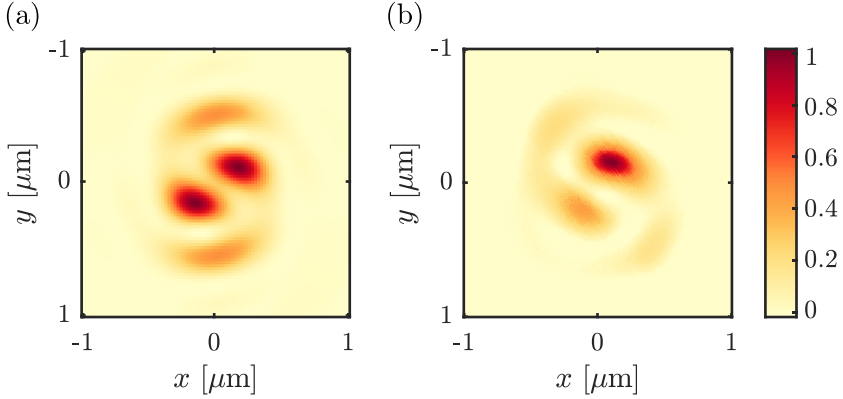


**Figure A.12:** Intensity distribution in the focal plane for a linearly polarized paraxial field, with amplitude  $A = \sqrt{|E_x|^2 + |E_y|^2}$  and phase  $\phi = \angle(E_x)$ , where  $E_x = |E_x|\exp(i\angle(E_x))$  and  $E_y$  are the  $x$  and  $y$  polarized components depicted in Fig. A.2. (a) Simulated and (b) measured intensity distributions.

results in the 3DQ intensity. Using a gold nanoparticle, we were able to probe the local intensity, and reconstruct the three dimensional distribution around the focus. As a benchmark, we reconstructed the three-dimensional focus of a linearly polarized Gaussian beam. Moreover, to prove our system capability, we measured the focus of a linearly polarized beam with the same amplitude distribution as the 3DQ paraxial field, and the phase distribution of the  $x$  component of the paraxial beam. Finally, we presented the experimental steps planned to include the polarization distribution and achieve the 3DQ intensity.

In conclusion, we presented a setup which is able to generate a desired complex vector field at a given plane, and a microscope system capable of reconstructing the 3D intensity distribution in the focal space. We plan to use it to generate a 3DQ intensity, which would provide an interesting tool for applications in laser cutting [132], trapping of levitated nanoparticles [135], and Bose-Einstein condensation [136].

# B

## Supplementary information

### B.1 Unitarity of a linear transformation and overall coherence

Let us consider a set of normalized input fields  $\mathbf{F}_{\text{in}}$ , characterized by a coherence matrix  $\mathbb{K}_{\text{in}} = \langle \mathbf{F}_{\text{in}} \mathbf{F}_{\text{in}}^\dagger \rangle$ . We apply a unitary transformation  $\hat{U}$  to get the set of output fields  $\mathbf{F}_{\text{out}} = \hat{U} \mathbf{F}_{\text{in}}$ , with coherence matrix  $\mathbb{K}_{\text{out}} = \langle \mathbf{F}_{\text{out}} \mathbf{F}_{\text{out}}^\dagger \rangle$ . By definition, the unitary transformation  $\hat{U}$  satisfies the relation  $\hat{U} \hat{U}^\dagger = \hat{U}^\dagger \hat{U} = \mathbb{I}$ .

We can demonstrate that the overall coherence  $\mathcal{S}$ , defined in Eq. (2.35), is invariant under unitary transformations. To prove it, we expand the traces

$$\text{tr}(\mathbb{K}_{\text{out}}^2) = \text{tr}(\langle \mathbf{F}_{\text{out}} \mathbf{F}_{\text{out}}^\dagger \rangle^2) = \text{tr} \left[ \left( \hat{U} \langle \mathbf{F}_{\text{in}} \mathbf{F}_{\text{in}}^\dagger \rangle \hat{U}^\dagger \right)^2 \right] = \text{tr} \left[ \left( \hat{U} \mathbb{K}_{\text{in}} \hat{U}^\dagger \right)^2 \right], \quad (\text{B.1})$$

$$\text{tr}(\mathbb{K}_{\text{out}}) = \text{tr}(\langle \mathbf{F}_{\text{out}} \mathbf{F}_{\text{out}}^\dagger \rangle) = \text{tr} \left[ \hat{U} \langle \mathbf{F}_{\text{in}} \mathbf{F}_{\text{in}}^\dagger \rangle \hat{U}^\dagger \right] = \text{tr} \left[ \hat{U} \mathbb{K}_{\text{in}} \hat{U}^\dagger \right], \quad (\text{B.2})$$

and, using the definition of unitarity of the transformation and the cyclic property of the trace, we obtain

$$\text{tr}(\mathbb{K}_{\text{out}}^2) = \text{tr} \left( \hat{U} \mathbb{K}_{\text{in}} \hat{U}^\dagger \hat{U} \mathbb{K}_{\text{in}} \hat{U}^\dagger \right) = \text{tr} \left( \mathbb{K}_{\text{in}} \hat{U}^\dagger \hat{U} \mathbb{K}_{\text{in}} \hat{U}^\dagger \hat{U} \right) = \text{tr}(\mathbb{K}_{\text{in}}^2). \quad (\text{B.3})$$

---

This appendix is based on the supplemental documents of the articles: A. Nardi *et al.*, Opt. Express 29, 40831-40840 (2021), and A. Nardi *et al.*, Opt. Lett. 47, 4588-4591 (2022).

$$\text{tr}(\mathbb{K}_{\text{out}}) = \text{tr}(\hat{U}\mathbb{K}_{\text{in}}\hat{U}^\dagger) = \text{tr}(\mathbb{K}_{\text{in}}\hat{U}^\dagger\hat{U}) = \text{tr}(\mathbb{K}_{\text{in}}). \quad (\text{B.4})$$

We proved that  $\text{tr}(\mathbb{K}_{\text{out}}^2) = \text{tr}(\mathbb{K}_{\text{in}}^2)$  and  $\text{tr}(\mathbb{K}_{\text{out}}) = \text{tr}(\mathbb{K}_{\text{in}})$ , thus confirming that the overall coherence remains unaffected under unitary transformations.

## B.2 Detected signal variance without added noise

In this appendix, we derive the expression of the variance of the detected signal in mutual coherence coding. We highlight that the variance considered here results from the stochastic nature of the mutual coherence: no noise is added to the transmitted fields in this treatment. Let us consider the interference experiment between a single pair of fields  $Y_i$  and  $Y_j$ . The signal  $S_{ij}$  measured by the balanced photodetector is [see Eq. (3.31)]

$$S_{ij} = \frac{2}{T(N_f - 1)} \int_{-T/2}^{T/2} \text{Re}(Y_i Y_j^*) dt, \quad (\text{B.5})$$

where  $T$  is the integration time of the detector, and  $N_f$  is the number of transmitted fields. The fields are stochastic variables, hence we characterize the signal through its expectation value and its variance. The expectation value, denoted with an overline, is

$$\overline{S_{ij}} = \frac{2}{T(N_f - 1)} \int_{-T/2}^{T/2} \text{Re}(\overline{Y_i Y_j^*}) dt = \frac{2P_{\text{out}}}{N_f - 1} \text{Re}(\gamma_{ij}), \quad (\text{B.6})$$

where we used the relation  $P_{\text{out}}\gamma_{ij} = \overline{Y_i Y_j^*}$ . To derive the variance  $\text{Var}(S_{ij}) = \overline{S_{ij}^2} - (\overline{S_{ij}})^2$ , we compute the second moment

$$\begin{aligned} \overline{S_{ij}^2} &= \frac{1}{T^2(N_f - 1)^2} \iint_{-T/2}^{T/2} \overline{\left[ Y_i(t_1) Y_j^*(t_1) + c.c. \right] \left[ Y_i(t_2) Y_j^*(t_2) + c.c. \right]} dt_1 dt_2 \\ &= \frac{2}{T^2(N_f - 1)^2} \iint_{-T/2}^{T/2} \text{Re} \left\{ \overbrace{\left[ Y_i(t_1) Y_j^*(t_1) + c.c. \right] Y_i(t_2) Y_j^*(t_2)}^{\mathcal{I}} \right\} dt_1 dt_2, \end{aligned} \quad (\text{B.7})$$

where *c.c.* stands for complex conjugate. Recalling that the input fields  $X_n$ , with  $n \in \{1, 2, \dots, N_f\}$ , are related to the outputs of the linear port through the

relation  $Y_i = \sum_n^{N_f} t_{in} X_n$ , we can express  $\mathcal{S}$  as:

$$\begin{aligned} \mathcal{S} &= \overline{\left[ Y_i(t_1) Y_j^*(t_1) + Y_i^*(t_1) Y_j(t_1) \right] Y_i(t_2) Y_j^*(t_2)} \\ &= \sum_{n,m,p,q}^{N_f} \left( t_{jn}^* t_{im} + t_{in}^* t_{jm} \right) t_{jp}^* t_{iq} \overline{X_n^*(t_1) X_m(t_1) X_p^*(t_2) X_q(t_2)}. \end{aligned} \quad (\text{B.8})$$

To simplify this equation, we need to derive the expression for the second-order correlation function  $\Gamma$  of the input fields, i.e.,

$$\Gamma_{nmpq}(t_1 - t_2) = \overline{X_n^*(t_1) X_m(t_1) X_p^*(t_2) X_q(t_2)}. \quad (\text{B.9})$$

The input fields are independent and have a null expectation value, hence  $\Gamma_{nmpq}(t_1 - t_2)$  is non-zero only if the values of the indexes are all equal, or equal in pairs. Therefore, only for the following four, mutually exclusive cases, the expression does not vanish. Firstly, if  $n = m \neq p = q$ , we have

$$\Gamma_{nnpp}(t_1 - t_2) = \overline{|X_n(t_1)|^2 |X_p(t_2)|^2} = P_{\text{in}}^2. \quad (\text{B.10})$$

Secondly, if  $n = q \neq m = p$ , we have

$$\Gamma_{nmmn}(t_1 - t_2) = \overline{X_n^*(t_1) X_n(t_2) X_m(t_1) X_m^*(t_2)}. \quad (\text{B.11})$$

To solve this equation, we use the degree of first-order coherence  $g^{(1)}$  (see Sec. 2.1.1):

$$g^{(1)}(t_1 - t_2) = \frac{\overline{X_n^*(t_1) X_n(t_2)}}{P_{\text{in}}}. \quad (\text{B.12})$$

We can consider the process stationary, hence not dependent on the particular value of  $t_1$  and  $t_2$ , but only on their difference  $\tau = t_1 - t_2$ . For Lorentzian power spectral density, the expression of  $g^{(1)}(\tau)$  is [see Eq. (2.13)]

$$g^{(1)}(\tau) = \exp\left(-i2\pi\nu_0\tau - 2\pi\Delta\nu|\tau|\right), \quad (\text{B.13})$$

where  $\nu_0$  and  $\Delta\nu$  are the central frequency and the linewidth of the input light fields, respectively. Thus,  $\Gamma_{nmmn}$  takes the form

$$\Gamma_{nmmn}(\tau) = P_{\text{in}}^2 |g^{(1)}(\tau)|^2. \quad (\text{B.14})$$

Thirdly, if  $n = p \neq m = q$ , we have

$$\Gamma_{nppn}(t_1 - t_2) = \overline{X_n^*(t_1) X_n^*(t_2) X_p(t_1) X_p(t_2)} = 0. \quad (\text{B.15})$$



Finally, we have for  $n = m = p = q$

$$\Gamma_{nnnn}(t_1 - t_2) = \overline{X_n^*(t_1)X_n(t_1)X_n^*(t_2)X_n(t_2)} = P_{\text{in}}^2 g^{(2)}(\tau), \quad (\text{B.16})$$

where we introduced the degree of second-order coherence  $g^{(2)}(\tau)$ . With classical chaotic light sources we have [150]

$$g^{(2)}(\tau) = 1 + |g^{(1)}(\tau)|^2, \quad (\text{B.17})$$

which allows us to join the four cases into a single expression:

$$\Gamma_{nmpq}(\tau) = P_{\text{in}}^2 [\delta_{nm}\delta_{pq} + \delta_{nq}\delta_{mp}|g^{(1)}(\tau)|^2]. \quad (\text{B.18})$$

Going back to the integral  $\mathcal{S}$  of Eq. (B.8) we get

$$\mathcal{S} = P_{\text{in}}^2 \sum_{n,p}^{N_f} \left[ \left( t_{jn}^* t_{in} + t_{in}^* t_{jn} \right) t_{jp}^* t_{ip} + \left( t_{jn}^* t_{ip} + t_{in}^* t_{jp} \right) t_{jp}^* t_{in} |g^{(1)}(\tau)|^2 \right]. \quad (\text{B.19})$$

From our choice of the linear port, we have  $P_{\text{out}}\gamma_{ij} = P_{\text{in}}\sum_n^{N_f} t_{in}t_{jn}^*$  [see Eq. (3.29)], leading to

$$\mathcal{S} = P_{\text{out}}^2 \left[ \left( \gamma_{ij} + \gamma_{ij}^* \right) \gamma_{ij} + \left( \gamma_{ij}^2 + \gamma_{ii}\gamma_{jj} \right) |g^{(1)}(\tau)|^2 \right]. \quad (\text{B.20})$$

Including the derived expression of  $\mathcal{S}$  in the second moment of the signal and recalling that  $\gamma_{ii} = 1$  we get

$$\overline{S_{ij}^2} = \frac{4P_{\text{out}}^2 \text{Re}(\gamma_{ij})^2}{(N_f - 1)^2} + \frac{2P_{\text{out}}^2 \left[ 1 + \text{Re}(\gamma_{ij}^2) \right]}{T(N_f - 1)^2} \int_{-T/2}^{T/2} |g^{(1)}(\tau)|^2 d\tau. \quad (\text{B.21})$$

The integral can be analytically solved from the definition of  $g^{(1)}(\tau)$  given in Eq. (B.13):

$$\int_{-T/2}^{T/2} |g^{(1)}(\tau)|^2 d\tau = \frac{1 - \exp(-2\pi\Delta\nu T)}{2\pi\Delta\nu} \rightarrow \frac{1}{2\pi\Delta\nu} \quad (\text{B.22})$$

where we considered the limit of integration time  $T$  much longer than the coherence time  $\tau_c = 1/(2\pi\Delta\nu)$  of the light sources. Finally, the variance of the signal is

$$\text{Var}(S_{ij}) = \frac{2P_{\text{out}}^2 \left[ 1 + \text{Re}(\gamma_{ij}^2) \right]}{(N_f - 1)^2 2\pi\Delta\nu T}. \quad (\text{B.23})$$

### B.3 Signal-to-noise ratio (SNR) derivation

In this section, we derive the expression of the SNR, defined as

$$\text{SNR} = \frac{\overline{\tilde{S}_{ij}}^2}{\text{Var}(\tilde{S}_{ij})}, \quad (\text{B.24})$$

where  $i \neq j$  and  $\tilde{S}_{ij}$  is the signal measured by the balanced detector. Differently than Sec. B.2, we consider here the presence of noise  $N_i$  (hence the different symbol  $\tilde{S}_{ij}$ ), which is added to the received signal  $\tilde{Y}_i = Y_i + N_i$ . Noise related to different signals are uncorrelated, i.e.,  $\overline{N_i N_j^*} = 0$ , with  $i \neq j$ , they are stationary and all characterized by zero mean value and an autocorrelation  $\mathcal{R}_N(\tau) = \overline{N_i(t)^* N_i(t + \tau)} = P_N \exp(-2\pi \Delta \nu_N |\tau|)$ , where  $\Delta \nu_N$  is the cut-off frequency of the transmission channel, and  $P_N$  is the noise power.

The expectation value of the detected signal in the presence of noise is

$$\overline{\tilde{S}_{ij}} = \int_{-T/2}^{T/2} \frac{2 \text{Re}(\tilde{Y}_i \tilde{Y}_j^*)}{T(N_f - 1)} dt = \int_{-T/2}^{T/2} \frac{2 \text{Re}(\overline{Y_i Y_j^*} + \overline{Y_i N_j^*} + \overline{N_i Y_j^*} + \overline{N_i N_j^*})}{T(N_f - 1)} dt. \quad (\text{B.25})$$

Since the noise and the signals are uncorrelated ( $\overline{Y_i N_j^*} = \overline{N_i Y_j^*} = 0$ ) and we know that  $\overline{N_i N_j^*} = 0$ , the expression simplifies to

$$\overline{\tilde{S}_{ij}} = \frac{2P_{\text{out}} \text{Re}(\gamma_{ij})}{T(N_f - 1)}, \quad (\text{B.26})$$

which is the same expression obtained without the noise [see Eq. (B.6)].

As for the second moment of the detected signal, we have

$$\overline{\tilde{S}_{ij}^2} = \frac{2}{T^2(N_f - 1)^2} \int_{T^2} \text{Re} \left\{ \overbrace{[\tilde{Y}_i^*(t_1) \tilde{Y}_j(t_1) + c.c.] \tilde{Y}_i^*(t_2) \tilde{Y}_j(t_2)}^{\tilde{\mathcal{I}}} \right\} dt_1 dt_2. \quad (\text{B.27})$$

We can analyze the two terms of  $\tilde{\mathcal{I}}$  separately:

$$\tilde{\mathcal{I}} = \overbrace{\tilde{Y}_i^*(t_1) \tilde{Y}_j(t_1) \tilde{Y}_i^*(t_2) \tilde{Y}_j(t_2)}^{\eta_1} + \overbrace{\tilde{Y}_i(t_1) \tilde{Y}_j^*(t_1) \tilde{Y}_i^*(t_2) \tilde{Y}_j(t_2)}^{\eta_2}. \quad (\text{B.28})$$

Of the 16 terms obtained expanding the product in  $\eta_1$ , the only non-zero term is

$$\eta_1 = \overline{Y_i^*(t_1) Y_j(t_1) Y_i^*(t_2) Y_j(t_2)} = \sum_{n,m,p,q}^N t_{in}^* t_{jm} t_{ip}^* t_{jq} \Gamma_{nmpq}(t_1 - t_2), \quad (\text{B.29})$$

where we used the definition of the linear port  $Y_i = \sum_{n=1}^{N_f} t_{in} X_n$  and the definition of  $\Gamma_{nmpq}(t_1 - t_2)$  given in Eq. (B.9). Using the expression derived in Eq. (B.18) we get

$$\eta_1 = P_{\text{out}}^2 \gamma_{ij}^2 (1 + |g^{(1)}(\tau)|^2). \quad (\text{B.30})$$

For  $\eta_2$ , instead, more terms are non-zero:

$$\begin{aligned} \eta_2 = & \sum_{n,m,p,q}^{N_f} t_{jn}^* t_{im} t_{ip}^* t_{jq} \Gamma_{nmpq}(t_1 - t_2) + |\mathcal{R}_N(\tau)|^2 + \\ & + \sum_{n,m}^{N_f} t_{in} t_{im}^* \overline{X_n(t_1) X_m^*(t_2)} \mathcal{R}(-\tau) + \sum_{n,m}^{N_f} t_{jn}^* t_{jm} \overline{X_n^*(t_1) X_m(t_2)} \mathcal{R}(\tau), \end{aligned} \quad (\text{B.31})$$

where  $\tau = t_1 - t_2$ . Using again Eq. (B.18) and considering that  $\gamma_{ii} = \gamma_{jj} = 1$  we obtain

$$\eta_2 = P_{\text{out}}^2 [|\gamma_{ij}|^2 + |g^{(1)}(\tau)|^2] + |\mathcal{R}_N(\tau)|^2 + P_{\text{out}} \text{Re} [g^{(1)}(\tau) \mathcal{R}_N(-\tau)]. \quad (\text{B.32})$$

To solve the integral we need the following relations:

$$\frac{1}{T} \int_{-T/2}^{T/2} |g^{(1)}(\tau)|^2 d\tau = \frac{1 - \exp(-2\pi\Delta\nu T)}{2\pi\Delta\nu T} \approx \frac{1}{2\pi\Delta\nu T}, \quad (\text{B.33})$$

$$\frac{1}{T} \int_{-T/2}^{T/2} |\mathcal{R}_N(\tau)|^2 d\tau = \frac{P_N^2 [1 - \exp(-2\pi\Delta\nu_N T)]}{2\pi\Delta\nu_N T} \approx \frac{P_N^2}{2\pi\Delta\nu_N T}, \quad (\text{B.34})$$

$$\frac{1}{T} \int_{-T/2}^{T/2} \text{Re} \{g^{(1)}(\tau) \mathcal{R}_N(-\tau)\} d\tau \approx \frac{P_N(\Delta\nu + \Delta\nu_N)}{2\pi T [(\Delta\nu + \Delta\nu_N)^2 + \nu_0^2]} \rightarrow 0. \quad (\text{B.35})$$

The approximate result comes from considering  $T \gg 1/\Delta\nu$ ,  $T \gg 1/\Delta\nu_N$  and  $\nu_0 \gg \Delta\nu, \Delta\nu_N$ . Therefore, going back to the expression of the second moment with the approximate results of the integrals we get

$$\overline{\tilde{S}_{ij}^2} = \frac{2P_{\text{out}}^2}{(N_f - 1)^2} \left[ \text{Re}(\gamma_{ij}^2) + |\gamma_{ij}|^2 + \frac{1 + \text{Re}(\gamma_{ij}^2)}{2\pi\Delta\nu T} + \frac{P_N^2}{P_{\text{out}}^2 2\pi\Delta\nu_N T} \right]. \quad (\text{B.36})$$

Considering that  $|\gamma_{ij}|^2 + \text{Re}(\gamma_{ij}^2) = 2\text{Re}(\gamma_{ij})^2$ , we finally derive the variance of the detected signal:

$$\text{Var}(\tilde{S}_{ij}) = \overline{\tilde{S}_{ij}^2} - (\overline{\tilde{S}_{ij}})^2 = \frac{2P_{\text{out}}^2}{(N_f - 1)^2} \left[ \frac{1 + \text{Re}(\gamma_{ij}^2)}{2\pi\Delta\nu T} + \frac{P_N^2}{P_{\text{out}}^2 2\pi\Delta\nu_N T} \right]. \quad (\text{B.37})$$

Finally, the expression of the SNR is the following

$$\text{SNR} = \frac{\overline{\tilde{S}_{ij}}^2}{\text{Var}(\tilde{S}_{ij})} = \left[ \frac{1 + \text{Re}(\gamma_{ij}^2)}{2\text{Re}(\gamma_{ij}^2)} \frac{1}{2\pi\Delta\nu T} + \frac{P_N^2}{2P_{\text{out}}^2 \text{Re}(\gamma_{ij}^2)} \frac{1}{2\pi\Delta\nu_N T} \right]^{-1}. \quad (\text{B.38})$$

In case we choose to consider only shot noise, the power spectral density for a balanced detector is  $\mathcal{S}_{NN} = P_N^2 / \Delta\nu_N = 2h\nu_0 P_{\text{out}}$ . Moreover, considering a transmission efficiency  $P_{\text{out}} / P_{\text{in}} = \eta$ , the final expression of the SNR is

$$\text{SNR} = \left[ \frac{1 + \text{Re}(\gamma_{ij}^2)}{2\text{Re}(\gamma_{ij}^2)} \frac{1}{2\pi\Delta\nu T} + \frac{h\nu_0}{\eta P_{\text{in}} \text{Re}(\gamma_{ij}^2)} \frac{1}{2\pi T} \right]^{-1}. \quad (\text{B.39})$$

## B.4 Technical limitations

In Sec. 4.2.3, we have seen that we encounter deviations between the encoded and the reconstructed degree of coherence when we try to achieve very low (approaching 0) or very high (approaching 1) values. In this section, we provide more details on the origins of these limits.

Let us start investigating the case where we want to obtain mutually incoherent outputs. According to Eq. (2.40), the linear transformation we want to apply is the identity matrix, i.e., the inputs should be transmitted to the outputs unaffected. However, since it is not feasible to control all the modes supported by the scattering medium (see Sec. 4.1.1), the beams get mixed during the propagation through the medium. The resulting background noise is responsible for an unwanted contribution of each input field to every output.

We will now quantify the limitations to the minimum degree of coherence imposed by the background noise. We start considering a coherence matrix  $\mathbb{K}_{\text{out}}$  of the form

$$\mathbb{K}_{\text{out}} = \begin{bmatrix} 1 & \gamma & \cdots & \gamma \\ \gamma & 1 & \cdots & \gamma \\ \vdots & \ddots & \ddots & \vdots \\ \gamma & \gamma & \cdots & 1 \end{bmatrix}, \quad (\text{B.40})$$

where, for simplicity, we set the off-diagonal terms to have the same constant real value  $\gamma$ . To have mutually incoherent output fields, we want  $\gamma$  to tend to 0. From  $\mathbb{K}_{\text{out}}$  we extract the expression of the linear transformation  $\hat{T}$  [Eq. (2.40)], which connects the mutually incoherent input fields  $\mathbf{E}_{\text{in}}$  to the output fields  $\mathbf{E}_{\text{out}}$  with coherence matrix  $\mathbb{K}_{\text{out}}$ . From the expression of  $\mathbb{K}_{\text{out}}$  in Eq. (B.40), the linear transformation  $\hat{T}$  can be completely described by two coefficients:

$t_{11}$  for the diagonal terms, which are all equal, and  $t_{21}$  for the off-diagonal elements, which are again all equal. Note that the coefficients  $t_{11}$  and  $t_{21}$  associate the two outputs  $E_1^{\text{out}}$  and  $E_2^{\text{out}}$  with the single input  $E_1^{\text{in}}$ , according to the relations  $E_1^{\text{out}} = t_{11}E_1^{\text{in}}$ , and  $E_2^{\text{out}} = t_{21}E_1^{\text{in}}$ . Ideally, we would like  $|t_{21}|$  to approach zero to get zero output degree of coherence, i.e., we want  $|E_2^{\text{out}}| = 0$ . In practice, the background noise in the output intensity pattern poses a lower bound to the intensity  $|E_2^{\text{out}}|^2$ , hence to  $|t_{21}|$ , which finally sets the minimum degree of coherence different from zero. In Fig. B.1a, we show the scaling of the absolute value of the ratio  $|t_{21}/t_{11}|$  as a function of the degree of coherence  $\gamma$ . If we increase the number of inputs, i.e., the dimensionality of  $\mathbb{K}_{\text{out}}$ , the requirement is very similar (Fig. B.1). A desired minimum degree of coherence translates into a minimum signal-to-noise ratio (SNR). In fact, considering the single input  $E_1^{\text{in}}$  and assuming that the only contribution to  $E_2^{\text{out}}$  is given by the background noise,  $|t_{11}|^2$  is the maximum generated intensity and  $|t_{21}|^2$  is the noise intensity, thus the SNR is defined as  $|t_{11}|^2/|t_{21}|^2$ . In Fig. B.1b, we show that low coherence values demand very high SNR, which is limited by the number of SLM pixels modulating each input laser [109]. We expect a similar argument to work for a coherence matrix  $\mathbb{K}_{\text{out}}$  where the off-diagonal terms assume various values. Following the reasoning described above, the limitation would be given by the coefficient of the linear port  $\hat{T} = \sqrt{\mathbb{K}}$  with the minimum absolute value, which requires a high enough SNR to be implemented. Note that this conclusion is the result of a numerical analysis, since we do not have a general analytical expression for  $\hat{T}$ .

Let us now consider the factors limiting the maximum degree of coherence.

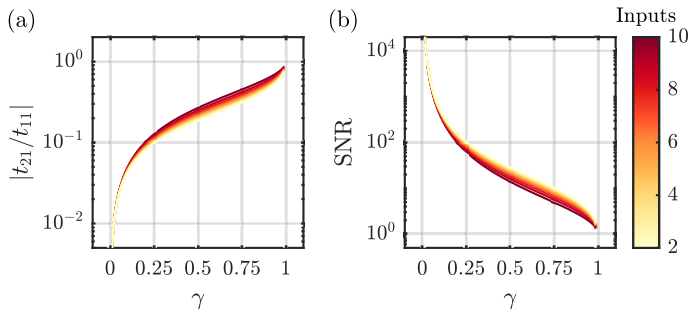


**Figure B.1:** Minimum degree of coherence limitations. (a) Given two outputs  $E_1^{\text{out}} = t_{11}E_1^{\text{in}}$  and  $E_2^{\text{out}} = t_{21}E_1^{\text{in}}$ , the degree of coherence  $\gamma$  depends on the ratio  $|t_{21}/t_{11}|$ . (b) Minimum signal-to-noise ratio (SNR) needed to encode the degree of coherence  $\gamma$ . In the case that  $|t_{21}|$  is only given by the background noise, the SNR is  $|t_{11}|^2/|t_{21}|^2$ .

To investigate this case, we turn on a single input ( $E_1^{\text{in}}$ ), and we consider a single pair of output fields  $E_1^{\text{out}}$  and  $E_2^{\text{out}}$ , which are related to the input by the coefficients  $t_{11}$  and  $t_{21}$ , as discussed above. We compute the mutual degree of coherence

$$\gamma = \frac{\langle E_1^{\text{out}}(E_2^{\text{out}})^* \rangle}{\sqrt{\langle |E_1^{\text{out}}|^2 \rangle \langle |E_2^{\text{out}}|^2 \rangle}} = \frac{t_{11} t_{21}^* \langle |E_1^{\text{in}}|^2 \rangle}{|t_{11} t_{21}| \langle |E_1^{\text{in}}|^2 \rangle} = \frac{t_{11} t_{21}^*}{|t_{11} t_{21}|}, \quad (\text{B.41})$$

whose modulus  $|\gamma|$  is always equal to 1, regardless the values of the transformation coefficients. Nevertheless, the measurements deviate from this ideal result. To show it, we use a single input laser to generate through our system two output beams. We then let the output beams interfere and we reconstruct the degree of coherence. We report the measured interference patterns for two different input lasers in Fig. B.2a and Fig. B.2b. The reconstructed degrees of coherence ( $\gamma_1 = 0.86$  for the first input and  $\gamma_1 = 0.92$  for the second) are lower than the ideal value of 1. This discrepancy, in line with what is reported in literature, is associated to the limited spatial coherence of the light source [151]. We show now that the maximum degree of coherence achievable with a single laser is limiting the value obtainable by the whole system. Let us consider two mutually incoherent inputs, both of them contributing to two output fields. Since the components from the different inputs do not interfere, the resulting interference pattern is given by the sum of the individual patterns. Thus, we can write the visibility in terms of the maximum  $I_1^{\text{max}}$ ,  $I_2^{\text{max}}$  and minimum  $I_1^{\text{min}}$ ,  $I_2^{\text{min}}$  intensity given by the contributions from the two different inputs:

$$\mathcal{V} = \frac{(I_1^{\text{max}} + I_2^{\text{max}}) - (I_1^{\text{min}} + I_2^{\text{min}})}{(I_1^{\text{max}} + I_2^{\text{max}}) + (I_1^{\text{min}} + I_2^{\text{min}})}. \quad (\text{B.42})$$

After few algebraic passages, we get

$$\mathcal{V} = \frac{\mathcal{V}_1}{1 + \frac{(I_2^{\text{max}} + I_2^{\text{min}})}{(I_1^{\text{max}} + I_1^{\text{min}})}} + \frac{\mathcal{V}_2}{1 + \frac{(I_1^{\text{max}} + I_1^{\text{min}})}{(I_2^{\text{max}} + I_2^{\text{min}})}}, \quad (\text{B.43})$$

where  $\mathcal{V}_i = (I_i^{\text{max}} - I_i^{\text{min}})/(I_i^{\text{max}} + I_i^{\text{min}})$  is the visibility of the interference pattern given by the  $i$ th input. Considering  $I_1^{\text{max}} = I_2^{\text{max}}$  and  $I_{1,2}^{\text{max}} \gg I_{1,2}^{\text{min}}$ , we obtain

$$\mathcal{V} \approx \frac{\mathcal{V}_1 + \mathcal{V}_2}{2}. \quad (\text{B.44})$$

The last equation tells us that the maximum visibility obtainable by the whole system [directly linked to the degree of coherence, see Eq. (4.11)] is limited by

the average visibility over each single input. Therefore, the maximum degree of coherence achievable is limited by the spatial coherence of the light sources. Figure B.2 shows the interference pattern when we turn on: (a) only the first input, (b) only the second one, or (c) both of them. The measured degrees of coherence resulting from the combination of the two inputs ( $\gamma_{12} = 0.89$ ) is in agreement with Eq. (B.44).

## B.5 Mutual incoherence of the input fields

Our implementation relies on mutually incoherent inputs. To achieve this condition, we used three red lasers (Thorlabs HRP050 and Meredith Instruments 633 nm HeNe lasers, and  $\approx 650$  nm pen-type visual fault locator FOSCO BOB-VFL650-10), with a linewidth (HeNe  $\approx 10$  MHz, VFL  $\approx 1$  THz) much larger than the bandwidth of the employed detector (Basler acA640-750um, bandwidth  $\approx 10 \div 100$  Hz). This ensures that we can consider them mutually incoherent. To confirm it, we focused the three laser beams into a single spot, checking that no interference fringes are visible (see Fig. B.3).

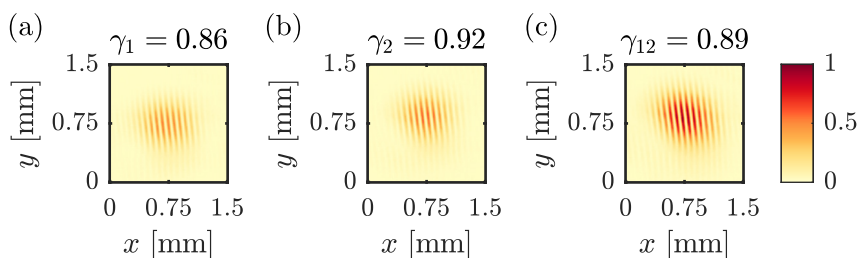


**Figure B.2:** Interference patterns. We have two interfering output fields, resulting from the superposition of two inputs. We show the interference patterns when (a) the first, (b) the second or (c) both inputs contribute to the outputs. Each case is associated to a measured degree of coherence  $\gamma_i$ , where the subscript  $i$  indicates the contributing inputs.

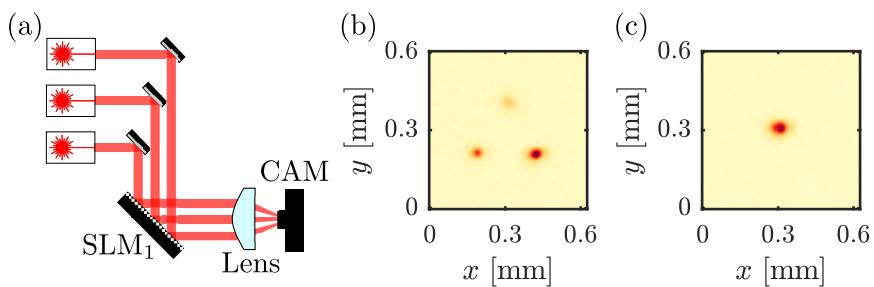


**Figure B.3:** Mutually incoherent inputs. (a) Characterization setup. Three independent laser beams are modulated by a SLM before being focused onto a camera. (b, c) Camera images. The SLM is used to (b) separate the beams in the focal plane or to (c) focus them in the same point. No interference fringes are present when the beams overlap, confirming that the three fields are mutually incoherent.





---

## References

- [1] Retrieved November 11, 2022, from <https://www.statista.com/statistics/871513/worldwide-data-created/>.
- [2] K. C. Kao and G. A. Hockham, *Dielectric-fibre surface waveguides for optical frequencies*, Proc. IEEE **113**, 1151 (1966).
- [3] F. P. Kapron, D. B. Keck, and R. D. Maurer, *Radiation losses in glass optical waveguides*, Applied Physics Letters **17**, 423 (1970).
- [4] T. Li, *Advances in optical fiber communications: An historical perspective*, IEEE Journal on Selected Areas in Communications **1**, 356 (1983).
- [5] D. J. Richardson, J. M. Fini, and L. E. Nelson, *Space-division multiplexing in optical fibres*, Nature Photonics **7**, 354 (2013).
- [6] E. Ip, A. P. T. Lau, D. J. F. Barros, and J. M. Kahn, *Coherent detection in optical fiber systems*, Opt. Express **16**, 753 (2008).
- [7] X. Liu, S. Chandrasekhar, and P. J. Winzer, *Digital signal processing techniques enabling multi-tbs superchannel transmission: An overview of recent advances in dsp-enabled superchannels*, IEEE Signal Processing Magazine **31**, 16 (2014).
- [8] V. Curri, *Multiband optical transport: a cost-effective and seamless increase of network capacity*, in *OSA Advanced Photonics Congress 2021*, page NeTu2C.3, Optica Publishing Group, 2021.
- [9] P. P. Mitra and J. B. Stark, *Nonlinear limits to the information capacity of optical fibre communications*, Nature **411**, 1027 (2001).
- [10] E. Agrell, M. Karlsson, A. R. Chraplyvy, D. J. Richardson, P. M. Krummrich, P. Winzer, K. Roberts, J. K. Fischer, S. J. Savory, B. J. Eggleton, M. Secondini, F. R. Kschischang, A. Lord, J. Prat, I. Tomkos, J. E. Bowers, S. Srinivasan, M. Brandt-Pearce, and N. Gisin, *Roadmap of optical communications*, Journal of Optics **18**, 063002 (2016).
- [11] A. Chralyvy, *The coming capacity crunch*, Plenary Address at the 35th European Conference on Optical Communication, 2009.
- [12] M.-J. Li and T. Hayashi, *Chapter 1 - advances in low-loss, large-area, and multicore fibers*, in *Optical Fiber Telecommunications VII*, edited by A. E. Willner, pages 3–50, Academic Press, 2020.

## REFERENCES

---

- [13] T. Mori, T. Sakamoto, M. Wada, T. Yamamoto, and K. Nakajima, *Few-mode fiber technology for mode division multiplexing*, *Optical Fiber Technology* **35**, 37 (2017), Next Generation Multiplexing Schemes in Fiber-based Systems.
- [14] *Europe internet users, 2022 population and Facebook statistics*, <https://www.internetworldstats.com/stats4.htm>.
- [15] *Africa internet users, 2022 population and Facebook statistics*, <https://www.internetworldstats.com/stats1.htm>.
- [16] P. K. Sahoo and A. K. Yadav, *A comprehensive road map of modern communication through free-space optics*, *Journal of Optical Communications*, 000010151520200238 (2020).
- [17] S. Arnon, J. Barry, G. Karagiannidis, R. Schober, and M. Uysal, editors, *Advanced Optical Wireless Communication Systems*, Cambridge University Press, 2012.
- [18] A. Trichili, M. A. Cox, B. S. Ooi, and M.-S. Alouini, *Roadmap to free space optics*, *J. Opt. Soc. Am. B* **37**, A184 (2020).
- [19] Z. Ghassemlooy, A. Majumdar, and A. B. Raj, *Introduction to free space optical (FSO) communications*, in *Principles and Applications of Free Space Optical Communications*, pages 1–26, Institution of Engineering and Technology, 2019.
- [20] Z. Qu and I. B. Djordjevic, *Free-space optical communication over strong atmospheric turbulence channels*, in *Principles and Applications of Free Space Optical Communications*, pages 27–38, Institution of Engineering and Technology, 2019.
- [21] O. Korotkova, L. C. Andrews, and R. L. Phillips, *Model for a partially coherent Gaussian beam in atmospheric turbulence with application in Lasercom*, *Optical Engineering* **43**, 330 (2004).
- [22] L. Mandel and E. Wolf, *Optical coherence and quantum optics*, Cambridge University, 1995.
- [23] M. Born and E. Wolf, *Principles of Optics*, Cambridge University, 7 edition, 1999.
- [24] E. Wolf, *The influence of young's interference experiment on the development of statistical optics*, *Progress in Optics* **50**, 251 (2007).
- [25] A. S. Ostrovsky, M. A. Olvera-Santamaría, and P. C. Romero-Soría, *Effect of coherence and polarization on resolution of optical imaging system*, *Optics Letters* **36**, 1677 (2011).
- [26] B. Redding, M. A. Choma, and H. Cao, *Speckle-free laser imaging using random laser illumination*, *Nature Photonics* **6**, 355 (2012).
- [27] E. Baleine and A. Dogariu, *Variable coherence tomography*, *Optics Letters* **29**, 1233 (2004).
- [28] E. Baleine and A. Dogariu, *Variable-coherence tomography for inverse scattering problems*, *Journal of the Optical Society of America A* **21**, 1917 (2004).
- [29] E. Baleine and A. Dogariu, *Variable Coherence Scattering Microscopy*, *Physical Review Letters* **95**, 193904 (2005).
- [30] G. Gbur and E. Wolf, *Spreading of partially coherent beams in random media*,

- Journal of the Optical Society of America A **19**, 1592 (2002).
- [31] A. Norrman, S. A. Ponomarenko, and A. T. Friberg, *Partially coherent surface plasmon polaritons*, EPL **116**, 64001 (2016).
- [32] Y. Chen, A. Norrman, S. A. Ponomarenko, and A. T. Friberg, *Optical coherence and electromagnetic surface waves*, Prog. Optics **65**, 105 (2020).
- [33] L.-G. Wang, C.-L. Zhao, L.-Q. Wang, X.-H. Lu, and S.-Y. Zhu, *Effect of spatial coherence on radiation forces acting on a Rayleigh dielectric sphere*, Optics Letters **32**, 1393 (2007).
- [34] J. M. Auñón and M. Nieto-Vesperinas, *Optical forces on small particles from partially coherent light*, Journal of the Optical Society of America A **29**, 1389 (2012).
- [35] J. M. Auñón and M. Nieto-Vesperinas, *Partially coherent fluctuating sources that produce the same optical force as a laser beam*, Optics Letters **38**, 2869 (2013).
- [36] S. Divitt, L. Rondin, and L. Novotny, *Cancellation of non-conservative scattering forces in optical traps by counter-propagating beams*, Optics Letters **40**, 1900 (2015).
- [37] G. Gbur, *Partially coherent beam propagation in atmospheric turbulence [Invited]*, Journal of the Optical Society of America A **31**, 2038 (2014).
- [38] R. Loudon, *The Quantum Theory Of Light*, Oxford University, 3 edition, 2000.
- [39] A. Nardi, S. Divitt, M. Rossi, F. Tebbenjohanns, A. Militaru, M. Frimmer, and L. Novotny, *Encoding information in the mutual coherence of spatially separated light beams*, Opt. Lett. **47**, 4588 (2022).
- [40] E. Wolf, *Introduction to the Theory of Coherence and Polarization of Light*, Cambridge University, 2007.
- [41] O. Korotkova and G. Gbur, *Unified matrix representation for spin and orbital angular momentum in partially coherent beams*, Phys. Rev. A **103**.
- [42] J. Goodman, *Introduction to Fourier Optics*, McGraw-Hill, 2 edition, 1988.
- [43] L. Devroye, *Non-Uniform Random Variate Generation*, Springer, 1986.
- [44] H. Wolkowicz and G. P. Styan, *Bounds for eigenvalues using traces*, Linear Algebra and its Applications **29**, 471 (1980).
- [45] J. J. Gil, *Sources of asymmetry and the concept of nonregularity of n-dimensional density matrices*, Symmetry **12**, 1002 (2020).
- [46] J. Brooks, R. Wentworth, R. Youngquist, M. Tur, B. Kim, and H. Shaw, *Coherence multiplexing of fiber-optic interferometric sensors*, Journal of Lightwave Technology **3**, 1062 (1985).
- [47] D. D. Sampson, G. J. Pendock, and R. A. Griffin, *Photonic code-division multiple-access communications*, Fiber and Integrated Optics **16**, 129 (1997).
- [48] G. Kats and S. Arnon, *Analysis of optical coherence multiplexing networks for satellite communication*, IEEE Transactions on Wireless Communications **3**, 1444 (2004).
- [49] R. Griffin, D. Sampson, and D. Jackson, *Coherence coding for photonic code-division multiple access networks*, Journal of Lightwave Technology **13**, 1826 (1995).

## REFERENCES

---

- [50] A. Meijerink, R. O. Taniman, G. H. L. M. Heideman, and W. van Etten, *Coherence multiplex system topologies*, IEEE Journal of Selected Topics in Quantum Electronics **13**, 1433 (2007).
- [51] R. H. Wentworth, *Theoretical noise performance of coherence-multiplexed interferometric sensors*, Journal of Lightwave Technology **7**, 941 (1989).
- [52] K. W. Chu and F. M. Dickey, *Optical Coherence Multiplexing For Interprocessor Communications*, in *Optical Interconnects in the Computer Environment*, edited by J. Pazaris and G. R. Willenbring, volume 1178, pages 11 – 23, International Society for Optics and Photonics, SPIE, 1990.
- [53] G. J. Pendock and D. D. Sampson, *Noise in coherence-multiplexed optical fiber systems*, Applied optics **36**, 9536 (1997).
- [54] G. Pendock and D. Sampson, *Capacity of coherence-multiplexed cdma networks*, Optics Communications **143**, 109 (1997).
- [55] W. B. Spillman and E. Udd, *Field guide to fiber optic sensors*, SPIE, 2014.
- [56] K. Blotekjaer, R. Wentworth, and H. Shaw, *Choosing relative optical path delays in series-topology interferometric sensor arrays*, Journal of lightwave technology **5**, 229 (1987).
- [57] C. Shannon, *Communication in the presence of noise*, Proceedings of the IRE **37**, 10 (1949).
- [58] T. Erseghe, *Digital modulation systems*, in *Principles of Communications Networks and Systems*, edited by N. Benvenuto and M. Zorzi, chapter 5, pages 259–371, John Wiley & Sons, Ltd, 2011.
- [59] D. Spirit, A. Ellis, and P. Barnsley, *Optical time division multiplexing: systems and networks*, IEEE Communications Magazine **32**, 56 (1994).
- [60] Z.-Y. Chen, L.-S. Yan, Y. Pan, L. Jiang, A.-L. Yi, W. Pan, and B. Luo, *Use of polarization freedom beyond polarization-division multiplexing to support high-speed and spectral-efficient data transmission*, Light: Science & Applications **6**, e16207 (2017).
- [61] J. Wang, J.-y. Yang, I. M. Fazal, N. Ahmed, Y. Yan, H. Huang, Y. Ren, Y. Yue, S. Dolinar, M. Tur, and A. E. Willner, *Terabit free-space data transmission employing orbital angular momentum multiplexing*, Nature Photonics **6**, 488 (2012).
- [62] N. Bozinovic, Y. Yue, Y. Ren, M. Tur, P. Kristensen, H. Huang, A. E. Willner, and S. Ramachandran, *Terabit-Scale Orbital Angular Momentum Mode Division Multiplexing in Fibers*, Science **340**, 1545 (2013).
- [63] J. Pfeifle et al., *Coherent terabit communications with microresonator kerr frequency combs*, Nature photonics **8**, 375 (2014).
- [64] G. Pendock and D. Sampson, *Increasing the transmission capacity of coherence multiplexed communication systems by using differential detection*, IEEE Photonics Technology Letters **7**, 1504 (1995).
- [65] A. Cagliero and R. Gaffoglio, *On the spectral efficiency limits of an oam-based multiplexing scheme*, IEEE Antennas and Wireless Propagation Letters **16**, 900 (2017).
- [66] B. J. Puttnam, G. Rademacher, and R. S. Luís, *Space-division multiplexing for*

- optical fiber communications*, *Optica* **8**, 1186 (2021).
- [67] G. J. Pendock and D. D. Sampson, *Capacity of coherence-multiplexed CDMA networks*, *Optics Communications* **143**, 109 (1997).
- [68] H. Yasaka and Y. Shibata, *Fibre Optic Communication: Key Devices*, chapter Semiconductor-Based Modulators, pages 359–416, Springer International Publishing, Cham, 2017.
- [69] R. Wu, F. Yang, Y. Sun, N. Cheng, J. Wang, F. Wei, Y. Gui, and H. Cai, *Absolute phase marking technology and fiber-optic remote coherent phase transmission*, *Opt. Express* **29**, 14041 (2021).
- [70] B. Wacogne and D. Jackson, *Enhanced security in a coherence modulation system using optical path difference corruption*, *IEEE Photonics Technology Letters* **8**, 947 (1996).
- [71] K. H. Kagalwala, H. E. Kondakci, A. F. Abouraddy, and B. E. A. Saleh, *Optical coherency matrix tomography*, *Scientific Reports* **5**, 15333 (2015).
- [72] P. De Santis, F. Gori, G. Guattari, and C. Palma, *An example of a Collett-Wolf source*, *Optics Communications* **29**, 256 (1979).
- [73] M. W. Hyde, S. Basu, D. G. Voelz, and X. Xiao, *Experimentally generating any desired partially coherent Schell-model source using phase-only control*, *Journal of Applied Physics* **118**, 093102 (2015).
- [74] B. Rodenburg, M. Mirhosseini, O. S. Magaña-Loaiza, and R. W. Boyd, *Experimental generation of an optical field with arbitrary spatial coherence properties*, *Journal of the Optical Society of America B* **31**, A51 (2014).
- [75] K. Sethuraj and B. Kanseri, *Optical coherence engineering in the polarization and spatial degrees of freedom*, *Journal of Modern Optics* **66**, 1896 (2019).
- [76] S. Divitt, M. Frimmer, T. D. Visser, and L. Novotny, *Modulation of optical spatial coherence by surface plasmon polaritons*, *Optics Letters* **41**, 3094 (2016).
- [77] D. Li and D. Pacifici, *Strong amplitude and phase modulation of optical spatial coherence with surface plasmon polaritons*, *Sci. Adv.* **3**, e1700133 (2017).
- [78] M. Reck, A. Zeilinger, H. J. Bernstein, and P. Bertani, *Experimental realization of any discrete unitary operator*, *Physical Review Letters* **73**, 58 (1994).
- [79] D. A. B. Miller, *Self-configuring universal linear optical component [Invited]*, *Photonics Research* **1**, 1 (2013).
- [80] J. Carolan, C. Harrold, C. Sparrow, E. Martin-Lopez, N. J. Russell, J. W. Silverstone, P. J. Shadbolt, N. Matsuda, M. Oguma, M. Itoh, G. D. Marshall, M. G. Thompson, J. C. F. Matthews, T. Hashimoto, J. L. O’Brien, and A. Laing, *Universal linear optics*, *Science* **349**, 711 (2015).
- [81] A. Ribeiro, A. Ruocco, L. Vanacker, and W. Bogaerts, *Demonstration of a  $4 \times 4$ -port universal linear circuit*, *Optica* **3**, 1348 (2016).
- [82] D. A. B. Miller, *Self-configuring universal linear optical component [invited]*, *Photon. Res.* **1**, 1 (2013).
- [83] N. Tischler, C. Rockstuhl, and K. Słowik, *Quantum Optical Realization of Arbitrary Linear Transformations Allowing for Loss and Gain*, *Physical Review X* **8**, 021017 (2018).

## REFERENCES

---

- [84] J. W. Goodman, *Speckle phenomena in optics : theory and applications*, Roberts and Company, 2007.
- [85] S. M. Popoff, G. Lerosey, R. Carminati, M. Fink, A. C. Boccarda, and S. Gigan, *Measuring the Transmission Matrix in Optics: An Approach to the Study and Control of Light Propagation in Disordered Media*, *Physical Review Letters* **104**, 100601 (2010).
- [86] I. M. Vellekoop, A. Lagendijk, and A. P. Mosk, *Exploiting disorder for perfect focusing*, *Nature Photonics* **4**, 320 (2010).
- [87] E. G. Van Putten, D. Akbulut, J. Bertolotti, W. L. Vos, A. Lagendijk, and A. P. Mosk, *Scattering lens resolves sub-100 nm structures with visible light*, *Physical Review Letters* **106**, 193905 (2011).
- [88] A. Boniface, M. Mounaix, B. Blochet, R. Piestun, and S. Gigan, *Transmission-matrix-based point-spread-function engineering through a complex medium*, *Optica* **4**, 54 (2017).
- [89] W. Xiong, C. W. Hsu, Y. Bromberg, J. E. Antonio-Lopez, R. Amezcua Correa, and H. Cao, *Complete polarization control in multimode fibers with polarization and mode coupling*, *Light: Science and Applications* **7**, 54 (2018).
- [90] Y. Guan, O. Katz, E. Small, J. Zhou, and Y. Silberberg, *Polarization control of multiply scattered light through random media by wavefront shaping*, *Optics Letters* **37**, 4663 (2012).
- [91] D. Andreoli, G. Volpe, S. Popoff, O. Katz, S. Grésillon, and S. Gigan, *Deterministic control of broadband light through a multiply scattering medium via the multispectral transmission matrix*, *Sci. Rep.* **5**, 10347 (2015).
- [92] M. Mounaix, D. Andreoli, H. Defienne, G. Volpe, O. Katz, S. Grésillon, and S. Gigan, *Spatiotemporal Coherent Control of Light through a Multiple Scattering Medium with the Multispectral Transmission Matrix*, *Physical Review Letters* **116**, 253901 (2016).
- [93] M. Mounaix, D. M. Ta, and S. Gigan, *Transmission matrix approaches for nonlinear fluorescence excitation through multiple scattering media*, *Optics Letters* **43**, 2831 (2018).
- [94] A. Boniface, M. Mounaix, B. Blochet, H. B. de Aguiar, F. Quéré, and S. Gigan, *Spectrally resolved point-spread-function engineering using a complex medium*, *Optics Express* **29**, 8985 (2021).
- [95] M. W. Matthès, P. del Hougne, J. de Rosny, G. Lerosey, and S. M. Popoff, *Optical complex media as universal reconfigurable linear operators*, *Optica* **6**, 465 (2019).
- [96] T. A. W. Wolterink, R. Uppu, G. Ctistis, W. L. Vos, K.-J. Boller, and P. W. H. Pinkse, *Programmable two-photon quantum interference in  $10^3$  channels in opaque scattering media*, *Physical Review A* **93**, 053817 (2016).
- [97] S. Leedumrongwattanakun, L. Innocenti, H. Defienne, T. Juffmann, A. Ferraro, M. Paternostro, and S. Gigan, *Programmable linear quantum networks with a multimode fibre*, *Nature Photonics* **14**, 139 (2020).
- [98] J.-H. Park, C. Park, H. Yu, Y.-H. Cho, and Y. Park, *Dynamic active wave plate using random nanoparticles*, *Optics Express* **20**, 17010 (2012).

- 
- [99] Y. Guan, O. Katz, E. Small, J. Zhou, and Y. Silberberg, *Polarization control of multiply scattered light through random media by wavefront shaping*, Optics letters **37**, 4663 (2012).
- [100] E. Small, O. Katz, Y. Guan, and Y. Silberberg, *Spectral control of broadband light through random media by wavefront shaping*, Optics letters **37**, 3429 (2012).
- [101] J.-H. Park, C. Park, H. Yu, Y.-H. Cho, and Y. Park, *Active spectral filtering through turbid media*, Optics letters **37**, 3261 (2012).
- [102] B. Redding, S. M. Popoff, and H. Cao, *All-fiber spectrometer based on speckle pattern reconstruction*, Optics express **21**, 6584 (2013).
- [103] B. Redding, M. Alam, M. Seifert, and H. Cao, *High-resolution and broadband all-fiber spectrometers*, Optica **1**, 175 (2014).
- [104] G. Jacucci, L. Delloye, D. Pierangeli, M. Rafayelyan, C. Conti, and S. Gigan, *Tunable spin-glass optical simulator based on multiple light scattering*, Phys. Rev. A **105**, 033502 (2022).
- [105] R. Savo, A. Morandi, J. S. Müller, F. Kaufmann, F. Timpu, M. R. Escalé, M. Zanini, L. Isa, and R. Grange, *Broadband mie driven random quasi-phase-matching*, Nature Photonics **14**, 740 (2020).
- [106] S. Rotter and S. Gigan, *Light fields in complex media: Mesoscopic scattering meets wave control*, Reviews of Modern Physics **89**, 015005 (2017).
- [107] H. Yu, T. R. Hillman, W. Choi, J. O. Lee, M. S. Feld, R. R. Dasari, and Y. Park, *Measuring large optical transmission matrices of disordered media*, Phys. Rev. Lett. **111**, 153902 (2013).
- [108] A. Goetschy and A. D. Stone, *Filtering random matrices: The effect of incomplete channel control in multiple scattering*, Phys. Rev. Lett. **111**, 063901 (2013).
- [109] S. M. Popoff, G. Lerosey, M. Fink, A. C. Boccara, and S. Gigan, *Controlling light through optical disordered media: Transmission matrix approach*, New Journal of Physics **13**, 123021 (2011).
- [110] A. Hedayat and W. D. Wallis, *Hadamard matrices and their applications*, The Annals of Statistics, 1184 (1978).
- [111] L. Devaud, B. Rauer, J. Melchard, M. Kühmayer, S. Rotter, and S. Gigan, *Speckle engineering through singular value decomposition of the transmission matrix*, Phys. Rev. Lett. **127**, 093903 (2021).
- [112] A. Dubois, L. Vabre, A. C. Boccara, and E. Beurepaire, *High-resolution full-field optical coherence tomography with a Linnik microscope*, Applied Optics **41**, 805 (2002).
- [113] J. A. Davis, D. M. Cottrell, J. Campos, M. J. Yzuel, and I. Moreno, *Encoding amplitude information onto phase-only filters*, Applied Optics **38**, 5004 (1999).
- [114] T. Young, *A Course of Lectures on Natural Philosophy and the Mechanical Arts, vols. I and II*, J. Johnson, 1807.
- [115] E. Wolf, *Unified theory of coherence and polarization of random electromagnetic beams*, Physics Letters A **312**, 263 (2003).
- [116] K. H. Kagalwala, G. D. Giuseppe, A. F. Abouraddy, and B. E. A. Saleh, *Bell's*



## REFERENCES

---

- measure in classical optical coherence*, Nature Photonics **7**, 72 (2012).
- [117] Y. Lian, D. Lan, S. Xing, B. Guo, Z. Ren, R. Lai, C. Zou, B. Zhao, R. H. Friend, and D. Di, *Ultralow-voltage operation of light-emitting diodes*, Nature Communications **13** (2022).
- [118] S. Turtaev, I. T. Leite, K. J. Mitchell, M. J. Padgett, D. B. Phillips, and T. Čížmár, *Comparison of nematic liquid-crystal and DMD based spatial light modulation in complex photonics*, Optics Express **25**, 29874 (2017).
- [119] C. Peng, R. Hamerly, M. Soltani, and D. R. Englund, *Design of high-speed phase-only spatial light modulators with two-dimensional tunable microcavity arrays*, Opt. Express **27**, 30669 (2019).
- [120] X. Sun, G. Liu, H. Yu, D. Ban, N. Deng, and F. Qiu, *Design and theoretical characterization of high speed metasurface modulators based on electro-optic polymer*, Opt. Express **29**, 9207 (2021).
- [121] Y.-Y. Xie, B.-Y. Wang, Z.-J. Cheng, Q.-Y. Yue, and C.-S. Guo, *Measurement of vector transmission matrix and control of beam focusing through a multiple-scattering medium based on a vector spatial light modulator and two-channel polarization holography*, Applied Physics Letters **110**, 221105 (2017).
- [122] A. Boniface, M. Mounaix, B. Blochet, R. Piestun, and S. Gigan, *Transmission-matrix-based point-spread-function engineering through a complex medium*, Optica **4**, 54 (2017).
- [123] M. Mounaix, N. K. Fontaine, D. T. Neilson, R. Ryf, H. Chen, J. C. Alvarado-Zacarias, and J. Carpenter, *Time reversed optical waves by arbitrary vector spatiotemporal field generation*, Nature communications **11**, 1 (2020).
- [124] S. Tripathi, R. Paxman, T. Bifano, and K. C. Toussaint, *Vector transmission matrix for the polarization behavior of light propagation in highly scattering media*, Opt. Express **20**, 16067 (2012).
- [125] H. Kupianskyi, S. A. Horsley, and D. B. Phillips, *High-dimensional spatial mode sorting and optical circuit design using multi-plane light conversion*, arXiv preprint arXiv:2209.11081 (2022).
- [126] R. Fickler, M. Ginoya, and R. W. Boyd, *Custom-tailored spatial mode sorting by controlled random scattering*, Phys. Rev. B **95**, 161108 (2017).
- [127] H. Defienne and D. Faccio, *Arbitrary spatial mode sorting in a multimode fiber*, Phys. Rev. A **101**, 063830 (2020).
- [128] M. Liu, Y. Lei, L. Yu, X. Fang, Y. Ma, L. Liu, J. Zheng, and P. Gao, *Super-resolution optical microscopy using cylindrical vector beams*, Nanophotonics **11**, 3395 (2022).
- [129] R. W. Gerchberg, *A practical algorithm for the determination of plane from image and diffraction pictures*, Optik **35**, 237 (1972).
- [130] L. Novotny and B. Hecht, *Principles of nano-optics*, Cambridge university press, 2012.
- [131] C.-C. Sun and C.-K. Liu, *Ultrasmall focusing spot with a long depth of focus based on polarization and phase modulation*, Optics letters **28**, 99 (2003).
- [132] W. Chen and Q. Zhan, *Three-dimensional focus shaping with cylindrical vector beams*, Optics Communications **265**, 411 (2006).

- [133] C. Maurer, A. Jesacher, S. Fürhapter, S. Bernet, and M. Ritsch-Marte, *Tailoring of arbitrary optical vector beams*, New Journal of Physics **9**, 78 (2007).
- [134] K. J. Mitchell, S. Turtaev, M. J. Padgett, T. Čižmár, and D. B. Phillips, *High-speed spatial control of the intensity, phase and polarisation of vector beams using a digital micro-mirror device*, Opt. Express **24**, 29269 (2016).
- [135] T. Weiss and O. Romero-Isart, *Quantum motional state tomography with nonquadratic potentials and neural networks*, Phys. Rev. Research **1**, 033157 (2019).
- [136] A. L. Gaunt, T. F. Schmidutz, I. Gotlibovych, R. P. Smith, and Z. Hadzibabic, *Bose-einstein condensation of atoms in a uniform potential*, Phys. Rev. Lett. **110**, 200406 (2013).
- [137] R. Gutiérrez-Cuevas and M. A. Alonso, *Three-dimensional quartic intensity distribution*, Internal note, unpublished, 2018.
- [138] V. Arrizón, U. Ruiz, R. Carrada, and L. A. González, *Pixelated phase computer holograms for the accurate encoding of scalar complex fields*, JOSA A **24**, 3500 (2007).
- [139] T. W. Clark, R. F. Offer, S. Franke-Arnold, A. S. Arnold, and N. Radwell, *Comparison of beam generation techniques using a phase only spatial light modulator*, Opt. Express **24**, 6249 (2016).
- [140] C. Rosales-Guzmán and A. Forbes, *How to shape light with spatial light modulators*, SPIE Press, 2017.
- [141] J. A. Davis, D. E. McNamara, D. M. Cottrell, and T. Sonehara, *Two-dimensional polarization encoding with a phase-only liquid-crystal spatial light modulator*, Appl. Opt. **39**, 1549 (2000).
- [142] M. R. Beversluis, L. Novotny, and S. J. Stranick, *Programmable vector point-spread function engineering*, Opt. Express **14**, 2650 (2006).
- [143] N. C. Pisoni, *Simplified approach to the jones calculus in retracing optical circuits*, Appl. Opt. **34**, 7870 (1995).
- [144] A. Jesacher, A. Schwaighofer, S. Fürhapter, C. Maurer, S. Bernet, and M. Ritsch-Marte, *Wavefront correction of spatial light modulators using an optical vortex image*, Optics express **15**, 5801 (2007).
- [145] D. Engström, M. Persson, J. Bengtsson, and M. Goksör, *Calibration of spatial light modulators suffering from spatially varying phase response*, Optics express **21**, 16086 (2013).
- [146] S. Reichelt, *Spatially resolved phase-response calibration of liquid-crystal-based spatial light modulators*, Applied optics **52**, 2610 (2013).
- [147] H. W. Babcock, *The possibility of compensating astronomical seeing*, Publications of the Astronomical Society of the Pacific **65**, 229 (1953).
- [148] R. W. Cole, T. Jinadasa, and C. M. Brown, *Measuring and interpreting point spread functions to determine confocal microscope resolution and ensure quality control*, Nature protocols **6**, 1929 (2011).
- [149] P. C. Goodwin, *Evaluating optical aberration using fluorescent microspheres: methods, analysis, and corrective actions*, Methods in cell biology **81**, 397 (2007).

## REFERENCES

---

- [150] R. Loudon, *The quantum theory of light*, Oxford science publications, Oxford Univ. Press, Oxford, 3rd ed., [repr.] edition, 2006.
- [151] L.-P. Leppänen, K. Saastamoinen, A. T. Friberg, and T. Setälä, *Measurement of the degree of temporal coherence of unpolarized light beams*, *Photon. Res.* **5**, 156 (2017).

---

## List of Publication

**This thesis is based in part on the following publications:**

**A. Nardi**, F. Tebbenjohanns, M. Rossi, S. Divitt, A. Norrman, S. Gigan, M. Frimmer, and L. Novotny, *Controlling spatial coherence with an optical complex medium*, *Opt. Express* **29**, 40831-40840 (2021).

**A. Nardi**, S. Divitt, M. Rossi, F. Tebbenjohanns, A. Militaru, M. Frimmer, and L. Novotny, *Encoding information in the mutual coherence of spatially separated light beams*, *Opt. Lett.* **47**, 4588-4591 (2022).

**A. Nardi**, F. Tebbenjohanns, M. Rossi, S. Divitt, A. Norrman, S. Gigan, M. Frimmer, and L. Novotny, “Controlling spatial coherence with a complex medium”, in *CLEO: QELS Fundamental Science* (pp. JF3A–3), Optica Publishing Group (2022).

**A. Nardi**, F. Tebbenjohanns, M. Frimmer, and L. Novotny, “Programmable Generation of Arbitrary Light Field Distributions”, in *Light-Matter Interactions Towards the Nanoscale* (pp. 345-348). Springer, Dordrecht (2022).



---

## Curriculum vitae

**Alfonso Nardi**, born on December 4th, 1993, in Penne, Italy.

### Professional Experience

2019–2023	Doctoral Researcher ETH Zurich, Photonics Laboratory
2018–2019	Master thesis ETH Zurich, Photonics Laboratory

### Education

2015–2018	Master Degree in Electronics Engineering Politecnico di Milano, Italy
2012–2015	Bachelor Degree in Electronics Engineering Politecnico di Milano, Italy

